Variable-Stiffness and Shape-Morphing Structured Media

Thesis by
Tracy Lu

In Partial Fulfillment of the Requirements for the
Degree of
Doctor of Philosophy in Mechanical Engineering

CALIFORNIA INSTITUTE OF TECHNOLOGY
Pasadena, California

2025
Defended March 11, 2025

Tracy Lu
ORCID: 0009-0004-4919-814X

ACKNOWLEDGEMENTS

First, I would like to thank my advisor. Working with her over the past 5 years, I have learned so much from the way she boldly pursues new ideas and communicates her thoughts and visions. I couldn't be more grateful to her for offering the opportunity to pursue projects and internships, for introducing me to an amazing community at Caltech and other institutions, and for her encouragement and passion.

I would like to thank my Caltech, JPL, and Meta collaborators for teaching me about their respective expertise and about how to be a better engineer, researcher, and communicator.

I would also like to thank my family. To my parents, I am thankful for their persistent support of my education from an early age and for instilling in me the value of learning and perseverance. I am also grateful to my younger sister, who has been by my side throughout my entire grade school journey, attending school with me for as long as I can remember before I went to college, and always getting better grades than me which, along with natural sibling rivalry, motivated me to work harder.

I am incredibly grateful to my MCE cohort. When I first arrived at Caltech, I feared that the competitive environment might feel isolating. However, I quickly discovered that they were not only brilliant but also friendly, supportive, and always eager to help. I have learned so much from all of them, and I know I wouldn't have made it through the demanding classes, qualifying exams, and candidacy exam without their support. I would especially like to give a heartfelt thanks to the women in our cohort. I loved being part of a group with an unusually high representation of women compared to the other cohorts.

Before coming to Caltech, I'm embarrassed to admit that I wasn't sure if Sri Lanka was a country and I didn't know where Romania, Azores, or Lebanon were on the map. However, after these past five and a half years, not only do I now know their geographical locations, but also I've eaten lots of delicious food and know about unique cultural quirks from each place. What I love most about Caltech is how it brings together brilliant minds from across the country and different pockets of the world, all within this tiny campus spanning just two blocks. Without Caltech, I would never have had the chance to meet these amazing people. I have learned so much from my friends here, and I am deeply grateful for their unwavering support

through the hardships of my PhD, as well as for the countless moments of joy, laughter, and camaraderie that made the journey worth it. As we all move on to new opportunities beyond Pasadena, I truly hope our relationships continue for years to come.

ABSTRACT

Advancements in additive manufacturing and material synthesis with highly controlled geometries have enabled the creation of structured media, engineered materials with patterned micro- and meso-scale geometries that impart unique mechanical properties. By fine-tuning these architectures, structured materials can achieve properties beyond those of their base materials. A subcategory, structured fabrics, consists of discrete granular particles rather than continuous fibers. Their mechanical behavior is governed by jamming, a transition driven by geometric constraints, allowing them to switch between flexible and rigid states. By leveraging the interactions of the building blocks, structured fabrics enable tunable stiffness, global shape change, and adaptive functionalities, making them ideal for wearable, deployable, and morphing structures.

The first structured fabric study explores a topologically interlocking material (TIM) system with adjustable bending stiffness controlled by external pre-stress. The system consists of truncated tetrahedral particles connected by tensioned nylon wires, allowing stiffness to be tuned by varying wire tension. Experiments examine the effects of surface friction and interlocking angle on bending response, guided by Level Set Discrete Element Method (LS-DEM) simulations. The second design presents deployable 3D structures that fold without rigid mechanisms, offering compact storage and stable deployment. The design consists of computationally generated rigid tiles adhered to a pre-stretched elastic sheet, which transforms from a flat state and jams into a predetermined 3D shape when released. Although the designs exhibited unique mechanical properties, experimentally understanding their internal mechanics was challenging due to limited visibility of the concealed membrane upon jamming. To optimize future designs, simulations were conducted to analyze the effects of various pattern designs and folding on membrane behavior.

PUBLISHED CONTENT AND CONTRIBUTIONS

T. Lu, Z. Zhou, P. Bordeenithikasem, N. Chung, D.F. Franco, J.E. Andrade, and C. Daraio. (2024). "Role of friction and geometry in tuning the bending stiffness of topologically interlocking materials". In: *Extreme Mechanics Letters,* vol.71, p.102 212. DOI: 10.1016/j.eml.2024.102212.
T.L. participated in the conception, design, methodology, experimental fabrication, visualization, validation, supervision of undergraduate researchers, software usage, experimental data acquisition, and data analysis.

T. Lu, P. Bordeenithikasem, C. McMahan, R. T. Watkins, and C. Daraio (in review). "A structured fabric design for folding and deploying 3D surfaces". *American Society of Mechanical Engineers Journal of Mechanisms and Robotics,*
(2025 in review), T.L. participated in the funding acquisition, conception, design, methodology, coding, experimental fabrication, visualization, validation, software usage, and data analysis.

T. Lu, A. Ogren, and C. Daraio. "Analysis of elastic membranes with rigid components". *(not submitted)*
(2025), T.L. participated in the conception, design, methodology, coding, simulation experiments, visualization, software usage, and data analysis.

TABLE OF CONTENTS

LIST OF ILLUSTRATIONS

LIST OF TABLES

Chapter 1

INTRODUCTION

1.1 Thesis Objectives and Outline

This thesis aims to advance the understanding and design of structured fabrics, a subcategory of structured media characterized by discrete components that can transition between flexible and rigid states. By investigating their tunable mechanical properties and deployable capabilities, this work aims to unlock new possibilities for adaptive, shape-morphing structured fabrics. More specifically, the chapters are outlined as follows: The first chapter explores the motivation behind designing new metamaterials using modern additive manufacturing and material synthesis technologies, which have led to the development of structured media and structured fabrics. Given our interest in multifunctional materials that integrate tunable stiffness and shape transformation, we also examine the challenges associated with morphing flat surfaces into three-dimensional structures and how these principles can be applied to structured fabrics. Additionally, we highlight key applications of these designs, demonstrating their potential across various fields.

The second chapter investigates the tunable stiffness in a topologically interlocking material (TIM) inspired structured fabric design. This involves examining the role of particle geometry, inter-particle friction, and applied tension in governing the bending response of TIM-based structured fabrics. By conducting both experimental and numerical analyses, the study aims to determine how contact angle and surface friction influence the stiffness and overall mechanical behavior of these materials. Additionally, the research explores the function of woven tension wires in enabling tunable stiffness, allowing the system to alternate between flexible and rigid states. Understanding these interactions provide insights into how structured fabrics can achieve programmable mechanical properties, making them suitable for a wide range of applications. Finally, investigating how these designs could transition between different initial and final configurations to achieve a target shape upon stiffening served as a key inspiration for the next phase of this thesis.

The third chapter focuses on developing deployable 3D structures that transition from compact, stowable states to stable, load-bearing forms without relying on traditional hinges or rigid mechanisms. A framework is established to design and fabricate these

structures, leveraging pre-stretched elastic membranes as actuation mechanisms for controlled shape transformation. This computational design methodology uniquely combines the compressive contact characteristics of the structured fabric, boundary-first conformal mapping, and folding of thick materials to enable deployment and compaction of 3D surfaces. This approach enables the application of origami patterns to stable 3D forms, which are traditionally designed for 2D surfaces.

In the fourth chapter, finite element simulations of a hyperelastic sheet with rigid components is utilized to gain deeper insights into the strain and stress distribution within the structured fabric's membrane, based on the previous experimental and computational design work. Since direct observation of internal mechanics is challenging, simulations provide a means to analyze the effects of the boundary constraints, tile density, spacing, and folding geometries on structural integrity. By understanding these parameters, the study seeks to minimize stress concentrations, enhance long-term durability, and improve the overall mechanical response of elastic sheet based deployable structures and other systems involving a combination of rigid and hyperelastic components.

Finally, the fifth chapter summarizes the key contributions of this thesis, while the appendix provides comprehensive details on the various background theory, experiments, and simulations discussed in the preceding chapters.

1.2 Motivation

Throughout history, the discovery of new material properties has profoundly transformed human civilization, shaping technological progress and enhancing living standards. These breakthroughs have propelled advancements across diverse fields, including infrastructure, transportation, and aerospace. Traditionally, the focus of material and structural design was on understanding the inherent mechanical properties of materials, such as ductility and strength, rather than engineering those properties for specific applications. Traditional manufacturing that makes structures and machines we are familiar with, uses subtractive processes where those materials are systematically removed from a larger block or mass to create the desired final product or a mold of the final product. However, modern developments in fabrication and computational design have shifted this paradigm, allowing for the intentional design of materials with tailored mechanical behaviors.

Engineering innovation is now moving beyond conventional structural and machine design approaches, which rely on rigid mechanisms and discrete joints. This shift

is driven by the growing demand for adaptable, lightweight, and multifunctional materials. Applications such as wearable devices [1], deployable structures [2], [3], and integrated soft robotics [4]–[8] require materials with tunable mechanical properties that can transition efficiently between different configurations while reducing part counts in complex assemblies. In such systems, traditional rigid components are increasingly being replaced by compliant elements [9] that can shape change and dynamically adapt to stimuli, enabling new functionalities. Some examples are shown in Fig. 1.1 . A common challenge in shape morphing design arises from the challenge of morphing flat designs into three-dimensional structures has been explored for centuries by artists, and more recently by mathematicians and engineers [9]–[11]. In fabrication, flat materials are favored for their ease of manufacturing, as well as for their efficiency in stacking and transport [12]. However, many applications, such as tunable mirrors and parabolic antennas [13]–[15], require surfaces with dynamically changing curvatures. Morphing between flat and curved geometries thus demands control over localized deformations.

Achieving non-zero Gaussian curvature from initially flat structures requires coupling bending with in-plane stretching, as dictated by Theorema Egregium [16]. Several strategies have been developed to accomplish this transformation. For instance, auxetic and kirigami structures utilize voids and patterned cuts to facilitate controlled out-of-plane deformations [17]–[19]. More recently, kinematic frustration has emerged as a powerful tool for inducing curvature changes in flat shells [20], [21]. While these approaches are effective for lightweight structures, they often require external mechanical stimuli, such as manual manipulation, boundary loading, or the release of pre-stretched materials, to achieve their final three-dimensional shape.

It has long been understood that a material's microstructure influences its overall properties, a principle that has been extensively applied in composite materials, sandwich structures, and cellular materials [22]–[24]. However, recent advancements in manufacturing and synthesis technologies have granted engineers unprecedented control over micro- and mesoscale architectures, allowing for the creation of materials with highly specific mechanical behaviors [25]–[27]. By carefully designing these internal geometries, materials can achieve new properties, such as high stiffness-to-weight ratios [28] and bistable auxeticity [29]. This capability has dramatically expanded the design space for deployable structures and shape-shifting materials. Mesoscale design, in particular, has been leveraged to introduce com-

pliant features that replace conventional hinges and flexures, enabling structures whose mechanical behaviors can be precisely tuned by adjusting geometric patterns [30]–[32].

This has enabled the development of what we term structured media, materials in which kinematic behavior is derived from geometric patterns embedded at micro- or mesostructural length scales [33]. These structured materials feature intricate architectures that are far smaller than both the overall dimensions of the object and the scale of global deformations. This distinct separation of length scales allows structured media to exhibit extraordinary mechanical properties that go beyond those of their original bulk constitutive properties [28]. By precisely designing mesoscale geometries, these materials can be optimized to achieve specific stiffness characteristics or energetically favor targeted modes of deformation. As a result, structured media offer efficient, lightweight, and dexterous solutions to engineering challenges, unlocking new capabilities that were previously unattainable with conventional materials.

Going beyond simply replacing rigid joints with compliant counterparts, advancements in materials synthesis and additive manufacturing have enabled the creation of structures whose kinematic behaviors are derived from geometric patterns embedded at micro- or mesostructural length scales. These structures, often referred to as structured media, feature intricate geometric designs that are much smaller than both the overall dimensions of the object and the size of global deformation features. This separation of length scales allows structured media to exhibit unique mechanical behaviors, making them efficient, lightweight, and dexterous, solving problems outside the scope of traditional materials.

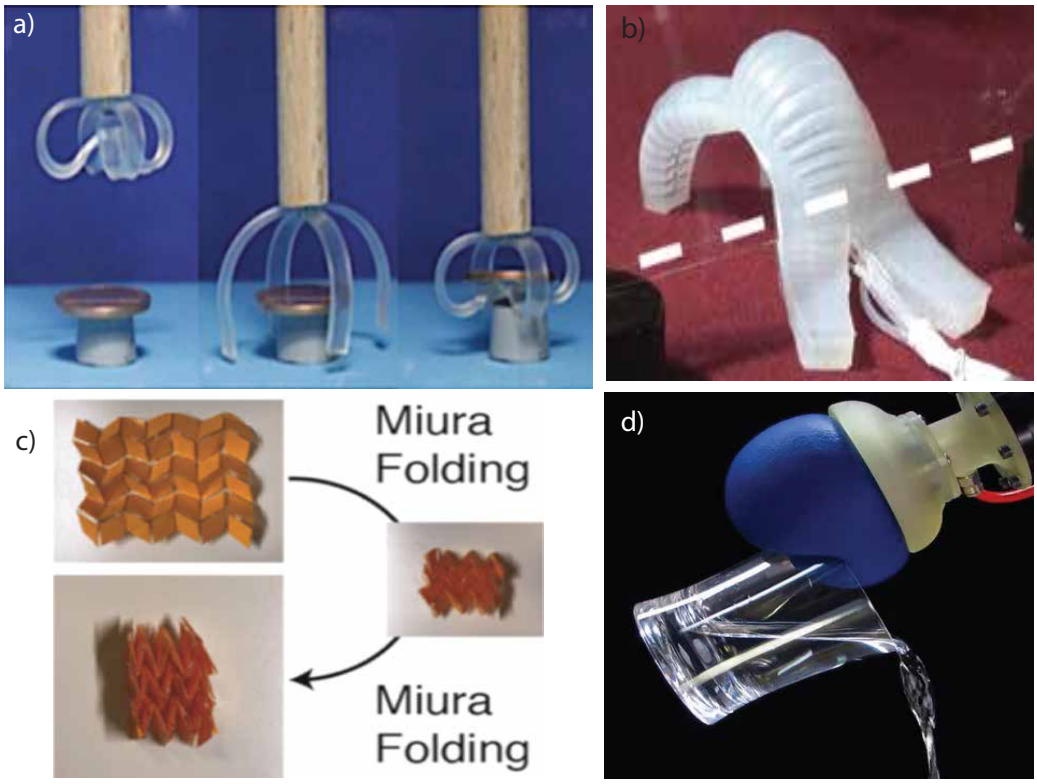

Figure 1.1: Examples of the design, synthesis, and integration of adaptive materials that can change stiffness and/or shape [34]: (a) a shape memory polymer based robotic gripper [35]. (b) soft robotic crawler [36]. (c) a thermally responsive Miura origami deployment [37]. (d) Individual fingers of a traditional robotic hand are replaced by a single mass of granular material that, when pressed onto a target object, flows around it and conforms to its shape. Upon application of a vacuum the granular material contracts and hardens quickly to pinch and hold the object without requiring sensory feedback [38].

1.3 Structured Fabrics

A subcategory of structured media is structured fabrics, which also derive their properties from a combination of the constitutive materials and their geometry [39], [40]. Unlike traditional fabrics that are woven or knitted from continuous materials such as fibers or wires, structured fabrics are composed of discrete, granular particles as their fundamental building blocks. These granular assemblies exhibit tunable mechanical properties through a phenomenon known as jamming, a phase transition driven by local geometric constraints. The jamming transition allows these systems to reversibly switch between fluid-like plasticity and solid-like rigidity, accompanied by changes in packing density.

Jamming has been widely utilized to develop adaptive materials with tunable stiffness, including soft robotic grippers [38], impact-absorbing materials [41], and reconfigurable structures [42]. However, conventional granular materials often require dense, bulky volumes to achieve sufficient mechanical stiffness when jammed [43], and assemblies of convex particles lack the ability to sustain tensile forces, limiting their bending stiffness and tensile strength [44]. These drawbacks make traditional granular systems unsuitable for applications such as wearable fabrics.

Structured fabrics, on the other hand, can leverage design principles from topologically interlocking systems to achieve desirable properties, such as global shape change and tunable stiffness, while maintaining a flexible, fabric-like state. By computationally designing the geometry of their granular components, structured fabrics can overcome the limitations of conventional granular materials, enabling novel functionalities for wearable, adaptive, or deployable applications.

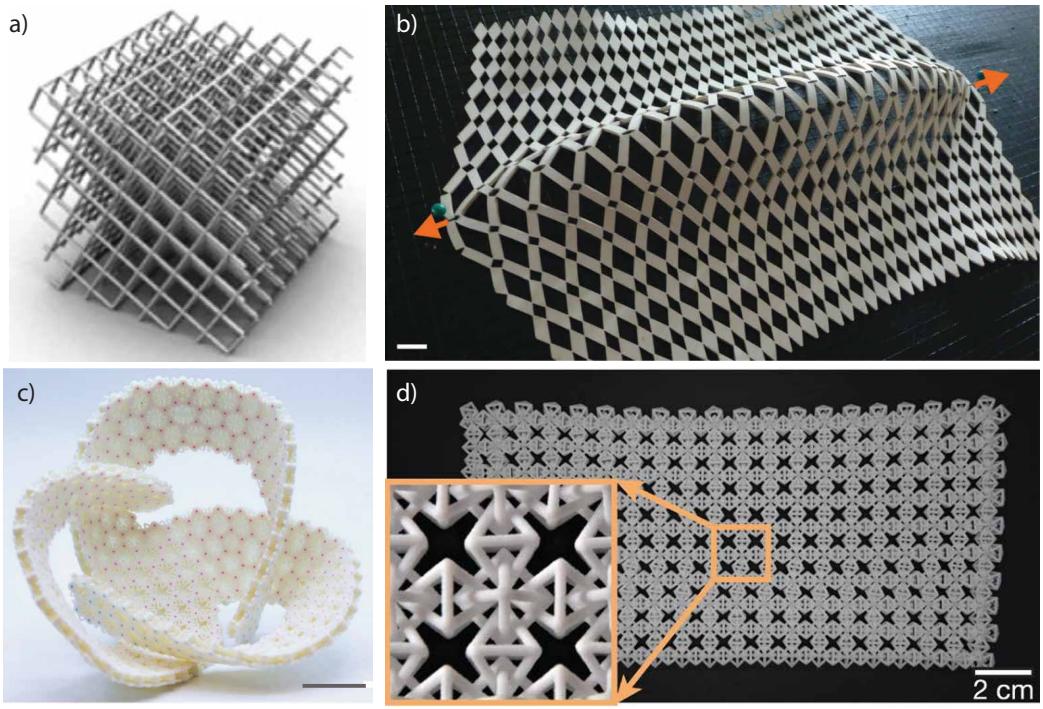

Figure 1.2: Examples of structured media: (a) Periodic and stochastic 3D lattice with energy absorption properties [45]. (b) Architected sheets with non-periodic cut patterns capable of shape-morphing; scale bar, 12 mm [33]. (c) Elastic 3D printed shells with membranes capable of temporally shape-changing; scale bar 3cm [46]. (d) 3D printed chainmail with geometrically interlocking particles [47].

Applications of Structured Fabrics

Structured fabrics have the potential to be wearable materials and could be embedded with sensors that sense and respond to environmental stimuli [48], offering applications in medical monitoring [49], wearable computing [50], energy harvesting [51], and more [52]. Fabrics with tunable mechanical properties provide new opportunities, such as mechanical feedback, joint assistance, support, and haptic perception [53]. Architected fabrics, such as chain mail layers with designed particles [47], can reversibly switch between soft and rigid states, making them promising for applications in soft robotics, shape-morphing structures, and wearable medical devices like exoskeletons and reconfigurable supports. On larger scales, tunable fabrics can be used for transportable and reconfigurable architectures, transitioning from flexible to rigid states for deployment. Their design can target desirable characteristics, such as high impact resistance, thermal regulation, or electrical conductivity, however the ones in this thesis focus on stiffness change and global shape-change.

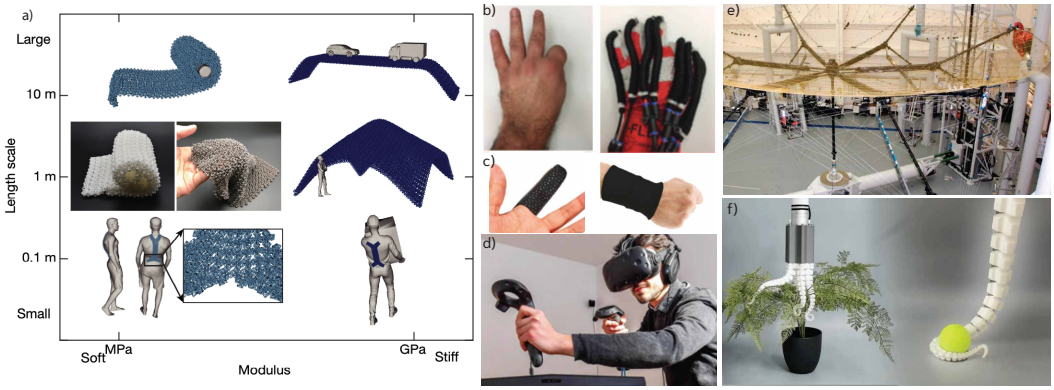

Figure 1.3: Potential structured fabric applications: (a) Possible applications of the reconfigurable fabrics at different length scales, ranging from wearable medical supports and exoskeletons (bottom) to transportable, reconfigurable architectures (top). The two inset images show the fabrics in the soft state, printed with two different materials: nylon plastic (left) and aluminum (right) [47]. Wearable structured fabrics for haptic feedback on the (b) hand and (c) finger or wrist. (d) Sensors and feedback embedded in structured fabrics could be used in virtual reality systems or other systems for communication, therapy, or entertainment. (e) A reconfigurable architecture example is a deployable antennae. (f) A structured fabric-like robotic grasper [54].

1.4 Bibliography

References

[1] Y. Yuan, S. Ma, X. Sun, *et al.*, "3d printed auxetic metamaterials with tunable mechanical properties and morphological fitting abilities," *Materials & Design*, vol. 244, p. 113 119, Aug. 1, 2024, ISSN: 0264-1275. DOI: 10.1016/j.matdes.2024.113119. [Online]. Available: https://www.sciencedirect.com/science/article/pii/S0264127524004933.

[2] J. W. Boley, W. M. van Rees, C. Lissandrello, *et al.*, "Shape-shifting structured lattices via multimaterial 4d printing," *Proceedings of the National Academy of Sciences*, vol. 116, no. 42, pp. 20 856–20 862, Oct. 15, 2019, Publisher: Proceedings of the National Academy of Sciences. DOI: 10.1073/pnas.1908806116. [Online]. Available: https://www.pnas.org/doi/full/10.1073/pnas.1908806116.

[3] M. Schenk, A. D. Viquerat, K. A. Seffen, and S. D. Guest, "Review of inflatable booms for deployable space structures: Packing and rigidization," *Journal of Spacecraft and Rockets*, vol. 51, no. 3, pp. 762–778, May 2014, Publisher: American Institute of Aeronautics and Astronautics, ISSN: 0022-4650. DOI: 10.2514/1.A32598. [Online]. Available: https://arc.aiaa.org/doi/10.2514/1.A32598.

[4] Y. Yao, J. T. Waters, A. V. Shneidman, *et al.*, "Multiresponsive polymeric microstructures with encoded predetermined and self-regulated deformability," *Proceedings of the National Academy of Sciences*, vol. 115, no. 51, pp. 12 950–12 955, Dec. 18, 2018, Publisher: Proceedings of the National Academy of Sciences. DOI: 10.1073/pnas.1811823115. [Online]. Available: https://www.pnas.org/doi/10.1073/pnas.1811823115.

[5] T. Guin, B. A. Kowalski, R. Rao, *et al.*, "Electrical control of shape in voxelated liquid crystalline polymer nanocomposites," *ACS Applied Materials & Interfaces*, vol. 10, no. 1, pp. 1187–1194, Jan. 10, 2018, Publisher: American Chemical Society, ISSN: 1944-8244. DOI: 10.1021/acsami.7b13814. [Online]. Available: https://doi.org/10.1021/acsami.7b13814.

[6] Y. Klein, E. Efrati, and E. Sharon, "Shaping of Elastic Sheets by Prescription of Non-Euclidean Metrics," *Science*, vol. 315, no. 5815, pp. 1116–1120, Feb. 2007, Publisher: American Association for the Advancement of Science. DOI: 10.1126/science.1135994. [Online]. Available: https://www.science.org/doi/10.1126/science.1135994.

[7] J. Kim, J. A. Hanna, M. Byun, C. D. Santangelo, and R. C. Hayward, "Designing responsive buckled surfaces by halftone gel lithography," *Science*, vol. 335, no. 6073, pp. 1201–1205, Mar. 9, 2012, Publisher: American Association for the Advancement of Science. DOI: 10.1126/science.1215309. [Online]. Available: https://www.science.org/doi/10.1126/science.1215309.

[8] P. Plucinsky, B. A. Kowalski, T. J. White, and K. Bhattacharya, "Patterning nonisometric origami in nematic elastomer sheets," *Soft Matter*, vol. 14, no. 16, pp. 3127–3134, Apr. 25, 2018, Publisher: The Royal Society of Chemistry, ISSN: 1744-6848. DOI: 10.1039/C8SM00103K. [Online]. Available: https://pubs.rsc.org/en/content/articlelanding/2018/sm/c8sm00103k.

[9] L. L. Howell, *Compliant Mechanisms*. John Wiley & Sons, Aug. 3, 2001, 484 pp., Google-Books-ID: tiiSOuhsIfgC, ISBN: 978-0-471-38478-6.

[10] M. Arya, N. Lee, and S. Pellegrino, "Crease-free biaxial packaging of thick membranes with slipping folds," *International Journal of Solids and Structures*, vol. 108, pp. 24–39, Mar. 1, 2017, ISSN: 0020-7683. DOI: 10.1016/j.ijsolstr.2016.08.013. [Online]. Available: https://www.sciencedirect.com/science/article/pii/S0020768316302232.

[11] M. Arya, F. S. Mechentel, D. R. Webb, *et al.*, "Demonstration of deployment repeatability of key subsystems of a furled starshade architecture," *Journal of Astronomical Telescopes, Instruments, and Systems*, vol. 7, no. 2, p. 021 202, Jan. 2021, Publisher: SPIE, ISSN: 2329-4124, 2329-4221. DOI: 10.1117/1.JATIS.7.2.021202. [Online]. Available: https://www.spiedigitallibrary.org/journals/Journal-of-Astronomical-Telescopes-Instruments-and-Systems/volume-7/issue-2/021202/Demonstration-of-deployment-repeatability-of-key-subsystems-of-a-furled/10.1117/1.JATIS.7.2.021202.full.

[12] J. Küpfer and H. Finkelmann, "Nematic liquid single crystal elastomers," *Die Makromolekulare Chemie, Rapid Communications*, vol. 12, no. 12, pp. 717–726, 1991, _eprint: https://onlinelibrary.wiley.com/doi/pdf/10.1002/marc.1991.030121211, ISSN: 0173-2803. DOI: 10.1002/marc.1991.030121211. [Online]. Available: https://onlinelibrary.wiley.com/doi/abs/10.1002/marc.1991.030121211.

[13] M. Clampin, "Status of the James Webb Space Telescope (JWST)," in *Space Telescopes and Instrumentation 2008: Optical, Infrared, and Millimeter*, vol. 7010, SPIE, Jul. 2008, pp. 192–198. DOI: 10.1117/12.790388. [Online]. Available: https://www.spiedigitallibrary.org/conference-proceedings-of-spie/7010/70100L/Status-of-the-James-Webb-Space-Telescope-JWST/10.1117/12.790388.full.

[14] W. Liu and J. J. Talghader, "Current-controlled curvature of coated micromirrors," *Optics Letters*, vol. 28, no. 11, pp. 932–934, Jun. 1, 2003, Publisher: Optica Publishing Group, ISSN: 1539-4794. DOI: 10.1364/OL.28.000932. [Online]. Available: https://opg.optica.org/ol/abstract.cfm?uri=ol-28-11-932.

[15] E. Peral, S. Tanelli, Z. Haddad, O. Sy, G. Stephens, and E. Im, "Raincube: A proposed constellation of precipitation profiling radars in CubeSat," in *2015 IEEE International Geoscience and Remote Sensing Symposium (IGARSS)*,

ISSN: 2153-7003, Jul. 2015, pp. 1261–1264. DOI: 10.1109/IGARSS.2015.7326003. [Online]. Available: https://ieeexplore.ieee.org/document/7326003.

[16] C. F. Gauss, "Disquisitiones generales circa superficies curvas typis diterici-anis," 1828.

[17] Y. Tang and J. Yin, "Design of cut unit geometry in hierarchical kirigami-based auxetic metamaterials for high stretchability and compressibility," en, *Extreme Mechanics Letters*, vol. 12, pp. 77–85, Apr. 2017, ISSN: 23524316. DOI: 10.1016/j.eml.2016.07.005. [Online]. Available: https://linkinghub.elsevier.com/retrieve/pii/S235243161630058X.

[18] E. T. Filipov, T. Tachi, and G. H. Paulino, "Origami tubes assembled into stiff, yet reconfigurable structures and metamaterials," *Proceedings of the National Academy of Sciences*, vol. 112, no. 40, pp. 12 321–12 326, Oct. 6, 2015, Publisher: Proceedings of the National Academy of Sciences. DOI: 10.1073/pnas.1509465112. [Online]. Available: https://www.pnas.org/doi/10.1073/pnas.1509465112.

[19] J. T. B. Overvelde, J. C. Weaver, C. Hoberman, and K. Bertoldi, "Rational design of reconfigurable prismatic architected materials," *Nature*, vol. 541, no. 7637, pp. 347–352, Jan. 2017, ISSN: 0028-0836, 1476-4687. DOI: 10.1038/nature20824. [Online]. Available: https://www.nature.com/articles/nature20824.

[20] L. H. Dudte, E. Vouga, T. Tachi, and L. Mahadevan, "Programming curvature using origami tessellations," *Nature Materials*, vol. 15, no. 5, pp. 583–588, May 2016, Publisher: Nature Publishing Group, ISSN: 1476-4660. DOI: 10.1038/nmat4540. [Online]. Available: https://www.nature.com/articles/nmat4540.

[21] J. N. Grima, V. Zammit, R. Gatt, A. Alderson, and K. E. Evans, "Auxetic behaviour from rotating semi-rigid units," *physica status solidi (b)*, vol. 244, no. 3, pp. 866–882, Mar. 2007, ISSN: 0370-1972, 1521-3951. DOI: 10.1002/pssb.200572706. [Online]. Available: https://onlinelibrary.wiley.com/doi/10.1002/pssb.200572706.

[22] L. J. Gibson and M. F. Ashby, *Cellular Solids: Structure and Properties* (Cambridge Solid State Science Series), 2nd ed. Cambridge: Cambridge University Press, 1997, ISBN: 978-0-521-49911-8. DOI: 10.1017/CBO9781139878326. [Online]. Available: https://www.cambridge.org/core/books/cellular-solids/BC25789552BAA8E3CAD5E1D105612AB5.

[23] G. W. Milton, *The Theory of Composites* (Cambridge Monographs on Applied and Computational Mathematics). Cambridge: Cambridge University Press, 2002. DOI: 10.1017/CBO9780511613357. [Online]. Available: https://www.cambridge.org/core/books/theory-of-composites/DDFAE9A8E827C0F6178FC2DDE8877AD7.

[24] J. Vinson, *The Behavior of Sandwich Structures of Isotropic and Composite Materials*. New York: Routledge, May 2018, ISBN: 978-0-203-73710-1. DOI: 10.1201/9780203737101.

[25] M. Kadic, G. W. Milton, M. van Hecke, and M. Wegener, "3d metamaterials," *Nature Reviews Physics*, vol. 1, no. 3, pp. 198–210, Mar. 2019, Publisher: Nature Publishing Group, ISSN: 2522-5820. DOI: 10.1038/s42254-018-0018-y. [Online]. Available: https://www.nature.com/articles/s42254-018-0018-y.

[26] J. B. Berger, H. N. G. Wadley, and R. M. McMeeking, "Mechanical metamaterials at the theoretical limit of isotropic elastic stiffness," en, *Nature*, vol. 543, no. 7646, pp. 533–537, Mar. 2017, Publisher: Nature Publishing Group, ISSN: 1476-4687. DOI: 10.1038/nature21075. [Online]. Available: https://www.nature.com/articles/nature21075.

[27] I. Gibson, D. Rosen, and B. Stucker, *Additive Manufacturing Technologies: 3D Printing, Rapid Prototyping, and Direct Digital Manufacturing*, en. New York, NY: Springer, 2015, ISBN: 978-1-4939-2112-6 978-1-4939-2113-3. DOI: 10.1007/978-1-4939-2113-3. [Online]. Available: https://link.springer.com/10.1007/978-1-4939-2113-3.

[28] T. A. Schaedler, A. J. Jacobsen, A. Torrents, *et al.*, "Ultralight metallic microlattices," *Science*, vol. 334, no. 6058, pp. 962–965, Nov. 18, 2011, Publisher: American Association for the Advancement of Science. DOI: 10.1126/science.1211649. [Online]. Available: https://www.science.org/doi/10.1126/science.1211649.

[29] A. Rafsanjani and D. Pasini, "Bistable auxetic mechanical metamaterials inspired by ancient geometric motifs," *Extreme Mechanics Letters*, vol. 9, pp. 291–296, Dec. 1, 2016, ISSN: 2352-4316. DOI: 10.1016/j.eml.2016.09.001. [Online]. Available: https://www.sciencedirect.com/science/article/pii/S2352431616301298.

[30] H. C. Greenberg, M. L. Gong, S. P. Magleby, and L. L. Howell, "Identifying links between origami and compliant mechanisms," *Mechanical Sciences*, vol. 2, no. 2, pp. 217–225, Dec. 12, 2011, Publisher: Copernicus GmbH, ISSN: 2191-9151. DOI: 10.5194/ms-2-217-2011. [Online]. Available: https://ms.copernicus.org/articles/2/217/2011/.

[31] P. Celli, A. Lamaro, C. McMahan, P. Bordeenithikasem, D. C. Hofmann, and C. Daraio, "Compliant morphing structures from twisted bulk metallic glass ribbons," *Journal of the Mechanics and Physics of Solids*, vol. 145, p. 104 129, Dec. 1, 2020, ISSN: 0022-5096. DOI: 10.1016/j.jmps.2020.104129. [Online]. Available: https://www.sciencedirect.com/science/article/pii/S002250962030363X.

[32] E. Ferraro, J. Gasterstädt, and J. Wahl, "Anforderungsstrukturen inklusivmedialen pädagogischen Handelns," *MedienPädagogik: Zeitschrift für Theorie und Praxis der Medienbildung*, vol. 41, pp. 1–14, Feb. 1, 2021, ISSN: 1424-3636. DOI: 10.21240/mpaed/41/2021.02.01.X. [Online]. Available: https://www.medienpaed.com/article/view/1127.

[33] P. Celli, C. McMahan, B. Ramirez, *et al.*, "Shape-morphing architected sheets with non-periodic cut patterns," *Soft Matter*, vol. 14, no. 48, pp. 9744–9749, 2018, ISSN: 1744-683X, 1744-6848. DOI: 10.1039/C8SM02082E. [Online]. Available: https://xlink.rsc.org/?DOI=C8SM02082E.

[34] J. M. McCracken, B. R. Donovan, and T. J. White, "Materials as machines," *Advanced Materials*, vol. 32, no. 20, p. 1 906 564, 2020. DOI: https://doi.org/10.1002/adma.201906564.

[35] M. Behl, K. Kratz, J. Zotzmann, U. Nöchel, and A. Lendlein, "Reversible bidirectional shape-memory polymers," *Advanced Materials*, vol. 25, no. 32, pp. 4466–4469, 2013, _eprint: https://onlinelibrary.wiley.com/doi/pdf/10.1002/adma.201300880, ISSN: 1521-4095. DOI: 10.1002/adma.201300880. [Online]. Available: https://onlinelibrary.wiley.com/doi/abs/10.1002/adma.201300880.

[36] F. Ilievski, A. D. Mazzeo, R. F. Shepherd, X. Chen, and G. M. Whitesides, "Soft robotics for chemists," *Angewandte Chemie International Edition*, vol. 50, no. 8, pp. 1890–1895, 2011, ISSN: 1521-3773. DOI: 10.1002/anie.201006464. [Online]. Available: https://onlinelibrary.wiley.com/doi/abs/10.1002/anie.201006464.

[37] M. K. McBride, M. Podgorski, S. Chatani, B. T. Worrell, and C. N. Bowman, "Thermoreversible folding as a route to the unique shape-memory character in ductile polymer networks," *ACS Applied Materials & Interfaces*, vol. 10, no. 26, pp. 22 739–22 745, Jul. 5, 2018, ISSN: 1944-8244, 1944-8252. DOI: 10.1021/acsami.8b06004. [Online]. Available: https://pubs.acs.org/doi/10.1021/acsami.8b06004.

[38] E. Brown, N. Rodenberg, J. Amend, *et al.*, "Universal robotic gripper based on the jamming of granular material," *Proceedings of the National Academy of Sciences*, vol. 107, no. 44, pp. 18 809–18 814, 2010. DOI: 10.1073/pnas.1003250107.

[39] X. Chen, L. W. Taylor, and L.-J. Tsai, "An overview on fabrication of three-dimensional woven textile preforms for composites," *Textile Research Journal*, vol. 81, no. 9, pp. 932–944, Jun. 1, 2011, Publisher: SAGE Publications Ltd STM, ISSN: 0040-5175. DOI: 10.1177/0040517510392471. [Online]. Available: https://doi.org/10.1177/0040517510392471.

[40] J. Engel and C. Liu, "Creation of a metallic micromachined chain mail fabric," *Journal of Micromechanics and Microengineering*, vol. 17, no. 3, p. 551, Feb.

2007, ISSN: 0960-1317. DOI: 10.1088/0960-1317/17/3/018. [Online]. Available: https://dx.doi.org/10.1088/0960-1317/17/3/018.

[41] P. Bartkowski, H. Bukowiecki, F. Gawiński, and R. Zalewski, "Adaptive crash energy absorber based on a granular jamming mechanism," *Bulletin of the Polish Academy of Sciences Technical Sciences; 2022; 70; 1; e139002*, 2022, ISSN: 2300-1917. [Online]. Available: https://journals.pan.pl/dlibra/publication/139002/edition/120817.

[42] H. M. Jaeger, "Celebrating soft matter's 10th anniversary: Toward jamming by design," *Soft Matter*, vol. 11, pp. 12–27, 1 2015. DOI: 10.1039/C4SM01923G.

[43] A. J. Liu and S. R. Nagel, "Jamming is not just cool any more," en, *Nature*, vol. 396, no. 6706, pp. 21–22, Nov. 1998, Publisher: Nature Publishing Group, ISSN: 1476-4687. DOI: 10.1038/23819. [Online]. Available: https://www.nature.com/articles/23819.

[44] D. Bi, J. Zhang, B. Chakraborty, and R. P. Behringer, "Jamming by shear," en, *Nature*, vol. 480, no. 7377, pp. 355–358, Dec. 2011, Publisher: Nature Publishing Group, ISSN: 1476-4687. DOI: 10.1038/nature10667. [Online]. Available: https://www.nature.com/articles/nature10667.

[45] J. Mueller, K. H. Matlack, K. Shea, and C. Daraio, "Energy absorption properties of periodic and stochastic 3d lattice materials," *Advanced Theory and Simulations*, vol. 2, no. 10, p. 1 900 081, 2019. DOI: https://doi.org/10.1002/adts.201900081. eprint: https://advanced.onlinelibrary.wiley.com/doi/pdf/10.1002/adts.201900081. [Online]. Available: https://advanced.onlinelibrary.wiley.com/doi/abs/10.1002/adts.201900081.

[46] R. Guseinov, C. McMahan, P. Jesus, C. Daraio, and B. Bickel, "Programming temporal morphing of self-actuated shells," *Nat Commun*, vol. 11, no. 1, Jan. 2020, ISSN: 0730-0301. DOI: 10.1038/s41467-019-14015-2. [Online]. Available: https://doi.org/10.1145/3072959.3073709.

[47] Y. Wang, L. Li, D. Hofmann, J. Andrade, and C. Daraio, "Structured fabrics with tunable mechanical properties," *Nature*, vol. 596, pp. 238–243, 2021. DOI: https://doi.org/10.1016/j.mechrescom.2018.07.002.

[48] M. Stoppa and A. Chiolerio, "Wearable electronics and smart textiles: A critical review," *Sensors*, vol. 14, no. 7, pp. 11 957–11 992, Jul. 2014, Number: 7 Publisher: Multidisciplinary Digital Publishing Institute, ISSN: 1424-8220. DOI: 10.3390/s140711957. [Online]. Available: https://www.mdpi.com/1424-8220/14/7/11957.

[49] S. Mondal, "Phase change materials for smart textiles – an overview," *Applied Thermal Engineering*, vol. 28, no. 11, pp. 1536–1550, Aug. 1, 2008, ISSN: 1359-4311. DOI: 10.1016/j.applthermaleng.2007.08.009. [Online]. Available: https://www.sciencedirect.com/science/article/pii/S1359431107002876.

[50] B. Gauvreau, N. Guo, K. Schicker, *et al.*, "Color-changing and color-tunable photonic bandgap fiber textiles," *Optics Express*, vol. 16, no. 20, pp. 15 677–15 693, Sep. 29, 2008, Publisher: Optica Publishing Group, ISSN: 1094-4087. DOI: 10.1364/OE.16.015677. [Online]. Available: https://opg.optica.org/oe/abstract.cfm?uri=oe-16-20-15677.

[51] J. Chen, Y. Huang, N. Zhang, *et al.*, "Micro-cable structured textile for simultaneously harvesting solar and mechanical energy," *Nature Energy*, vol. 1, no. 10, pp. 1–8, Sep. 12, 2016, Publisher: Nature Publishing Group, ISSN: 2058-7546. DOI: 10.1038/nenergy.2016.138. [Online]. Available: https://www.nature.com/articles/nenergy2016138.

[52] K. Cherenack and L. van Pieterson, "Smart textiles: Challenges and opportunities," *Journal of Applied Physics*, vol. 112, no. 9, p. 091 301, Nov. 7, 2012, ISSN: 0021-8979. DOI: 10.1063/1.4742728. [Online]. Available: https://doi.org/10.1063/1.4742728.

[53] K. Cherenack, C. Zysset, T. Kinkeldei, N. Münzenrieder, and G. Tröster, "Woven electronic fibers with sensing and display functions for smart textiles," *Advanced Materials*, vol. 22, no. 45, pp. 5178–5182, 2010, _eprint: https://onlinelibrary.wiley.com/doi/pdf/10.1002/adma.201002159, ISSN: 1521-4095. DOI: 10.1002/adma.201002159. [Online]. Available: https://onlinelibrary.wiley.com/doi/abs/10.1002/adma.201002159.

[54] Z. Wang, N. M. Freris, and X. Wei, "SpiRobs: Logarithmic spiral-shaped robots for versatile grasping across scales," *Device*, p. 100 646, Dec. 6, 2024, ISSN: 2666-9986. DOI: 10.1016/j.device.2024.100646. [Online]. Available: https://www.sciencedirect.com/science/article/pii/S2666998624006033.

Chapter 2

ROLE OF FRICTION AND GEOMETRY IN TUNING THE BENDING STIFFNESS OF TOPOLOGICALLY INTERLOCKING MATERIALS

[1] T. Lu, Z. Zhou, P. Bordeenithikasem, *et al.*, "Role of friction and geometry in tuning the bending stiffness of topologically interlocking materials," *Extreme Mechanics Letters*, vol. 71, p. 102 212, Sep. 1, 2024, ISSN: 2352-4316. DOI: 10.1016/j.eml.2024.102212. [Online]. Available: https://www.sciencedirect.com/science/article/pii/S2352431624000920.

2.1 Introduction

The demand for materials with adjustable physical properties and the ability to respond rapidly to environmental stimuli has been growing [1]. In particular, fabrics with adaptable or tunable stiffness are applicable for use in soft robotics, shape morphing structures, and wearable devices [2]–[4]. For example, tunable fabrics can find use in wearable medical devices, like exoskeletons, haptic systems, and reconfigurable medical supports [5]–[7]. At larger scales, applications of tunable fabrics include transportable and reconfigurable architectures, which transition from a compact and flexible state to a deployed and rigid state [8], [9].

Incorporating interlocking particles in fabrics opens up the possibility to incorporate added structural support and adjustable mechanical properties [10]–[13]. The mechanical behavior of such structured fabrics or topologically interlocking materials (TIM) is determined by the characteristics of their constituents and the topology of their arrangement [11], [14]–[16]. In most architected materials and woven fabrics, these mechanical behaviors are determined during the design process and remain fixed after the components are fabricated. However, in some realizations, the fabric properties can be adjusted through actuation [13], [17]. Wang, et al. demonstrated architected fabrics consisting of chain mail layers with interconnected particles, which demonstrate the ability to reversibly and gradually switch between soft and rigid states [2], [16], [17]. The control of the fabrics' stiffness is achieved by applying pressure at the boundary that jams the particles via vacuum suction, in a system similar to other structured fabrics [2], [4], [8]. While this example demonstrates the ability to create architected fabrics with tunable properties, the use of vacuum

actuation is not practical, because it requires bulky and energy intensive pumping systems. Using tensioned fibers or artificial muscles could be a more compact and power-efficient solution [18].

In this paper, we study the response of a particular TIM system, consisting of truncated tetrahedral particles connected by woven tension wires [13], [15], [16]. Unlike the TIM system that is held solely by geometric interlocking and external in-plane constraint, which exhibits a softening stage before the TIM collapses [13], our fabric-TIM system shows a stiffening response during the indentation tests due to the gradual increment of anti-separation forces provided by the wires. The connecting wires facilitate the tunability of the bending modulus in response to adjustable applied tension, as demonstrated in Fig. 2.4c and d [16], [17]. Additionally, they enable the formation of various flexible shapes while keeping the TIM structure intact. To better understand the fundamental mechanisms governing the tunability of the TIM system's apparent bending stiffness, we explore the role of contact angle and contact friction at a fixed applied wire tension, using experiments and numerical simulations.

2.2 Design and Fabrication of the Topologically Interlocking Material Structured Fabric

There are various designs of TIMs. For example, Dyskin, et al. [10] used tetrahedral solids to form layer-like structures that are interlocked topologically. TIM systems can be used for architectural designs and other global surfaces as shown in Fig. 2.1. Molotnikov, et al. [17] constructed TIM systems made of osteomorphic blocks embedded with shape memory alloy wires that can alter the TIM's flexural stiffness when activated. Siegmund et al. [16] created TIM systems using truncated tetrahedron blocks integrated with internal constraint fibers or woven tow material, demonstrating interlocking systems confined by passive elements.

The tetrahedron was selected for its relevance in topological interlocking, a design principle where blocks are held together without physical or adhesive joining. Topological interlocking relies on geometric and kinematic constraints, with the structure maintained by a global peripheral constraint and an arrangement of specially shaped elements. Unlike conventional interlocking, it avoids keys or connectors, which prevents crack propagation across blocks, but more importantly allows for modifications to make the structure more adaptable. This approach combines the flexibility and damage tolerance of fragmented materials with the overall structural integrity of

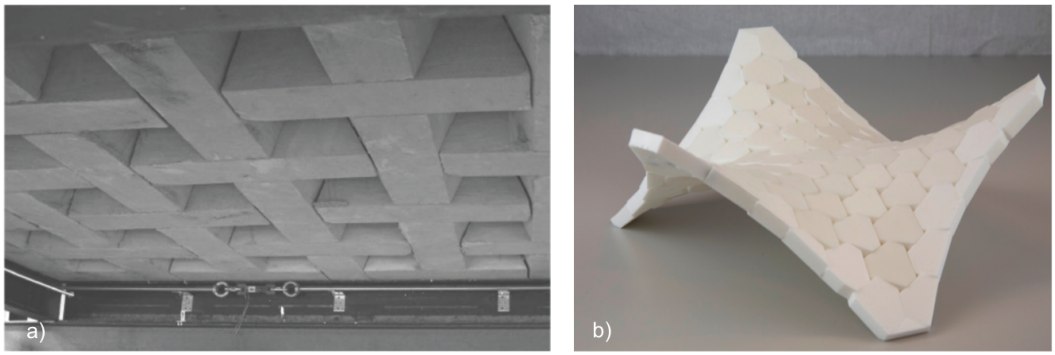

Figure 2.1: (a) An example of the stability of interlocked truncated tetrahedra in architecture [11]. (b) An example of other stable shapes that can be achieved with topological interlocking [19].

a unified system, and its scale-independent nature makes it applicable across various sizes.

The architecture of interlocking assemblies can be understood by examining the evolution of planar cross-sections of a layer-like arrangement of tetrahedra as the plane moves in the normal direction [20]. Starting with the middle section, which is a pattern of tiled squares, the pattern transforms into rectangles and ultimately degenerates into lines (edges of the tetrahedra) as the plane moves upward. A similar transformation occurs when moving downward, with rectangles rotated by 90°. Interlocking is achieved because a reference block is obstructed by adjacent blocks in all directions—upward, downward, and sideways—due to the inclined faces of its neighbors. This ensures the reference block cannot be removed through any combination of displacements or rotations.

Using this principle, interlocking assemblies can also be constructed with other platonic solids, as demonstrated in Fig. 2.3. Solids with hexagonal cross-sections, such as cubes, octahedra, and dodecahedra, can form interlocked arrangements using a honeycomb pattern. In these assemblies, the reference element is locked topologically by its shape and the arrangement of its neighbors, preventing movement through the channels formed by adjacent elements. This principle of translational interlocking can be rigorously described by the degeneration of polygonal cross-sections into segments or points as the plane shifts.

Certain truncations of these solids can be applied without compromising their interlocking properties. However, increasing the degree of truncation to a point where

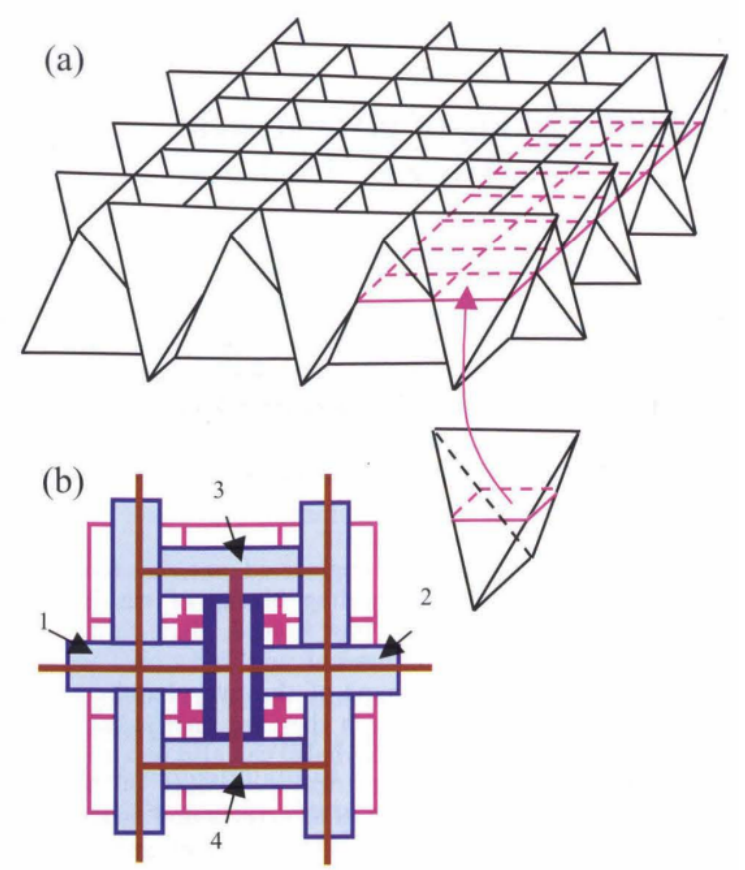

Figure 2.2: Layer-like assembly of interlocked tetrahedra. (a) Overview of assembly. (b) Evolution of the planar section through the assembly. Magenta lines indicate a fragment of the middle section, shaded blue rectangles correspond to the section moved from the middle section half way up, and black and brown lines indicate the sections that have degenerated into the upper edges (seen when one looks on the assembly from the top). Bold lines delineate sections of a reference block [20].

the interlocking is partially affected can be advantageous for enhancing the flexibility of the structure. This is particularly beneficial in the systems of our samples, where structural stability relies less on interlocking alone, as the supporting wires integrated into the design for actuation also provide stabilization.

Additionally, tetrahedrons have a trapezoidal cross section, and trapezoidal particles are known for their substantial contact surfaces [12] and have extensive applications in architected materials to enhance mechanical performance [21]. Drawing inspiration from the previous references, we study a classic system of a TIM assembled with truncated tetrahedron particles as the basic building blocks (Fig. 2.4a). Using truncated tetrahedrons, as opposed to osteomorphic blocks, allows us to systemat-

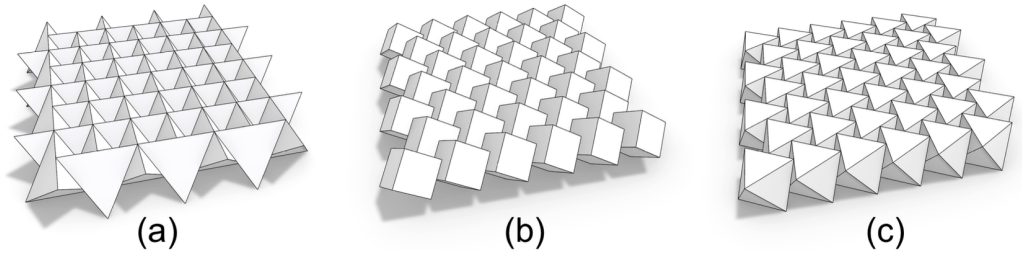

Figure 2.3: Example planar topologically interlocking assemblies described in [Dyskin et al. 2003 [20]] composed of (a) tetrahedrons, (b) cubes, and (c) octahedrons. Image from [19].

ically change a single parameter, such as dihedral angle, to dictate the amount of interlocking. Moreover, since truncated tetrahedrons don't completely fit into each other, the relaxed state is more flexible and similar to a fabric. Inspired by Siegmund et al. [16], we design the particles with longitudinal and latitudinal through-holes. We use nylon wires to weave through each discrete particle and interconnect them, as depicted in Fig. 2.4b. To actuate the fabrics, we apply different levels of tension to the wires and thereby jam the particles with their neighbors to form an interlocked state (Fig. 2.4c–d). The combined outer surface of the truncated tetrahedrons upon post-tensioning is a flat plane. The resulting assemblies possess geometric contact and interlocking periodicity.

A series of TIMs were produced by varying two different particle parameters: the particle's dihedral angles, θ (Fig. 2.4a) and their surface friction. The particles were fabricated with three different dihedral angles, 60°, 70° and 90°, where the latter is simply a prism geometry with no geometric interlocking (Fig. 2.5). To vary the surface friction, we 3D-printed the particles using two different materials of similar stiffness: Vero White (VW) using an Objet Stratasys Connex 500 (Fig. 2.5a), and Nylon Polyamide 12 (PA12) using a Sintratec SLS 3D printer (Fig. 2.5b). Particles were cleaned by removing the outer support material. The Vero White particles were additionally cleaned in a 2-percent aqueous solution of NaOH to remove the remaining support material. The coefficients of friction were determined experimentally after the particles had been cleaned, using sliding friction tests. The resulting surface friction coefficients were measured to be 0.2 and 0.6, respectively. The particles were then woven together with 0.3 mm diameter nylon wire. The system is subsequently actuated with a small motor (28BYJ-48 Stepper Motor) that

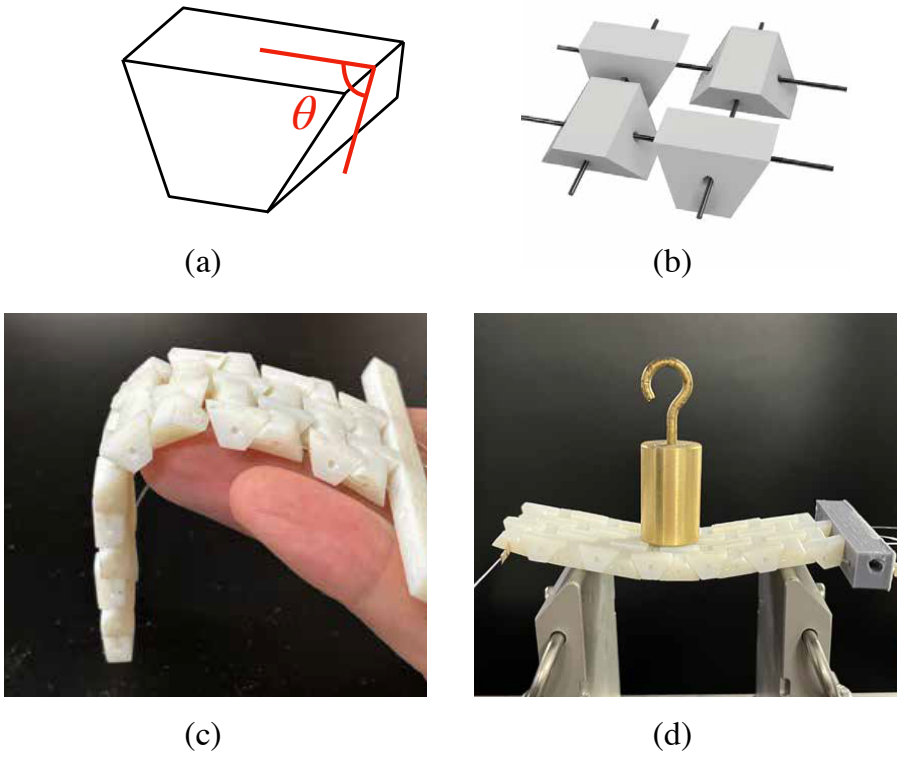

Figure 2.4: (a) Schematic of a basic building block (particle) in the shape of a truncated tetrahedron [10], with dihedral angle, θ, between the truncating surface and the side surface of particle; (b) Schematic of particles inter-connected by post-tensioned wires; (c) Unactuated, soft state of the sample; (d) Actuated, stiff state of the sample.

controls the amount of wire tension and therefore jamming the particles. A custom-designed fixture was 3D-printed for the motor housing and tensioning mechanism with sufficient clearance space for the tension meter (Checkline ETB-2000). The tension should attain the predetermined threshold, ensuring that the wire remains within the elastic range during the testing phase. The tension meter was used to gauge the tension and determine whether to incrementally increase the tension by spinning the motor. Once the desired average tension was achieved in the wires, the tension was secured with clamp beads to hold the wire in place. Then the woven sample was removed from the fixture with the motor.

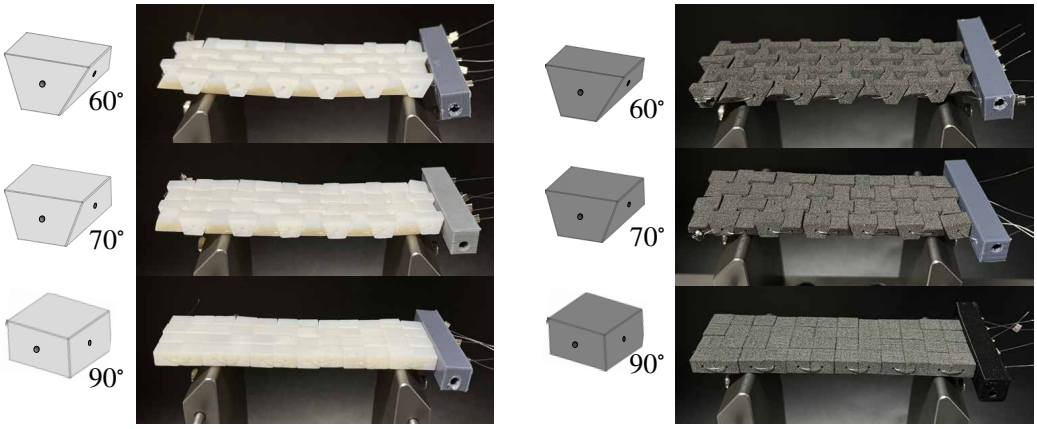

Figure 2.5: Samples made by particles with $\theta = 60°$, $70°$, and $90°$; Samples shown in (a) are made by Vero White, with a measured friction coefficient of 0.2; samples shown in (b) are made by Nylon Polyamide 12, with a measured friction coefficient of 0.6.

2.3 Simulations

For a more systematic analysis of the TIM fabrics' behavior as a function of particle's geometry and constituent material properties, a reliable and validated numerical model is necessary. Level Set Discrete Element Method (LS-DEM) is used to model the physical experiment. LS-DEM is a variant of the traditional Discrete Element Method (DEM) allowing arbitrary object shapes. Originally developed for granular applications [22], [23], LS-DEM has recently been adapted to study the structural behaviors of multi-block structures [24], [25], and the structural analysis of TIM, showing satisfactory results in capturing the slip-governed failure [26], [27] and the deflection limit [28] of the slab-like TIM. LS-DEM uses level set functions as the geometric basis, which calculates the signed distance ϕ from any arbitrary point in the space to the nearest surface of the grain. For example, in this work, a cross-sectional slice of a basic building block, which is the shape of a truncated tetrahedron, is a trapezoid in 2D, as shown in Fig. 2.6a. The surface of the building block, or particle, can be reconstructed by $\phi = 0$. We impose a set of surface nodes with uniform discretization size onto each particle (Fig. 2.6b). When checking potential particle contact, we take the position of each surface node $\mathbf{x}$ of one particle and check the corresponding level set value from another neighboring particle. If $\phi(\mathbf{x}) \leq 0$, then contact exists between this pair of particles.

Given the discrete nature of the woven-connected particles, LS-DEM is capable of extracting particle-scale information at micro-mechanical level, thus providing insight into how friction and contacts between particles affect the macroscopic property such as sample bending stiffness. Furthermore, the use of level set function provides flexibility in particle shape control, allowing us to easily simulate different particle shapes and investigate the combined geometric shape effects to the sample's overall behavior. The use of LS-DEM is also computationally efficient compared to other simulation methods such as Finite Element Method (FEM) for potential simulations of large ensembles of particles [29].

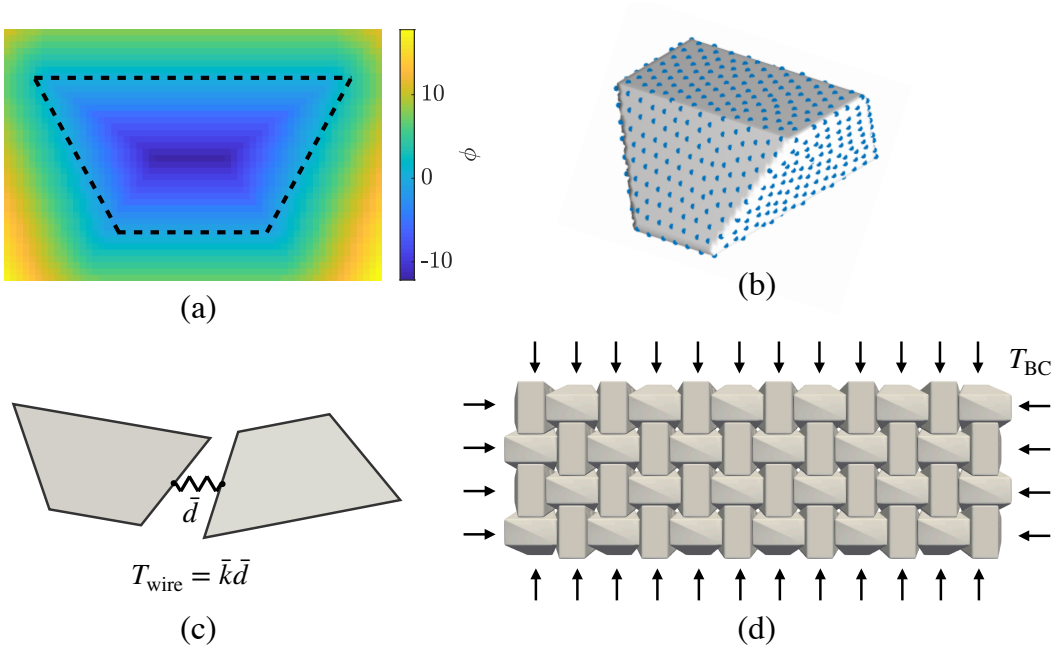

Figure 2.6: (a) Illustration of the level set matrix of a slice of the truncated tetrahedron; (b) The particle is reconstructed by surfaces with $\phi = 0$; the imposed surface nodes are shown in blue dots; (c) Illustration of a pair of neighboring particles, connected by a massless spring with stiffness $\bar{k}$ and elongation $\bar{d}$; (d) Illustration of the sample under post-tensioning force T_{BC}.

We use point forces acting on the boundary particles T_{BC} to model the post-tensioning effect of the wires (Fig. 2.6d). On top of that, we use massless springs connecting the face center of the side of each particle to the face center of the side of its neighbors (Fig. 2.6c). The neutral position of the spring is at a distance $\bar{d} = 0$. The springs connecting neighboring particles can only exert tensile forces on the connected particles. When two neighboring particles are separated, the wire force

T_{wire} is calculated as:

$$T_{\text{wire}} = \bar{k}\bar{d} \tag{2.1}$$

where $\bar{k}$ is the stiffness of the spring and is calibrated to match the experimental result of an uniaxial tension test carried out on a single woven wire.

2.4 Mechanical Characterizations

In order to experimentally investigate the macroscopic properties of the sample under various particle geometries and material properties, displacement-controlled three-point bending tests were performed with an Instron E3000 Mechanical Testing Machine (Fig. 2.7a). The indenter had a set loading rate of 0.5 mm s^{-1}. To ensure that the TIM systems deform within their components' elastic limits, we imposed a maximum indentation depth of 5 mm. This indentation depth was determined by performing three-point bending tests on 3D-printed slabs of the same material with the same fabric sample dimensions. Tests show no yielding behavior within 5 mm. This indentation depth also guarantees that the wire remains within its elastic limit, confirmed by independent tensile tests on the wire, aligning with the assumption made in Eqn. 2.1.

To compare the bending performance of the different fabrics, we define an apparent elastic bending modulus, E^*, as [2]:

$$E^* = \frac{KL^3}{4bh^3}. \tag{2.2}$$

Here, K is the stiffness of the initial linear regime of the force-displacement plot obtained from the test machine, L is the support span, b is the width of the sample, and h is the thickness of the sample before testing.

We study the role of friction and particle's shape on the overall fabric's behavior, comparing the apparent bending moduli values extracted from the experiments. Fig. 2.7b shows an overview of the bending modulus calculated from Fig. 2.7c–d using Eqn. 2.2. Both increasing surface irregularities (i.e., friction between particles) and geometric interlocking have a positive correlation with the bending modulus. Samples made with PA12, resulting in a higher surface friction coefficient ($\mu = 0.6$) than those made with Vero White (VW) ($\mu = 0.2$), exhibit almost twice as much bending modulus as VW samples of the same particle geometry. Fig. 2.7c–d show the force-displacement plot for VW samples and PA12 samples accordingly. The force-displacement curves obtained from the three-point bending tests show an initially linear regime at small indentation depths, primarily due to the elastic

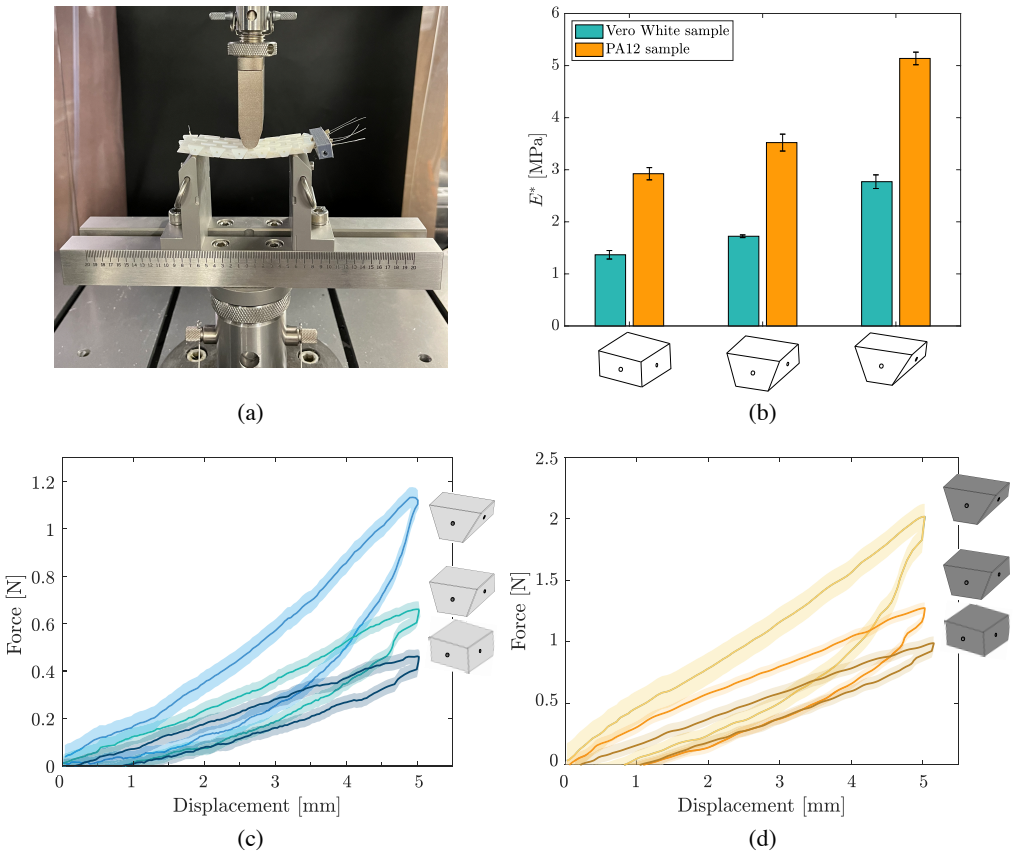

Figure 2.7: (a) The three-point bending test setup with sample; (b) Apparent bending modulus of the different samples, fabricated with 2 different constitutive materials (Vero White and PA12) and three different dihedral angles (θ = 60°, 70° and 90°); (c) Force-displacement plots of the Vero White samples; (d) Force-displacement plot of the PA12 samples. In (c) and (d), for each sample, a total of five experiments are performed. The solid lines represent the average force-displacement behavior, and the shaded regions show the standard deviation over five experiments.

response of the wire while the particles spread out. However, as the displacement increases, a nonlinear response is observed, most likely because of frictional sliding and local rearrangement of the particles within the system. Comparing the force-displacement plot within samples of the same material (Fig. 2.7c–d), we see that particles with smaller dihedral angle θ, which result in higher interlocking upon post-tensioning, show higher stiffness. If we compare samples of same particle geometry but made with different materials, samples with higher surface friction show higher stiffness.

For comparison, particles with zero interlocking were fabricated, which were

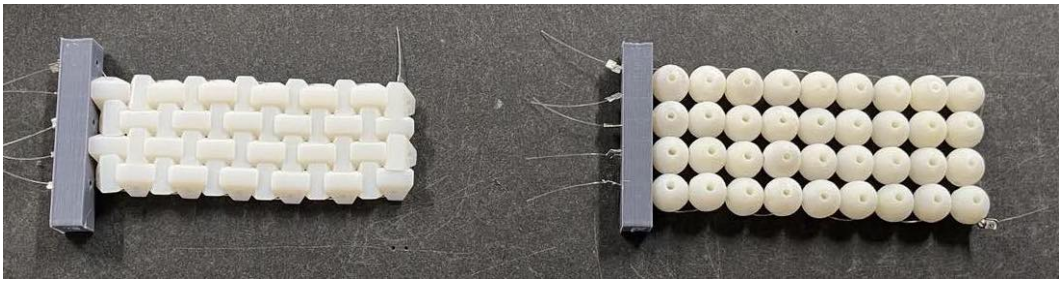

Figure 2.8: Sample with zero interlocking (spherical particles) and its truncated tetrahedral counterparts.

spheres, as shown in Fig. 2.8 with their truncated tetrahedral counterparts. Fig. 2.9a shows the bending torque test setup performed on them. The test samples are attached to a motor to vary the amount of tension in the wires. Two types of particles are tested, the truncated tetrahedron and uniform spheres, each in two different wire tensions, one at 40N and one at 20N. In the test, we bend a test sample from $\theta = 0°$ to 50°.

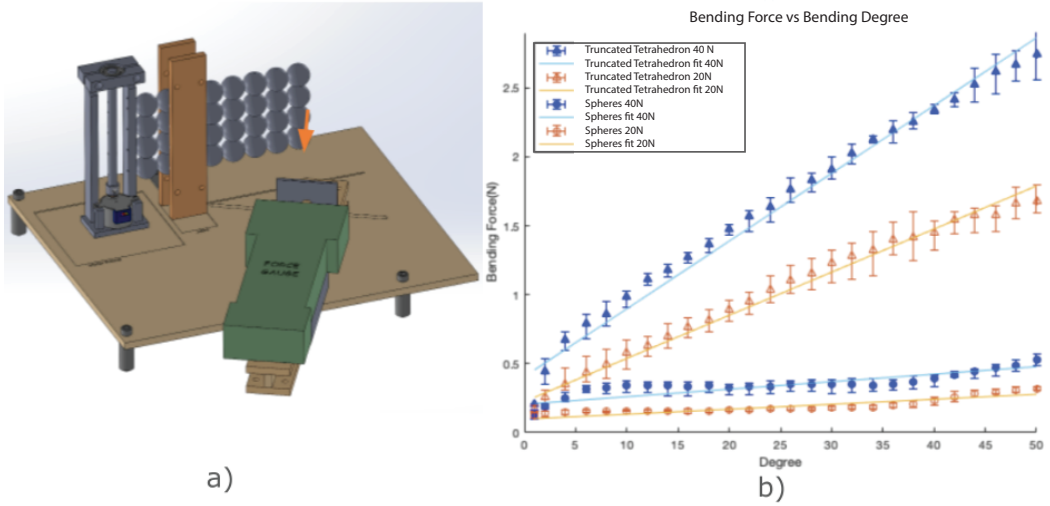

Figure 2.9: (a) Bending torque test setup with sample; (b) Plot of results for the truncated tetrahedron (TT) and spheres at two different wire tensions.

The lever arm is 20 cm. Based on the measured bending force, the bending stiffness (with varying amounts of tension and therefore jamming) of a sample can be roughly calculated as: torque = $0.2Fcos(\theta)$ Nm, where F is the measured bending force from a digital 5N force gauge. From the resulting plot in Fig. 2.9b, we can see that

as more bending occurs, due to the increased degree of bending, the bending force increases. The truncated tetrahedrons are capable of geometric interlocking, so they become harder to bend as the degree of bending increases, unlike the spherical particles which have zero geometric interlocking. Additionally, higher tensions require greater bending force due to increased jamming. However, with spherical particles, the geometry does not effectively support the increased tension, making the rise in bending force almost entirely attributable to the stiffer wire. In contrast, with truncated tetrahedrons, the increased wire stiffness also contributed to enhanced geometric interlocking.

2.5 Numerical Simulations

To construct the numerical model, we first construct the particles using level set functions and surface nodes (Figure 2.6a–b). We then arrange and post-tension the particles (Figure 2.6c–d), as described in the Simulations section. To simulate the testing setup, we construct a 1:1 model of the experiment apparatus using the same level set technique. We then move the indenter downward at a constant loading rate. In the experiments, though the fabrics samples are prepared and post-tensioned according to the same procedure, there is no way to explicitly measure the slack of wires introduced during fabrication, and consequently it is not possible to know the exact tensile forces, T_{BC}, exerted by the wires on all particles. Therefore, we adjust the boundary force T_{BC} in the bending simulation of the 70° VW sample until the simulated apparent bending modulus E^* matches with that of the corresponding experiment. To ensure consistency and uniformity, we then apply the same calibrated boundary force to the remaining five simulations (60° and 90° VW samples, as well as 60°, 70°, and 90° PA12 samples).

As depicted in Fig. 2.10, the resulting calibrated numerical model exhibits good agreement with experimental data regarding the apparent bending modulus E^*. In Fig. 2.10a, we show that as the friction coefficient reaches larger values ($>\sim$0.3), the bending modulus of the samples does not increase as much, particularly for the samples with the least geometric interlocking (rectangular prism particles). As expected, in samples with more interlocked particles, the modulus increases more rapidly with increasing friction coefficient. For the 90° prism particles, the interwoven wire and friction between neighboring particles are the main factors that counteract out-of-plane deflection. With more interlocked particles (60° prism particles), however, not only friction and the wire, but also geometric constraints are collectively counteracting the out-of-plane deflection.

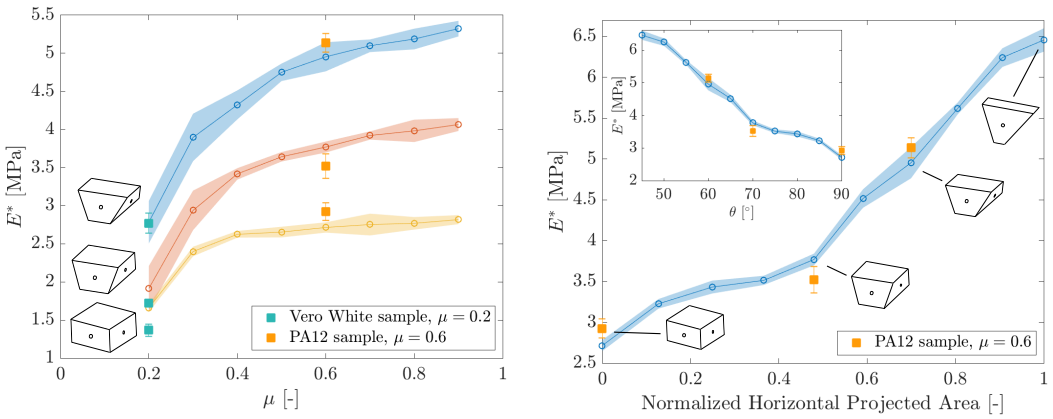

(a) (b)

Figure 2.10: Comparison of experiments and numerical simulations. (a) Simulated bending modulus of samples consisted of particles with $\theta = 60°$, $70°$, and $90°$ across different friction coefficient, from 0.2 to 0.9. For each particle shape at each friction coefficient, five simulations are run. For each run, noise is introduced to the initial particle position, particle orientation and boundary force T_{BC}. The solid line represents the average modulus, while the shaded regions show the standard deviation across five runs. Experiment results obtained from VW ($\mu = 0.2$) and PA12 ($\mu = 0.6$) samples are marked by green and orange respectively; (b) Simulated bending modulus vs. normalized contact area in horizontal projection with particles from $\theta = 45°$ to $\theta = 90°$ with $5°$ increments. The projected contact area is calculated based on the initial configuration of the particle orientation, and is normalized by the area of the $45°$ particle.

Inset: simulated bending modulus vs. θ. Similar to (a), five simulations are run for each particle shape and noise is introduced in the initial state of each simulation. Experiment results from PA12 are marked in orange.

In order to analyze how geometry affects the modulus, we simulate the bending tests of samples made by 7 other particles of different degrees of geometric interlocking. Wang et al. [2] reported a quadratic law relating average particle contact number to the apparent bending modulus. In this work, since all particles are generated with surface nodes of uniform discretization size, the contact number per particle upon contact directly translates to contact area between the contacting neighboring particles. Since we are assuming a small indentation depth, we estimate the contact area to be the maximum area of the side surface of a truncated tetrahedron in contact with its neighbor at initial configuration before indentation, which is one trapezoid overlapped with a flipped trapezoid, or a hexagon. We plot the bending modulus against the normalized contact area projected onto the horizontal plane.

Since the horizontal plane is directly perpendicular to the indenting direction, the projected horizontal contact area acts as the effective contact area for the solid material to counteract the indentation force. From Fig. 2.10b, we see that the bending modulus scales almost linearly with the horizontally projected contact area. The dihedral angle θ scales inverse-linearly with the bending modulus, due to the fact that particles with larger θ have smaller horizontal projected contact areas. From Fig. 2.10b and the additional inset figure, we see that particle geometry is a crucial factor in contributing to the bending modulus.

In contrast to [2], which exhibited a power law relationship, we find an approximately linear scaling between the projected horizontal contact area and the bending stiffness in our samples. We attribute this difference to the presence of the woven wires, which make the samples with less geometric interlocking rely more on elastic wire forces. During indentation, the wires in samples made from the rectangular prism particles are expected to be stretched more compared to samples made from the 45°-particles. This indicates that the wires may exert increased anti-separation forces within the 90°-particle TIMs in contrast to the other particles that can rely on greater geometric interlocking.

2.6 Conclusion

In this paper, we study the role of particles' geometry and inter-particle friction in the bending response of TIM systems consisting of truncated tetrahedron particles woven together with nylon wires. We fabricate samples with particles of varying interlocking contact angles and surface friction. Using LS-DEM simulations, we extended our analysis to investigate how the combined influence of multiple parameters, rather than their individual effects, impacts the apparent bending modulus. In the post-tensioned state, we find that both high friction and large horizontally projected contact area between the neighboring particles contribute positively to the resulting sample's bending resistance. The positive effect of friction to bending stiffness diminishes as friction coefficient increases. The projected horizontal contact area positively contributes to the bending modulus at a linear rate.

The TIM is a complex system with many factors at play. Besides the friction and geometric interlocking, sample thickness and external post-stress also have profound effects on bending response. In order to isolate the effect of friction and geometry, we keep the sample thickness and post-stress consistent throughout all experiments and simulations. More comprehensive studies on the combined effect of all factors

should be investigated in future work. Future studies could explore how varying tension across different regions of the structured fabric can be used to achieve localized stiffness variations within a single structure. In addition, other platonic solids used as particle geometries should be explored, and other particle shapes outside of topological interlocking should also be explored. A brief exploration of this is demonstrated below in Fig. 2.11.

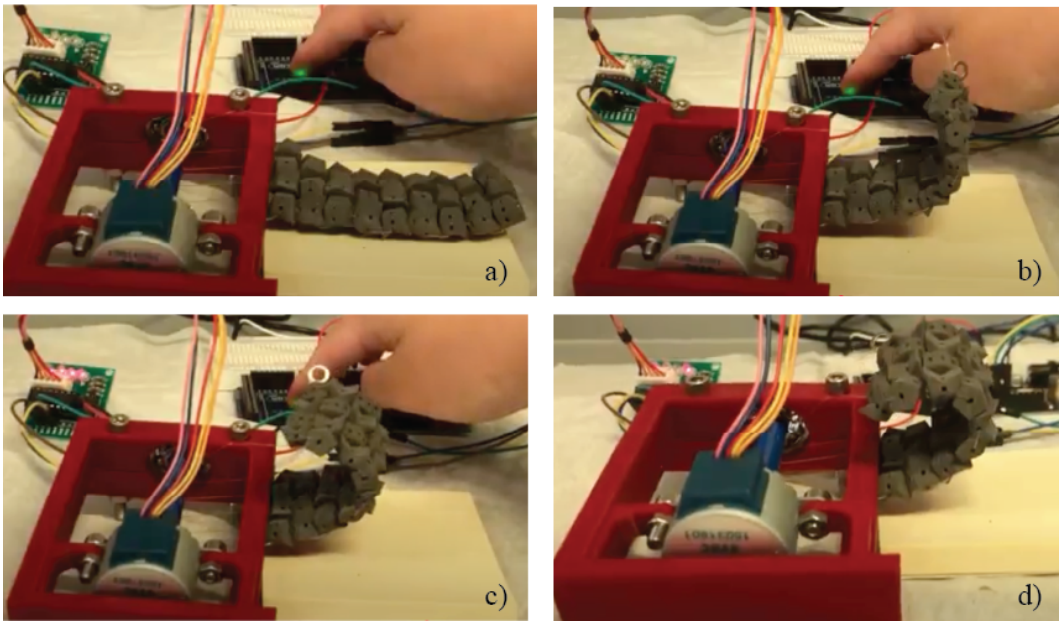

Figure 2.11: Recreating the samples with a different particle design that induces shape change; (a) The sample starts relaxed and in a flat plane; (b) As the small motor increases tension in the wires, the global structure gradually develops curvature as neighboring particles jam at predetermined angles, enabling shape transformation.; (c) The tension in the wires is further increased resulting in more curvature; (d) The sample has achieved its maximum curvature, as neighboring particle pairs have reached their limit of contact. Further increasing the wire tension will not result in additional shape transformation.

Exploring particle geometries without topological interlocking, but instead leveraging edge collisions at specific angles, enables the formation of other global shapes and introduces additional pathways for shape and stiffness modulation [30]. This concept was investigated in Fig. 2.11, where the fabrication and assembly methods remained consistent, but the particle design was modified so that, upon lateral jamming with neighboring particles, an obtuse angle was formed. In this configuration, the sample initially lies relaxed in a flat plane Fig. 2.11a. As a small motor incrementally increases tension in the wires, the global structure gradually develops curvature

as neighboring particles jam at predetermined angles, facilitating controlled shape transformation (Fig. 2.11b). Further tensioning amplifies this curvature (Fig. 2.11c) until the system reaches its maximum curvature, at which point particle pairs achieve their maximum contact. Beyond this point, additional wire tension does not result in further shape change (Fig. 2.11d). This demonstration highlights how geometric tuning of particle interactions, can enable programmable shape morphing and stiffness variation in the structure. These concepts were the inspiration for the next chapter, in which they are further developed.

2.7 Acknowledgments

Part of this research was done at the Jet Propulsion Laboratory (JPL), California Institute of Technology, under contract with NASA (80NM0018D0004). This work was supported by the JPL Researchers on Campus program and Caltech President's and JPL Director's Research and Development Fund. Reference herein to any specific commercial product, process, or service by trade name, trademark, manufacturer, or otherwise, does not constitute or imply its endorsement by the United States Government or the Jet Propulsion Laboratory, California Institute of Technology. J.E.A. and Z.Z. would like to acknowledge the support from the National Science Foundation (NSF) under award number CMMI-2033779, and the U.S. Army Research Office under grant number W911NF-19-1-0245.

2.8 Bibliography

References

[1] M. Stoppa and A. Chiolerio, "Wearable electronics and smart textiles: A critical review," *Sensors*, vol. 14, no. 7, pp. 11 957–11 992, 2014, ISSN: 1424-8220. DOI: 10.3390/s140711957. [Online]. Available: https://www.mdpi.com/1424-8220/14/7/11957.

[2] Y. Wang, L. Li, D. Hofmann, J. Andrade, and C. Daraio, "Structured fabrics with tunable mechanical properties," *Nature*, vol. 596, pp. 238–243, 2021. DOI: https://doi.org/10.1016/j.mechrescom.2018.07.002.

[3] S. Mondal, "Phase change materials for smart textiles – an overview," *Applied Thermal Engineering*, vol. 28, no. 11, pp. 1536–1550, 2008, ISSN: 1359-4311. DOI: https://doi.org/10.1016/j.applthermaleng.2007.08.009.

[4] D. S. Shah, E. J. Yang, M. C. Yuen, E. C. Huang, and R. Kramer-Bottiglio, "Jamming skins that control system rigidity from the surface," *Advanced Functional Materials*, vol. 31, no. 1, p. 2 006 915, 2021. DOI: https://doi.org/10.1002/adfm.202006915.

[5] A. R. Ploszajski, R. Jackson, M. Ransley, and M. Miodownik, "4d printing of magnetically functionalized chainmail for exoskeletal biomedical applications," *MRS Advances*, vol. 4, no. 23, pp. 1361–1366, 2019. DOI: 10.1557/adv.2019.154.

[6] J. M. McCracken, B. R. Donovan, and T. J. White, "Materials as machines," *Advanced Materials*, vol. 32, no. 20, p. 1 906 564, 2020. DOI: https://doi.org/10.1002/adma.201906564.

[7] X. Yang, Z. Wang, B. Zhang, *et al.*, "Self-sensing robotic structures from architectured particle assemblies," *Advanced Intelligent Systems*, vol. 5, no. 1, p. 2 200 250, 2023. DOI: https://doi.org/10.1002/aisy.202200250.

[8] J. Ou, L. Yao, D. Tauber, J. Steimle, R. Niiyama, and H. Ishii, "Jamsheets: Thin interfaces with tunable stiffness enabled by layer jamming," in *Proceedings of the 8th International Conference on Tangible, Embedded and Embodied Interaction*, ser. TEI '14, Munich, Germany: Association for Computing Machinery, 2014, pp. 65–72, ISBN: 9781450326353. DOI: 10.1145/2540930.2540971. [Online]. Available: https://doi.org/10.1145/2540930.2540971.

[9] P. Aejmelaeus-Lindström, J. Willmann, S. Tibbits, F. Gramazio, and M. Kohler, "Jammed architectural structures: Towards large-scale reversible construction," *Granular Matter*, vol. 18, Apr. 2016. DOI: 10.1007/s10035-016-0628-y.

[10] A. Dyskin, Y. Estrin, A. Kanel-Belov, and E. Pasternak, "A new concept in design of materials and structures: Assemblies of interlocked tetrahedron-shaped elements," *Scripta Materialia*, vol. 44, no. 12, pp. 2689–2694, 2001, ISSN: 1359-6462. DOI: https://doi.org/10.1016/S1359-6462(01)00968-X.

[11] Y. Estrin, V. R. Krishnamurthy, and E. Akleman, "Design of architectured materials based on topological and geometrical interlocking," *Journal of Materials Research and Technology*, vol. 15, pp. 1165–1178, 2021, ISSN: 2238-7854. DOI: https://doi.org/10.1016/j.jmrt.2021.08.064.

[12] F. Barthelat, "Architectured materials in engineering and biology: Fabrication, structure, mechanics and performance," *International Materials Reviews*, vol. 60, no. 8, pp. 413–430, 2015. DOI: 10.1179/1743280415Y.0000000008.

[13] S. Khandelwal, T. Siegmund, R. J. Cipra, and J. S. Bolton, "Adaptive mechanical properties of topologically interlocking material systems," *Smart Materials and Structures*, vol. 24, no. 4, p. 045 037, Mar. 2015. DOI: 10.1088/0964-1726/24/4/045037.

[14] A. Molotnikov, R. Gerbrand, O. Bouaziz, and Y. Estrin, "Sandwich panels with a core segmented into topologically interlocked elements," *Advanced Engineering Materials*, vol. 15, no. 8, pp. 728–731, 2013.

[15] Y. Estrin, Y. Beygelzimer, R. Kulagin, *et al.*, "Architecturing materials at mesoscale: Some current trends," *Materials Research Letters*, vol. 9, no. 10, pp. 399–421, 2021. DOI: 10.1080/21663831.2021.1961908.

[16] T. Siegmund, F. Barthelat, R. Cipra, E. Habtour, and J. Riddick, "Manufacture and Mechanics of Topologically Interlocked Material Assemblies," *Applied Mechanics Reviews*, vol. 68, no. 4, p. 040 803, Jul. 2016, ISSN: 0003-6900. DOI: 10.1115/1.4033967.

[17] A. Molotnikov, R. Gerbrand, Y. Qi, G. P. Simon, and Y. Estrin, "Design of responsive materials using topologically interlocked elements," *Smart Materials and Structures*, vol. 24, no. 2, p. 025 034, Jan. 2015. DOI: 10.1088/0964-1726/24/2/025034. [Online]. Available: https://dx.doi.org/10.1088/0964-1726/24/2/025034.

[18] L. Wang, Y. Yang, Y. Chen, *et al.*, "Controllable and reversible tuning of material rigidity for robot applications," *Materials Today*, vol. 21, no. 5, pp. 563–576, 2018, ISSN: 1369-7021. DOI: https://doi.org/10.1016/j.mattod.2017.10.010.

[19] Z. Wang, P. Song, F. Isvoranu, and M. Pauly, "Design and structural optimization of topological interlocking assemblies," *ACM Transactions on Graphics*, vol. 38, p. 193, 2019. DOI: 10.1145/3355089.3356489.

[20] A. V. Dyskin, Y. Estrin, A. J. Kanel-Belov, and E. Pasternak, "Topological interlocking of platonic solids: A way to new materials and structures," *Philosophical Magazine Letters*, vol. 83, no. 3, pp. 197–203, 2003. DOI: 10.1080/0950083031000065226.

[21] M. Weizmann, O. Amir, and Y. J. Grobman, "Topological interlocking in buildings: A case for the design and construction of floors," *Automation in Construction*, vol. 72, pp. 18–25, 2016, Computational and generative design for digital fabrication: Computer-Aided Architectural Design Research in Asia (CAADRIA), ISSN: 0926-5805. DOI: https://doi.org/10.1016/j.autcon.2016.05.014.

[22] R. Kawamoto, E. Andò, G. Viggiani, and J. E. Andrade, "Level set discrete element method for three-dimensional computations with triaxial case study," *Journal of the Mechanics and Physics of Solids*, vol. 91, pp. 1–13, 2016, ISSN: 0022-5096. DOI: https://doi.org/10.1016/j.jmps.2016.02.021.

[23] R. B. de Macedo, E. Andò, S. Joy, *et al.*, "Unearthing real-time 3d ant tunneling mechanics," *Proceedings of the National Academy of Sciences*, vol. 118, no. 36, 2021. DOI: 10.1073/pnas.2102267118.

[24] J. M. Harmon, V. Gabuchian, A. J. Rosakis, *et al.*, "Predicting the seismic behavior of multiblock tower structures using the level set discrete element method," *Earthquake Engineering & Structural Dynamics*, vol. 52, no. 9, pp. 2577–2596, 2023. DOI: https://doi.org/10.1002/eqe.3883.

[25] Z. Zhou, M. Andreini, L. Sironi, *et al.*, "Discrete structural systems modeling: Benchmarking of LS-DEM and LMGC90 with seismic experiments," *Journal of Engineering Mechanics*, vol. 149, no. 12, p. 04 023 097, 2023.

[26] S. Feldfogel, K. Karapiperis, J. Andrade, and D. S. Kammer, "Failure of topologically interlocked structures — a level-set-dem approach," *European Journal of Mechanics - A/Solids*, vol. 103, p. 105 156, 2024, ISSN: 0997-7538. DOI: https://doi.org/10.1016/j.euromechsol.2023.105156.

[27] S. Feldfogel, K. Karapiperis, J. Andrade, and D. S. Kammer, "Scaling, saturation, and upper bounds in the failure of topologically interlocked structures," *International Journal of Solids and Structures*, vol. 269, p. 112 228, 2023, ISSN: 0020-7683. DOI: https://doi.org/10.1016/j.ijsolstr.2023.112228.

[28] S. Ullmann, D. S. Kammer, and S. Feldfogel, "The Deflection Limit of Slab-Like Topologically Interlocked Structures," *Journal of Applied Mechanics*, vol. 91, no. 2, p. 021 004, Oct. 2023, ISSN: 0021-8936.

[29] A. S. Dalaq and F. Barthelat, "Manipulating the geometry of architectured beams for maximum toughness and strength," *Materials Design*, vol. 194, p. 108 889, 2020, ISSN: 0264-1275.

[30] T. Chen, X. Yang, and Y. Wang, "Design and modeling of a programmable morphing structure with variable stiffness capability," *International Journal of Mechanical Sciences*, vol. 284, p. 109 699, Dec. 15, 2024, ISSN: 0020-7403. DOI: 10.1016/j.ijmecsci.2024.109699. [Online]. Available: https://www.sciencedirect.com/science/article/pii/S0020740324007409.

Chapter 3

A STRUCTURED FABRIC DESIGN FOR FOLDING AND DEPLOYING 3D SURFACES

T. Lu, P. Bordeenithikasem, C. McMahan, R. T. Watkins, and C. Daraio, "A structured fabric design for folding and deploying 3D surfaces," American Society of Mechanical Engineers Journal of Mechanisms and Robotics (in review).

3.1 Introduction

Self-transforming structures have inspired researchers across disciplines to develop novel materials, fabrication techniques, and programmable properties. Designing such deployable structures is a computational challenge that requires physically realizable configurations that meet functional constraints while managing numerous degrees of freedom. In addition, the ability to fold deployable 3D solid surfaces without relying on rigid mechanisms and hinges allows for tight compaction, making it particularly useful for applications such as soft robotics [1], kinetic architectures [2], solar panels [3], or antenna deployment [4]. For example, current deployable antennas are typically restricted to lower frequency bands because their rigid mechanisms are only compatible with mesh surfaces, rather than solid surfaces [5]. Mesh reflectors do not readily scale above Ka-bands (27-40 GHz) due to mesh leakage and surface tolerance issues. Other antennaes such as Reflectarrays have very narrow bandwidth and will require stiffening structures to maintain surface tolerances to extend to above Ka-band. [6]. There is also ongoing work on trusses for foldable W-band (higher frequency of 75 to 110 GHz) antennas but the complexity of the truss having to open in one attempt to acheive a desirable surface is limiting [7]. A self-transforming structure with fabric-like qualities that can fold while remaining structurally stable would be beneficial for designing future deployable antennas with solid surfaces, enabling them to achieve higher frequencies beyond the constraints of current mesh designs [8]–[10].

In this study, we create deployable structures that are compacted by folding along prescribed fold patterns and morph into desired 3D shapes upon the release of a flattening or folding force. The structures achieve stability by leveraging conformal mapping and the compressive contact properties of the structured fabric design, while accommodating fold patterns that can remain independent of the target 3D

surface, allowing stowage of the same structure into different shape containers. Our prototypes highlight how the design and fabrication methods can be extended to other shapes and fold patterns of interest.

The ability of structured fabrics to alternate between stiff and flexible states makes them advantageous for deployable applications, offering benefits such as compact stowage, on-demand structural integrity, versatility, and weight efficiency [11]. This capability has been demonstrated in woven topologically interlocking materials [12], [13], which utilize 3D printed blocks interwoven with various wires, including nylon, carbon fiber, and Shape Memory Alloy [14], [15], as well as in woven active fabrics [16]. These approaches have been useful for applications starting from planar and flat configurations, but are less suitable for foldable structures and assemblies that require tension from multiple directions for stability and deployment. Wires tend to tangle or overlap and do not tension uniformly when folded multiple times (Appendix 2).

These challenges can be overcome by using pre-stretched elastic sheets that behave as uniform, multidirectional transformation mechanisms. This approach was demonstrated by Guseinov et al. [17], where flat initial configurations of disconnected rigid tiles are first sandwiched between two elastic sheets, then collide and jam into desired 3D shapes when the pre-stretch is released. Other studies have shown shape morphing driven by pre-stretched elastic sheets using non-periodic tessellations of contractile unit cells that soften in water to form the new shape [18]. Similarly, we design systems that sandwich a pre-stretched elastic sheet between tiles of different shapes, which collide when the stretch is released to form curved structures with a continuous surface [18]. However, we also select the tiles' geometry to enable predetermined folding patterns for stowage.

The freedom to fold structures along desired creases enables achieving target compaction volumes or shapes. While studies on origami of non-zero thickness materials [19]–[21] provide guidelines for folding deployable surfaces, most origami fold patterns are based on a flat surface orientation. Because we seek to fold curved 3D surfaces, we require the additional steps of conformally mapping a deployed geometry's mid-surfaces to a flat mesh, then overlaying the 2D fold pattern. This guarantees both the foldability of the structure and that the extruded tiles will collide in a manner that induces deployment into pre-programmed 3D surfaces.

Overview

We explore a method of compacting and deploying tile-based assemblies into stable 3D configurations without rigid mechanisms or manual assembly. There is freedom in the assignment of crease patterns to the structure so they can be folded to achieve desired compact storage geometries. Our assembly, which we call a structured fabric, is composed of flat, rigid tiles that sandwich a solid active surface (an elastic sheet that stores the energy required to drive the morphing process). Starting from a flat initial configuration, the fabric achieves compaction via folding and an approximation of a desired three-dimensional shape upon releasing its binding mechanism, the elastic sheet. In addition, the elastic sheet is essential for reaching non-zero Gaussian curvatures from initially flat shells, where bending must be coupled to in-plane stretches, according to Gauss' Theorema Egregium [22].

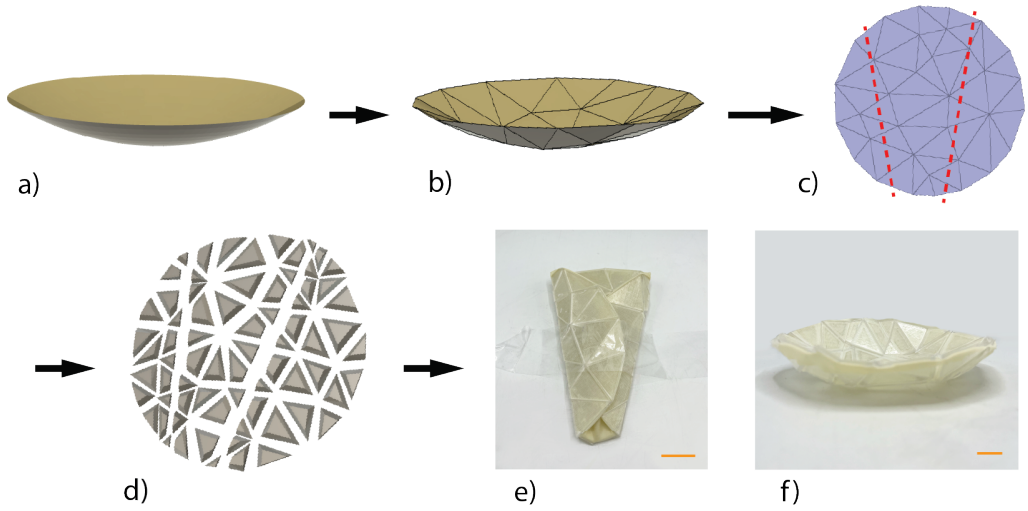

Figure 3.1: Overview of our workflow using an example of a paraboloid surface: the input design (a) is decimated to a coarser triangular mesh (b). After conformal flattening, a fold pattern is overlaid on the flattened mesh and the intersected triangles are split into derivative polygons (c). Each mesh element is separated via an isotropic rigid body translation and extruded on each side so that they will yield the dihedral angles of the target surface mesh (d). The fabricated structured fabric result is shown being folded along the crease pattern in (f), and after deployment in (e). Scale bars, 3cm.

Algorithm 1 summarizes the computational design approach of the structured fabrics. The distribution of tiles it creates accounts for the fold lines and enables achieving a targeted 3D surface upon actuation. When the pre-tensioned elastic

Algorithm 1: Summary of Algorithm

```
Mesh:=decimated mesh
Data: Mesh.vertices, Mesh.face, Mesh.face.neighbors, Mesh.face.normal
Function FlattenMesh(Mesh)
    Conformally flatten the decimated mesh such that Eq. 1 is satisfied
    return FlatMesh.vertices, FlatMesh.faces
Function CutFoldLines(lineSegments, FlatMesh.vertices, FlatMesh.faces)
    foreach line in lineSegments do
        foreach face in FlatMesh do
            if line crosses at least 1 face.edge then
                newVertices:= FindIntersect(line,face.edge)
                Find Case:
                A: 1 vertex and 1 edge are crossed, with internal point
                B: 2 edges are crossed, with internal point
                C: 2 vertices are crossed, with internal point
                D: 1 vertex and 1 edge are crossed
                E: 1 vertex and 1 edge are crossed
                based on the identified case, store new mesh vertices and faces
            else
    return CutMesh.vertices, CutMesh.faces
Function ExtrudeTiles(CutMesh.vertices, CutMesh.faces, thickness)
    solve Eq.3
    return BottomVertices
Function Spacing(CutMesh.vertices, CutMesh.faces, BottomVertices)
    spread out the tiles such that the extruded tiles do not intersect
    return FinalMesh.vertices,FinalBottomVertices
Result: script of coordinates of each tile as OpenScad Polyhedron
```

sheet is released, contractile forces cause the tiles to collide at prescribed dihedral angles, generating local curvatures that control the structure's global shape. The prestretched elastic sheet applies uniform contraction forces to jam the pieces together. This actuation method was selected over the tensioned wires used in the previous chapter, because the wires produced only uniaxial forces, and weaving them to achieve uniformity across the area proved impractical. The antenna-resembling paraboloid shown in Fig. 3.1 demonstrates the application of the algorithm. The first step is to input a 3D model for the target surface (Fig. 3.1a) and a crease pattern along which the paraboloid is folded (Fig. 3.1b). The 3D description of the target surface is meshed and reduced (Fig. 3.1c) so that there are fewer triangular faces, resulting in lower fabrication complexity as each triangle in the resulting mesh will become a tile. Next, the simplified mesh is conformally flattened with a bijective mapping of the 3D to 2D mesh, (Fig. 3.1d) and faces that intersect the crease pattern

are split to accommodate the fold pattern. To generate the extruded tile geometries, the polygonal mesh faces are spread isotropically and extruded to display the dihedral angles required by the deployed geometry (Fig. 3.1d). The tiles are then split along their mid-plane into top and bottom halves. The fabricated tiles are then glued to both sides of a pre-stretched elastic sheet in their pre-determined locations and orientations. Upon releasing the pre-stretch, the sheet contracts to form the targeted 3D structure (Fig. 3.1f), but it can be folded along the fold pattern shown in (Fig. 3.1e)., or crumpled like a fabric (Fig. 3.2).

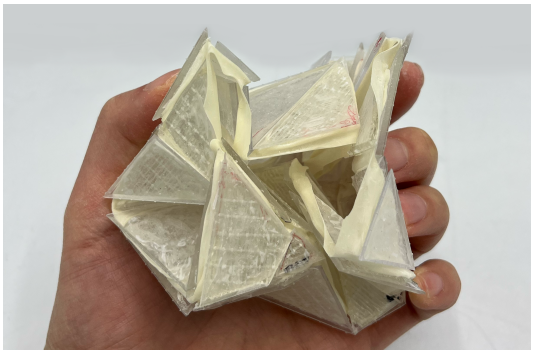

Figure 3.2: Demonstrating the flexibility of a structured fabric that deploys into a paraboloid.

While the original inspiration of the designs was an antennae so parabolic target shapes were chosen, other target surfaces of different curvatures were explored as well. The other shapes were chosen to demonstrate a diversity of the Gaussian curvatures, as defined below [23].

In terms of curves traveling along the surface, let X be a unit tangent direction at some distinguished point on the surface, and consider a plane containing both $df(X)$ and the corresponding normal N. This plane intersects the surface in a curve, and the curvature κ_n of this curve is called the normal curvature in the direction X.

The normal curvature along X by extracting the tangential part of dN:

$$\kappa_n(X) = \frac{df(X) \cdot dN(X)}{|df(X)|^2} \tag{3.1}$$

where the factor $|df(X)|^2$ normalizes any stretching that occurs as we map from the 2D domain into the 3D domain [24].

At any given point the directions that the surface bends the most along can be found. The principal directions are the unit vectors X_1 and X_2 along which we find

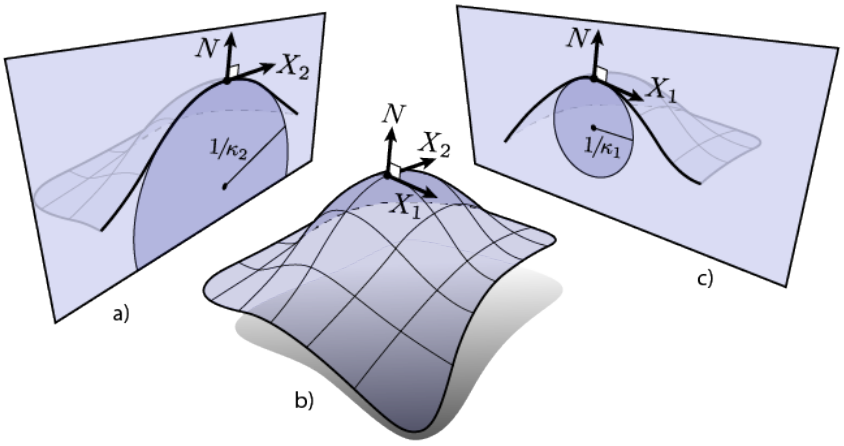

Figure 3.3: X_1 and X_2 are the unit vectors along which the maximum and minimum normal curvatures κ_1 and κ_2 are found [23]; (a) The visual representation of X_2 with its corresponding normal vector N and κ_2; (b) The location of where the vectors are relative to the entire surface; (c) The visual representation of X_1 and its corresponding normal vector N.

the maximum and minimum normal curvatures κ_1 and κ_2. The curvatures κ_i are called the principal curvatures. The Gaussian curvature is an intrinsic measure of curvature, independent of the coordinate system used to describe it, representing an average of the two principal curvatures [23]:

$$K = \kappa_1 \kappa_2. \tag{3.2}$$

Surfaces with zero Gaussian curvature are called developable surfaces because they can be flattened out into the plane without any stretching or tearing. For instance in Fig. 3.4a, any piece of a cylinder is developable since one of the principal curvatures is zero. Designs of this target geometry can be achieved with angled collisions between tiles aligned in the direction of non-zero principal curvature. An example of a surface with positive curvature is Fig. 3.4b, where the principal curvatures are in the same direction and therefore have the same sign. Surfaces with zero mean curvature are called minimal surfaces because they minimize surface area (with respect to certain constraints). Minimal surfaces tend to be saddle-like since principal curvatures have equal magnitude but opposite sign, as shown in Fig. 3.4c.

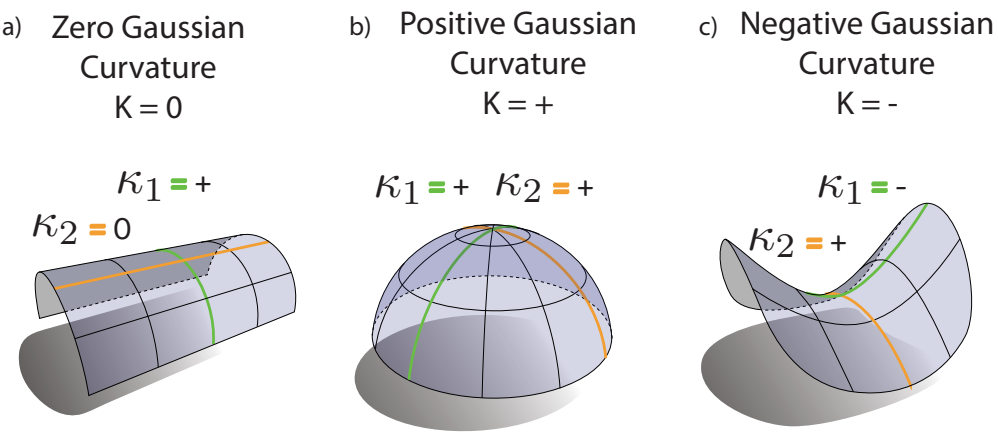

Figure 3.4: Surfaces with different Gaussian Curvatures [25]: (a) Zero Gaussian Curvature. (b) Positive Gaussian Curvature. (c) Negative Gaussian Curvature.

3.2 3D Model Generation

Mesh Flattening

The first input to our design algorithm is a triangular mesh that describes the structure's target 3D shape. Because a physical tile will be associated with each triangular mesh element, this target surface mesh is decimated to minimize fabrication complexities. Triangular meshes reduce the number of edge contacts per tile relative to other polygonal meshes, but our design approach could be readily applied to other mesh topologies. Because fabrication and assembly occur on a flat 2D surface, the 3D surface must be mapped to a planar configuration. Conformal flattening [26] achieves this while minimizing shearing, which can introduce tile edge misalignment and shape inaccuracies during the elastic sheet's contraction.

Conformal maps are functions that preserve the angles between curves [27]. More precisely, suppose $X(z)$ is differentiable at $z_0 = (u, v)$ and $\gamma(t)$ is a smooth curve through z_0 and $\gamma(t_0) = z_0$. The function maps the point z_0 to $w_0 = f(z_0)$ and the curve γ to

$$\tilde{\gamma}(t) = X(\gamma(t)).$$

Under this map, the tangent vector $\gamma'(t_0)$ at z_0 is mapped to the tangent vector

$$\tilde{\gamma}'(t_0) = (X \circ \gamma)'(t_0)$$

at w_0. Using the notations above, the definition is as follows: The function $X(z)$ is conformal at z_0 if there is an angle ϕ and a scale $a > 0$ such that for any smooth curve $\gamma(t)$ through z_0 the map X rotates the tangent vector at z_0 by ϕ and scales it

by a. That is, for any γ, the tangent vector $(X \circ \gamma)'(t_0)$ is found by rotating $\gamma'(t_0)$ by ϕ and scaling it by a. If $X(z)$ is defined on a region A, it is a conformal map on A if it is conformal at each point z in A. In addition, the scale factor a and rotation angle ϕ depends on the point z, but not on any of the curves through z [28].

A visual representation is shown in (Fig. 3.5a), where the local angles of the mesh are preserved such that N(u,v) is the cross product of du and dv and

$$N(u,v) \times \frac{dX}{du}(u,v) = \frac{dX}{dv}(u,v). \tag{3.3}$$

Prescribing the boundary geometry of the flattened mesh ensures compatibility with the desired folding patterns that are needed to attain the target compacted configuration. This motivates performing conformal flattening using The Boundary First Flattening (BFF) tool, as described in Sawhney et. al [26]. This tool not only minimizes distortion during the initial flattening but also allows for the introduction of cone singularities, which can dramatically reduce area distortion. Furthermore, BFF enables boundary adjustments of the flattened domain, allowing the fold pattern to better overlay the tiled design and minimize mesh element splitting. We discuss folding in the next subsection.

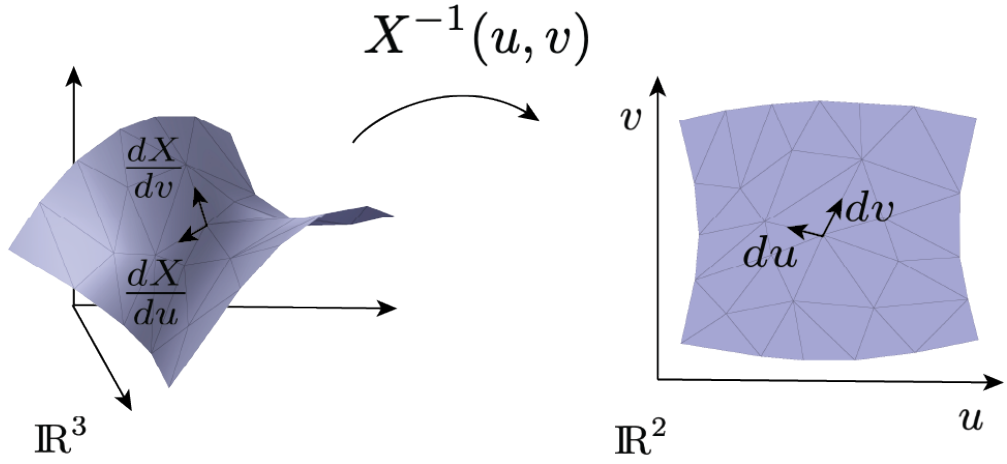

Figure 3.5: Local angles are preserved during mesh flattening.

Fold Pattern Overlay

One of the features of this fabric structuring approach is that it enables folding along predetermined lines to achieve a desired compaction shape and size. Since the rigid tiles are compressed into contact by the elastic sheet, the structure can only be folded along tile boundaries. Therefore, mesh elements that intersect an overlay

of the desired crease pattern mesh must be split to enable the required local bending mode. This is shown in Fig. 3.6.

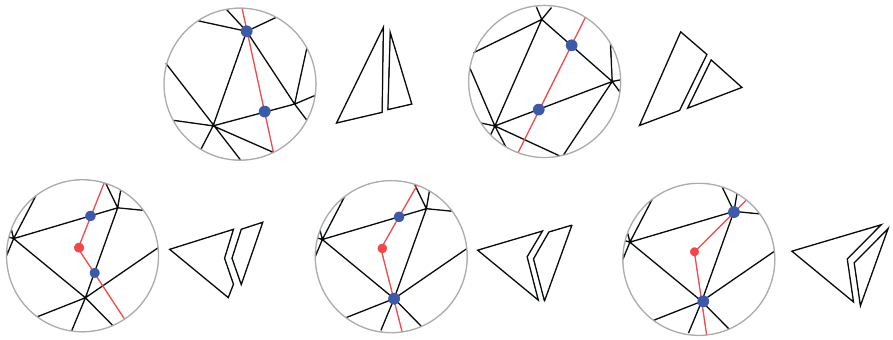

Figure 3.6: Examples of tile cuts required by fold patterns overlaid on the flattened mesh.

The fold lines are defined by their endpoint coordinates. The mesh-splitting algorithm first determines which triangular facet contains each endpoint. An endpoint is contained within a facet if all components of its barycentric coordinates are non-negative. Starting from one endpoint of the fold line segment and progressing toward the other, the algorithm determines the location where it intersects the triangle boundary and determines the next mesh facet that will contain a line segment. Finally, mesh elements are divided along lines connecting the intersection points. This process is repeated for each fold line.

Tile Extrusion

The edges of the initially planar tiles should collide at the dihedral angles required to form the desired global 3D shape. Therefore, the 2D triangles derived from the flattened mesh should not be extruded perpendicularly into prisms but rather at specified frustrum angles. This is illustrated in Fig. 3.7. The extrusion angle for each edge is determined by finding the half-angle between the normal vectors of adjacent faces. The facet edges are then projected to a parallel plane at a distance t (the prescribed tile thickness) while enforcing the calculated dihedral angles.

We also evaluate the normal vectors of two adjacent tiles to determine whether these vectors converge or diverge based on the sign of the estimated local curvature: positive curvature indicates they point towards each other, while negative curvature indicates they point away from each other.

$$(\vec{n_2} - \vec{n_1}) \cdot \frac{v_2 - v_1}{\|v_2 - v_1\|^2} \tag{3.4}$$

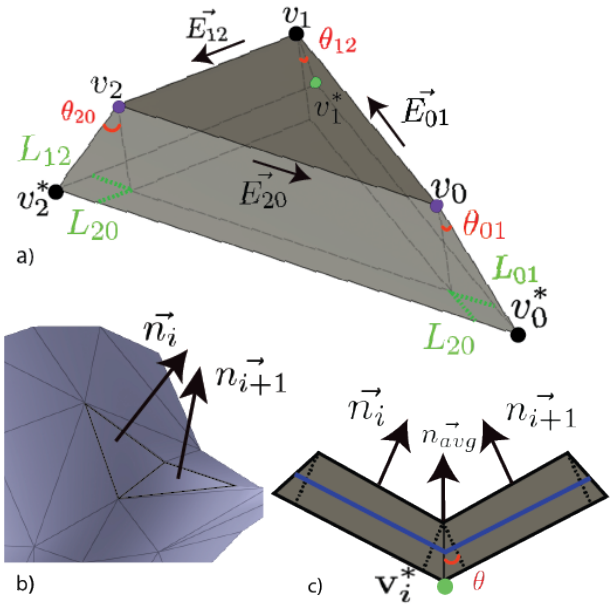

Figure 3.7: (a) A diagram with notation labeling a tile where E_{ab} is the edge vector from vertex a to vertex b, θ_{ab} is the half-angle between the normal vectors of the current face and adjacent face for the tile edge of E_{ab}, L_{ab} is the projected distance perpendicular to E_{ab} that is extended from the original vertex. (b) Two neighboring faces and their normal vectors on the reduced input mesh, (c) a side view of how the tiles collide when the structure is deployed. The blue line indicates where they are split to adhere to the membrane.

If Eq. 3.4 is positive, the tiles should form a concave shape and the tile is extruded to be progressively wider away from its extrusion plane. If Eq. 3.4 is negative, the tiles should form convex shape and the angle extrudes the tile in the opposite direction.

The coordinates of the tile vertices on the projection plane are given by:

$$\begin{aligned} v_0^* &= v_0 - (L_{20} \cdot \vec{E_{01}}) + (L_{01} \cdot \vec{E_{20}}) + \vec{t} \\ v_1^* &= v_1 + (L_{12} \cdot \vec{E_{01}}) - (L_{01} \cdot \vec{E_{12}}) + \vec{t} \\ v_2^* &= v_2 + (L_{20} \cdot \vec{E_{12}}) - (L_{12} \cdot \vec{E_{20}}) + \vec{t} \end{aligned} \tag{3.5}$$

where L_{ab} is the projected distance perpendicular to E_{ab} that is extended from the original vertex, and E_{ab} is the edge vector from vertex a to vertex b, and a and b are 0, 1, or 2.

$$\begin{aligned} \vec{t} &= \begin{bmatrix} 0 & 0 & t \end{bmatrix} \\ L_{01} &= t \cdot \tan(\theta_{01}) \\ L_{12} &= t \cdot \tan(\theta_{12}) \\ L_{20} &= t \cdot \tan(\theta_{20}) \end{aligned} \tag{3.6}$$

The tiles are then split along their mid-thickness plane into top and bottom halves which will sandwich the elastic membrane.

Spacing

The tiles are assumed to be rigid and in the algorithm are spaced apart to prevent overlap following the angled extrusions described in the previous section. The elastic membrane will need to be pre-stretched sufficiently to drive tile collisions, but the chosen stretch should not be greater than what is minimally needed. This minimizes the stress the elastic membrane is subjected to and eases fabrication. The spacing is done by scaling the centroids of faces about the structure's center of mass in the flat configuration, then translating each tile to its new centroid via rigid body motion. The residual stresses present in the elastic membrane after tiles collide stiffen the deployed configuration of the structure. Then the pre-stretch applied to the elastic membrane during fabrication is based on the stretch factor chosen in the algorithm during triangle spacing, which is discussed in the next section.

3.3 Fabrication

After generating the STL files for the top (Fig. 3.8a) and bottom halves (Fig. 3.8b) of the tiles, the tiles were manufactured using Stereolithography 3D printing on a 3D Systems SLA ProJet7000 machine with Accura ClearVue, a polycarbonate-like plastic. The tiles were printed attached to a plate with support structures to maintain their predetermined positions and orientations relative to neighboring tiles. The plate and support material were only removed after adhering the tiles to the pre-stretched sheet, to ensure the positions and orientations were preserved during fabrication.

To adhere the tiles to the stretched elastic sheet, double-sided tape was cut with a Cricut Explore Air into shapes corresponding to the cross-section of the tiles at their mid-thickness plane. The corresponding cross-sectional shapes were reduced to 75% of their area to allow the elastic sheet additional contraction room, ensuring that the tiles would jam together. Each double-sided tape piece was then adhered to

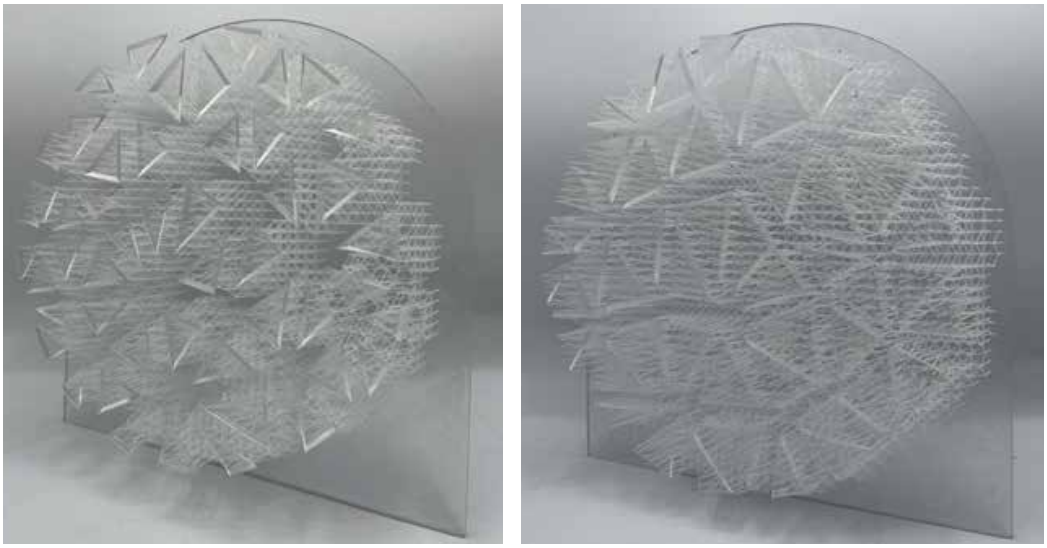

Figure 3.8: Paraboloid with two fold lines. (a) Left: The 3D-printed top halves of the tiles. (b) Right: The 3D-printed bottom halves of the tiles.

the respective tile for both the top and bottom halves.

To achieve uniform stretching of the rubber sheets, we utilize a stretching frame with evenly spaced teeth that provide sufficient friction to maintain the sheet's tension without additional fixation [17]. To attain the desired equiaxial stretching factor, we place markers on the sheet and manually stretch it until the markers are coincident with the tooth tips on the stretching device. The elastic sheet was stretched to the factor used in the generation code which finds the minimum to avoid tile overlap from the angled extrusion, with an additional 0.3x stretch to account for stress relaxation during fabrication. The elastic sheet, a 0.008" 40A Rubber Sheet was cleaned to remove residual particles and dust before adhering the tiles to each side. The second layer was then aligned to match the tiles on the other side and adhered to the elastic sheet with the same method as the previous layer of tiles.

The plate with its attached support material was removed from both the top and bottom halves, using a Dremel tool with a cutting wheel (Fig. 3.9b). The result of the removal is shown in Fig. 3.9c while the assembly remains stretched. Finally, the fabricated assembly was unhooked from the stretching frame, allowing the tiles to jam into the target 3D shape in Fig. 3.9d. The dimensionality of the shape is more clearly shown outside of its fabrication environment in Fig. 3.1f. The structure can then be folded along the fold lines and bound to maintain the folded shape. When there are no forces holding the folds in place or stretching the sheet, the structured

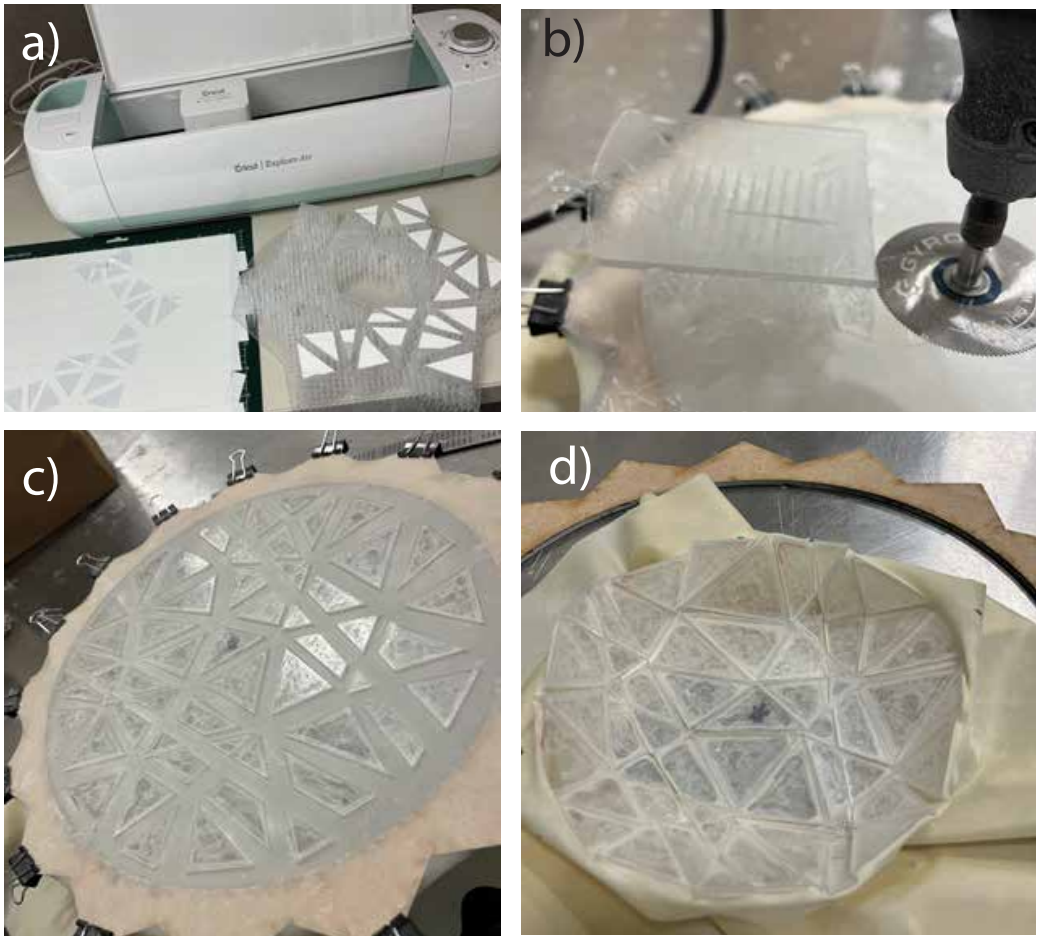

Figure 3.9: (a) Precision-cut, double-sided tape is adhered to each tile. (b) The support structure is removed and a plate holds the positions and orientations of the the tiles after adhesion to the elastic sheet. (c) The top and bottom halves after adhesion and removal from the support. (d) Releasing the sheet from the stretching frame.

fabric pops into its target 3D shape.

The fabrication process could be enhanced by aligning the placement of the stickers to the centroids of each tile, using an image projection of the isotropically reduced area of the original tile for precise positioning. Additionally, the removal of support structures could be further refined using an abrasive blast chamber to achieve smoother results. While there is a clear, but more labor-intensive, pathway to improve repeatability, the primary goal of this work was to demonstrate the feasibility of the process.

3.4 Results

The results present deployable structures that fold along set patterns for compact storage and transform into desired 3D shapes when released. Stability is achieved through conformal mapping and the compressive properties of the structured fabric, allowing fold patterns to remain independent of the target 3D surface. The prototypes show how these design and fabrication methods can be applied to different shapes and fold patterns. While the fabric can be randomly collapsed (Fig. 3.2), applications requiring control over the sequence of unfolding or the compacted configuration would benefit from the ability to fold along predefined lines. Furthermore, the randomness inherent in crumpling may introduce unintended folds, potentially leading to damage, such as an edge of a tile inadvertently tearing the membrane due to improper alignment during folding.

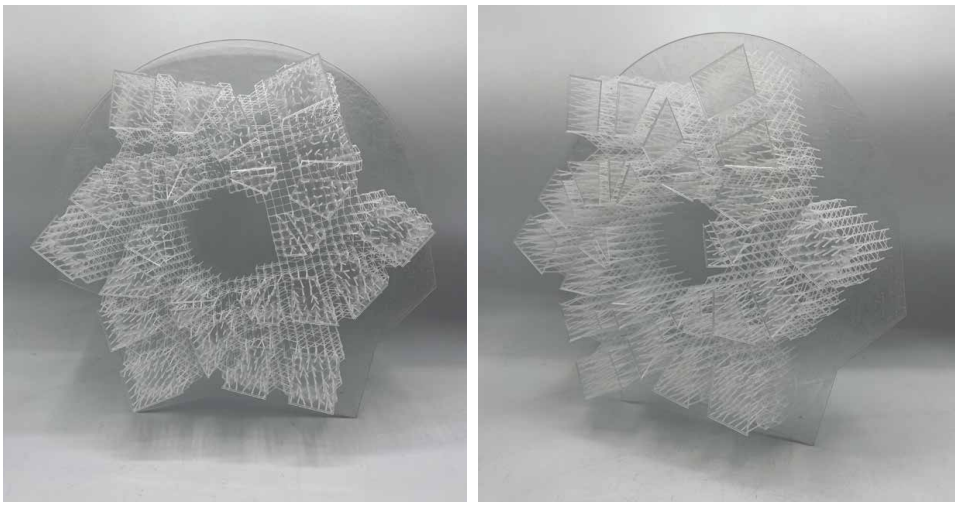

Figure 3.10: Paraboloid with flasher fold pattern. (a) Left: the 3D-printed top halves of the tiles; (b) Right: the 3D-printed bottom halves of the tiles.

In Figs. 3.11-3.13, the pictures from top left to top right to bottom left to bottom right display the target surfaces, overlaid fold patterns, deployed fabricated structured fabrics, and folded structured fabrics. In the Fig. 3.11, a paraboloid target surface was selected, based on our antennae application inspiration. It can be folded into a cylindrical shape via an origami flasher fold pattern [29], which has been used in other deployable space structures [30]. Traditionally, origami flashers are used on flat round panels [31]; however, we overlaid the flasher pattern onto the paraboloid 3D surface using the methods we have described. A zip tie holds the structure in place to prevent natural deployment into its 3D shape. Upon cutting the zip tie, the structured fabric unfolds into the discretized approximation of the target surface.

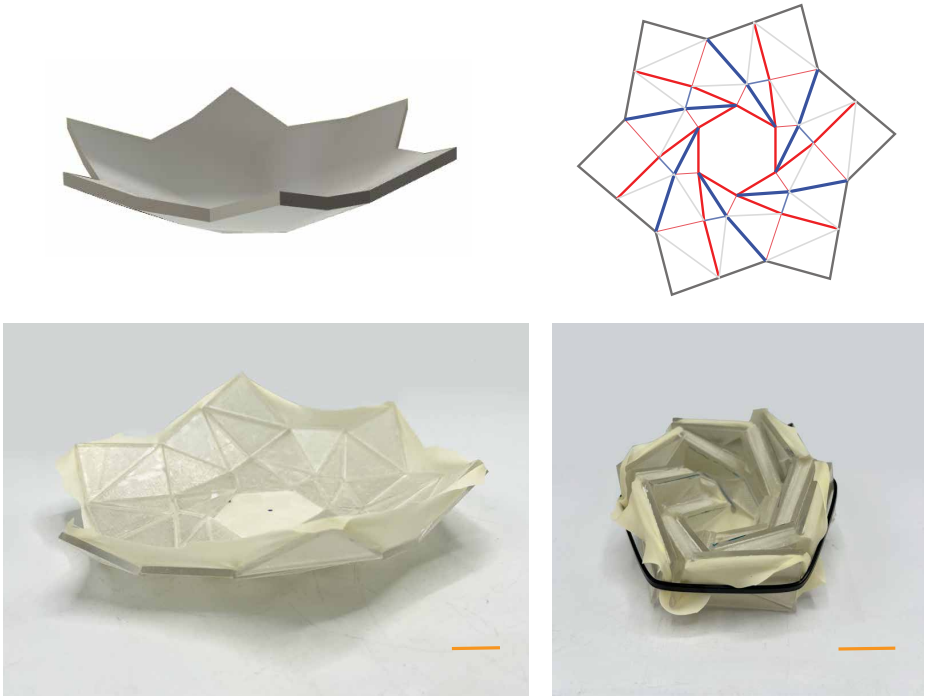

Figure 3.11: Paraboloid with an origami flasher fold pattern. For each section: (a) top left: input design, (b) top right: overlaid fold pattern, (c) bottom left: actuated deployed configuration, (d) bottom right: folded configuration. The valley folds are indicated with red, mountain folds are indicated with blue, supplementary bends are indicated with gray. Scale bar, 3cm.

The compaction ratio of the structured fabric was approximately 2:1 by volumetric shrinkage of an enclosing box. We also show the deployment and packing of a saddle in Fig. 3.12, highlighting that our method can be used for structures that display both positive and negative principal curvatures. The selected fold pattern was a simple quadrant fold, compacting the shape into a prism-like form. The compaction ratio of the structured fabric was approximately 3:1 by volumetric shrinkage of an enclosing box. The final example (Fig. 3.13) showcases the flexibility of compacted geometries that can be achieved with our approach to stowage and deployment: we demonstrate a structured fabric that deploys into a shape inspired by the Lilium Tower and can be folded into a paper airplane configuration. To reduce the additional area distortion due to the sharper curvature around the corners, cone singularity points were placed on corners during mesh flattening.

To determine deployment shape-accuracy, a Zeiss Comet L3D-5MP3D Scanner was used to scan a physical prototype of the saddle and generate a textured 3D mesh

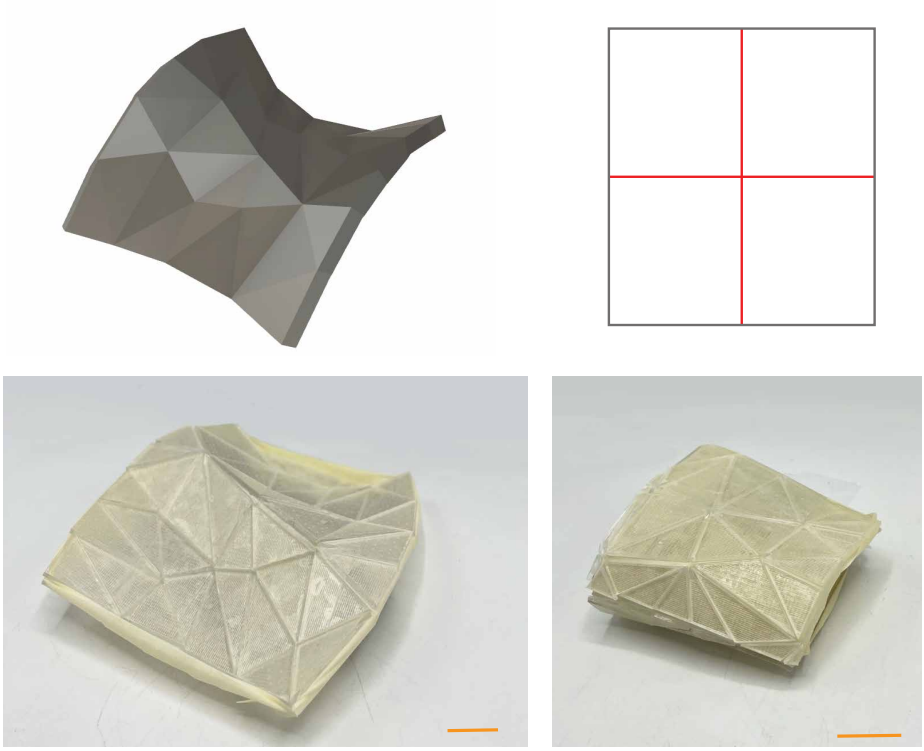

Figure 3.12: Saddle with a quadrant fold pattern. For each section: (a) top left: input design, (b) top right: overlaid fold pattern, (c) bottom left: actuated deployed configuration, (d) bottom right: folded configuration. The valley folds are indicated with red, mountain folds are indicated with blue, supplementary bends are indicated with gray. Scale bar, 3cm.

in STL format. Then the scanned mesh was compared to the actual mesh using the 3D Systems Geomagic software. As shown in Fig. 3.14, the 3D scan and analysis reveals a maximum deviation of the physical model from the target surface is 5.1% of the bounding box diagonal with a max deviation of about 4.1mm. The overall shape is a good approximation of the target 3D surface, however due to unavoidable inconsistencies in the fabrication process, mesh coarseness, and area distortion during the conformal flattening, there is more surface deviation in sections of the structure that display large curvature.

The structure is currently limited to a single deployed shape, capable of achieving either positive or negative Gaussian curvature. However, more complex geometries and reduced deviation error could be achieved by reducing the size of the tiles and increasing the dimensions of the overall structure. As illustrated in the crumpled versus folded example, the structures can adopt different compacted configurations,

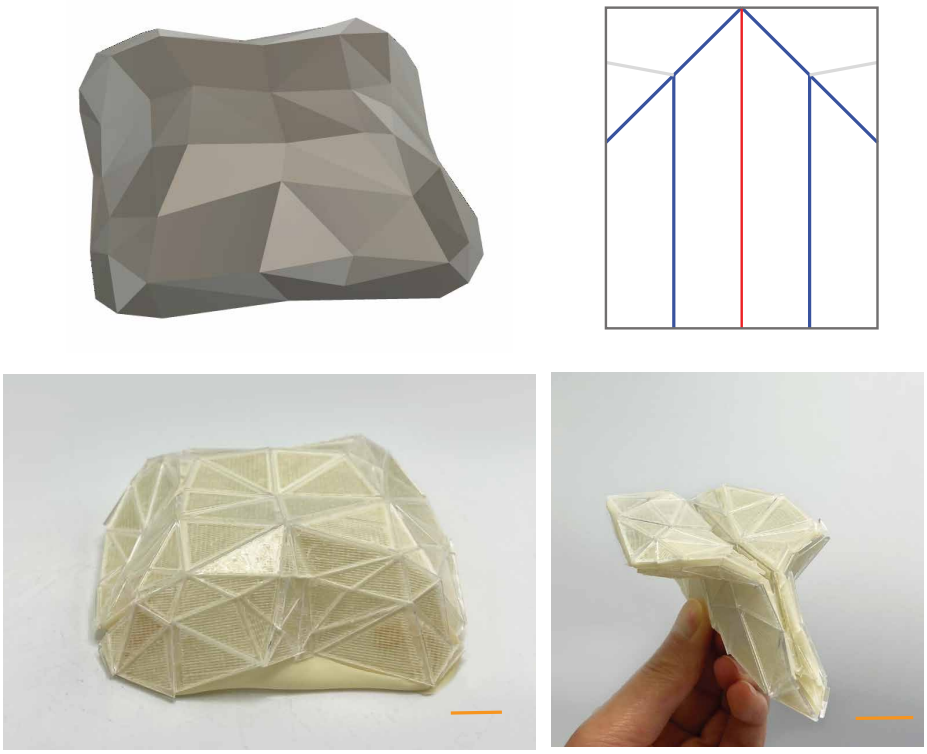

Figure 3.13: Lilium with a paper airplane fold pattern. For each section: (a) top left: input design, (b) top right: overlaid fold pattern, (c) bottom left: actuated deployed configuration, (d) bottom right: folded configuration. The valley folds are indicated with red, mountain folds are indicated with blue, supplementary bends are indicated with gray. Scale bar, 3cm.

particularly if multiple fold line options are incorporated into the tile pattern. While the fabrication could be improved with more resources and labor, the acceptable deviation depends on usage of the designs for deployables and other soft robotics.

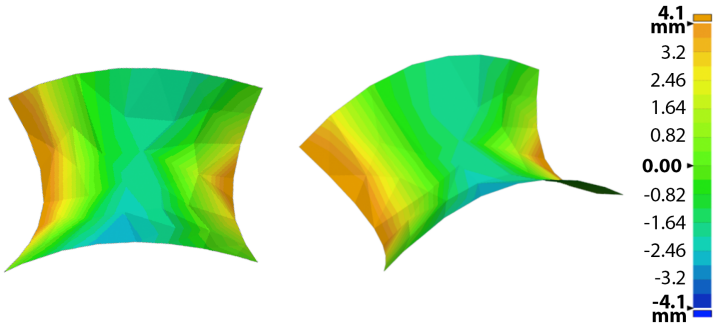

Figure 3.14: A 3D scanned comparison of the saddle model with error.

3.5 Conclusion

This computational design methodology uniquely combines the compressive contact characteristics of the structured fabric, boundary-first conformal mapping, and folding of thick materials to enable deployment and compaction of 3D surfaces. The resulting 3D surfaces become load-bearing structures, warranting further investigation into their load capacity. As with other morphing structure approaches that leverage conformal mappings, our methods are less effective for surfaces with regions of large curvature. In these cases, the surface accuracy declines as a result of area distortion from conformal mapping. To improve deployment accuracy and stability, connectors or 3D printed micro-velcro [32] could be added to the edges of the tiles so they lock together upon contact. Other ways of actuating the tiles besides elastic sheets should also be explored, such as with shape memory alloy or other actuators that provide equiaxial forces. Additionally, incorporating curved tiles instead of flat ones could enable the formation of more complex geometries, though this would introduce tiles with variable thickness and added complexities to the design process.

The maturation of this method for structured fabric design would benefit from future efforts that incorporate analyses into the effects of fold patterns on elastic sheet strain energy, and from methods to optimize fold patterns. This would enable achieving improved compaction ratios while minimizing strain energy, thereby reducing unnecessary stretching and potential for sheet degradation.

3.6 Acknowledgments

I would like to thank Manan Arya for valuable discussions and for providing the crease pattern for the structure shown in Figure 7a, Hector Ramirez and Mauricio Zuleta for 3D printing support and fabrication, Wenjie Zhou for helping create input models, and all proofreaders and anonymous reviewers. Part of this research was done at the Jet Propulsion Laboratory (JPL), California Institute of Technology, under contract with NASA (80NM0018D0004). This work was supported by the JPL Researchers on Campus program and Caltech President's and JPL Director's Research and Development Fund. Reference herein to any specific commercial product, process, or service by trade name, trademark, manufacturer, or otherwise, does not constitute or imply its endorsement by the United States Government or the Jet Propulsion Laboratory, California Institute of Technology.

3.7 Bibliography

References

[1] X. Yang, Z. Wang, B. Zhang, *et al.*, "Self-sensing robotic structures from architectured particle assemblies," *Advanced Intelligent Systems*, vol. 5, no. 1, p. 2 200 250, 2023. DOI: https://doi.org/10.1002/aisy.202200250.

[2] T. Tachi, "Rigid-foldable thick origami," *Origami 5*, pp. 253–264, 2011.

[3] T. Chen, O. R. Bilal, R. Lang, C. Daraio, and K. Shea, "Autonomous deployment of a solar panel using elastic origami and distributed shape-memory-polymer actuators," *Phys. Rev. Appl.*, vol. 11, p. 064 069, 6 Jun. 2019. DOI: 10.1103/PhysRevApplied.11.064069. [Online]. Available: https://link.aps.org/doi/10.1103/PhysRevApplied.11.064069.

[4] A. Babuscia, M. Van de Loo, Q. J. Wei, S. Pan, S. Mohan, and S. Seager, "Inflatable antenna for cubesat: Fabrication, deployment and results of experimental tests," in *2014 IEEE Aerospace Conference*, 2014, pp. 1–12. DOI: 10.1109/AERO.2014.7024296.

[5] E. National Academies of Sciences and Medicine, *Thriving on Our Changing Planet: A Decadal Strategy for Earth Observation from Space*. Washington, DC: The National Academies Press, 2018, ISBN: 978-0-309-46757-5. DOI: 10.17226/24938. [Online]. Available: https://nap.nationalacademies.org/catalog/24938/thriving-on-our-changing-planet-a-decadal-strategy-for-earth.

[6] B. Imaz-Lueje, D. R. Prado, M. Arrebola, and M. R. Pino, "Reflectarray antennas: A smart solution for new generation satellite mega-constellations in space communications," *Scientific Reports*, vol. 10, no. 1, p. 21 554, 2020. DOI: 10.1038/s41598-020-78501-0.

[7] L. Dai and R. Xiao, "Optimal design and analysis of deployable antenna truss structure based on dynamic characteristics restraints," *Aerospace Science and Technology*, vol. 106, p. 106 086, Jul. 2020. DOI: 10.1016/j.ast.2020.106086.

[8] S. H. Kang and C. W. Jung, "Transparent patch antenna using metal mesh," *IEEE Transactions on Antennas and Propagation*, vol. 66, no. 4, pp. 2095–2100, 2018.

[9] P. A. R. Ade, G. Pisano, C. Tucker, and S. Weaver, "A review of metal mesh filters," in *Millimeter and Submillimeter Detectors and Instrumentation for Astronomy III*, International Society for Optics and Photonics, vol. 6275, SPIE, 2006, 62750U. DOI: 10.1117/12.673162. [Online]. Available: https://doi.org/10.1117/12.673162.

[10] K. Casey, "Electromagnetic shielding behavior of wire-mesh screens," *IEEE Transactions on Electromagnetic Compatibility*, vol. 30, no. 3, pp. 298–306, 1988. DOI: 10.1109/15.3309.

[11] X. Dang, F. Feng, P. Plucinsky, R. D. James, H. Duan, and J. Wang, "Inverse design of deployable origami structures that approximate a general surface," *International Journal of Solids and Structures*, vol. 234-235, p. 111 224, 2022, ISSN: 0020-7683. DOI: https://doi.org/10.1016/j.ijsolstr.2021.111224. [Online]. Available: https://www.sciencedirect.com/science/article/pii/S0020768321003127.

[12] T. Lu, Z. Zhou, P. Bordeenithikasem, *et al.*, "Role of friction and geometry in tuning the bending stiffness of topologically interlocking materials," *Extreme Mechanics Letters*, vol. n, pp. 7688–7694, n 2024. DOI: n.

[13] T. Siegmund, F. Barthelat, R. Cipra, E. Habtour, and J. Riddick, "Manufacture and Mechanics of Topologically Interlocked Material Assemblies," *Applied Mechanics Reviews*, vol. 68, no. 4, p. 040 803, Jul. 2016, ISSN: 0003-6900. DOI: 10.1115/1.4033967.

[14] A. Molotnikov, R. Gerbrand, O. Bouaziz, and Y. Estrin, "Sandwich panels with a core segmented into topologically interlocked elements," *Advanced Engineering Materials*, vol. 15, no. 8, pp. 728–731, 2013.

[15] A. Molotnikov, R. Gerbrand, Y. Qi, G. P. Simon, and Y. Estrin, "Design of responsive materials using topologically interlocked elements," *Smart Materials and Structures*, vol. 24, no. 2, p. 025 034, Jan. 2015. DOI: 10.1088/0964-1726/24/2/025034. [Online]. Available: https://dx.doi.org/10.1088/0964-1726/24/2/025034.

[16] X. Yang, Y. Chen, T. Chen, J. Li, and Y. Wang, "Active fabrics with controllable stiffness for robotic assistive interfaces," *Advanced Materials*, vol. n/a, no. n/a, p. 2 404 502, DOI: https://doi.org/10.1002/adma.202404502. [Online]. Available: https://onlinelibrary.wiley.com/doi/abs/10.1002/adma.202404502.

[17] R. Guseinov, E. Miguel, and B. Bickel, "Curveups: Shaping objects from flat plates with tension-actuated curvature," *ACM Trans. Graph.*, vol. 36, no. 4, Jul. 2017, ISSN: 0730-0301. DOI: 10.1145/3072959.3073709. [Online]. Available: https://doi.org/10.1145/3072959.3073709.

[18] R. Guseinov, C. McMahan, P. Jesus, C. Daraio, and B. Bickel, "Programming temporal morphing of self-actuated shells," *Nat Commun*, vol. 11, no. 1, Jan. 2020, ISSN: 0730-0301. DOI: 10.1038/s41467-019-14015-2. [Online]. Available: https://doi.org/10.1145/3072959.3073709.

[19] J. S. Ku and E. D. Demaine, "Folding Flat Crease Patterns With Thick Materials," *Journal of Mechanisms and Robotics*, vol. 8, no. 3, p. 031 003, Mar. 2016, ISSN: 1942-4302. DOI: 10.1115/1.4031954. eprint: https://asmedigitalcollection.asme.org/mechanismsrobotics/article-pdf/8/3/031003/6253263/jmr_008_03_031003.pdf. [Online]. Available: https://doi.org/10.1115/1.4031954.

[20] S. M. Felton, M. T. Tolley, B. Shin, *et al.*, "Self-folding with shape memory composites," *Soft Matter*, vol. 9, pp. 7688–7694, 32 2013. DOI: 10.1039/C3SM51003D. [Online]. Available: http://dx.doi.org/10.1039/C3SM51003D.

[21] D. Misseroni, P. P. Pratapa, K. Liu, *et al.*, "Origami engineering," *Nature Reviews Methods Primers*, vol. 4, no. 1, Jun. 2024. DOI: 10.1038/s43586-024-00313-7. [Online]. Available: https://www.nature.com/articles/s43586-024-00313-7.

[22] C. F. Gauss, "Disquisitiones generales circa superficies curvas typis diterici-anis," 1828.

[23] B. Audoly and Y. Pomeau, *Elasticity and Geometry: From Hair Curls to the Non-linear Response of Shells*, en. Oxford University Press, Jun. 2010, Google-Books-ID: FMQRDAAAQBAJ, ISBN: 978-0-19-850625-6.

[24] C. D. Modes, K. Bhattacharya, and M. Warner, "Gaussian curvature from flat elastica sheets," *Proceedings of the Royal Society A: Mathematical, Physical and Engineering Sciences*, vol. 467, no. 2128, pp. 1121–1140, Oct. 20, 2010, Publisher: Royal Society. DOI: 10.1098/rspa.2010.0352. [Online]. Available: https://royalsocietypublishing.org/doi/10.1098/rspa.2010.0352.

[25] K. Crane. "A quick and dirty introduction to the curvature of surfaces – geometry processing and applications WS19." (2019), [Online]. Available: http://wordpress.discretization.de/geometryprocessingandapplicationsws19/a-quick-and-dirty-introduction-to-the-curvature-of-surfaces/.

[26] R. Sawhney and K. Crane, "Boundary first flattening," *ACM Trans. Graph.*, vol. 37, no. 1, Dec. 2017, ISSN: 0730-0301. DOI: 10.1145/3132705. [Online]. Available: https://doi.org/10.1145/3132705.

[27] R. Schinzinger and P. A. A. Laura, *Conformal Mapping: Methods and Applications*. Courier Corporation, Apr. 30, 2012, 628 pp., ISBN: 978-0-486-15074-1.

[28] L. Kharevych, B. Springborn, and P. Schröder, "Discrete conformal mappings via circle patterns," *ACM Transactions on Graphics (TOG)*, Apr. 1, 2006, Publisher: ACMPUB27New York, NY, USA. DOI: 10.1145/1138450.1138461. [Online]. Available: https://dl.acm.org/doi/10.1145/1138450.1138461.

[29] V. Parque, W. Suzaki, S. Miura, A. Torisaka, T. Miyashita, and M. Natori, "Packaging of thick membranes using a multi-spiral folding approach: Flat and curved surfaces," *Advances in Space Research*, vol. 67, no. 9, pp. 2589–2612, 2021, Solar Sailing: Concepts, Technology, and Missions II, ISSN: 0273-1177. DOI: https://doi.org/10.1016/j.asr.2020.09.040. [Online].

Available: https://www.sciencedirect.com/science/article/pii/S0273117720306876.

[30] *Origami-Inspired Optical Shield for a Starshade Inner Disk Testbed: Design, Fabrication, and Analysis*, Jan. 2021. DOI: 10.2514/6.2021-0904.

[31] S. Wang, Y. Gao, H. Huang, B. Li, H. Guo, and R. Liu, "Design of deployable curved-surface rigid origami flashers," *Mechanism and Machine Theory*, vol. 167, p. 104 512, 2022, ISSN: 0094-114X. DOI: https://doi.org/10.1016/j.mechmachtheory.2021.104512. [Online]. Available: https://www.sciencedirect.com/science/article/pii/S0094114X21002664.

[32] I. Fiorello, O. Tricinci, G. Naselli, *et al.*, "Climbing plant-inspired micropatterned devices for reversible attachment," *Advanced Functional Materials*, vol. 30, p. 2 003 380, Jul. 2020. DOI: 10.1002/adfm.202003380.

Chapter 4

ANALYSIS OF ELASTIC MEMBRANES WITH RIGID COMPONENTS

4.1 Introduction

While the structured fabric design presented in the previous chapter demonstrated unique mechanical properties and capabilities, a better understanding of the internal mechanics, particularly the strain and stress distribution within the membrane, remained limited. This limitation primarily arises from the experimental challenges in evaluating strain within the membrane, especially when the tiles are fully engaged and conceal the membrane during jamming. This lack of direct observation hinders the ability to assess critical factors such as localized stress concentrations, excessive stretching, and potential failure points within the membrane. Gaining insight into these internal mechanics is essential for future design optimizations, including the refinement of fold patterns, minimization of unnecessary strain, and the reduction of long-term risks such as material fatigue and degradation.

For deployable applications that demand repeatability, durability, and adaptability, understanding the interactions between the membrane and the attached tiles is crucial [1]. Repeated folding and unfolding cycles can introduce localized stress concentrations, increasing the likelihood of membrane tearing or permanent deformation [2]. Therefore, optimizing the structural layout to mitigate these risks is important for ensuring the longevity and functional reliability of the system.

Beyond the specific scope of the structured fabric examined, this line of investigation has broader implications in fields that integrate hyperelastic components with rigid components, such as in soft robotics, where elastic skins are often combined with rigid frames and rigid components [3] are connected by flexible components [4], [5], or in compliant mechanisms [6], where controlled flexibility is used to achieve complex motions. In these systems, the interaction between rigid and flexible elements significantly influences performance, and improper stress distribution can compromise both function and lifespan. Incorporating these findings into future structured fabric designs will not only improve the current system but will also inform the development of other hybrid systems that combine elastic and rigid components [7]. Understanding the nuanced effects of tile patterns, folding dynamics, and

membrane deformation is essential for advancing the design of adaptive, durable, and efficient materials across a wide range of engineering applications [8]–[10].

Numerical simulations offer a powerful tool to bridge the current experimental gaps, allowing for a detailed exploration of the membrane's behavior under various configurations. By systematically varying parameters such as pre-stretch levels, tile spacing, tile density, and folding geometries, simulations can reveal how these factors influence strain localization, stress distribution, and overall mechanical response. This information can guide design strategies to optimize mechanical performance while minimizing the risk of damage.

The finite element method can be used to solve problems involving shape changes from deformations [11]. COMSOL Multiphysics is a finite element analyzer, solver, and simulation software that was used to perform these computations [12]. The membrane in the deployable structured fabric was modeled as a Neo-Hookean material, a type of hyperelastic material model used to describe rubber-like, soft, and biological materials under finite deformations, and is more accurate than linear elasticity for materials that can undergo large elastic deformations [13]. A series of tile pattern configurations and membrane simulations were conducted to evaluate the influence of tile density, tile spacing, and structured fabric folding on the membrane's internal mechanics, strain behavior, and stress distribution.

4.2 Neo-Hookean Hyperelastic Materials

Hyperelastic constitutive laws are designed to model materials that exhibit elastic behavior even under very large strains, capturing both nonlinear material responses and significant shape changes. These models are particularly suited for materials like rubbers and polymeric foams, which can undergo large, reversible deformations [14]. In this analysis, the structured fabric incorporates a rubber membrane, making the hyperelastic framework especially relevant for representing the rubber-like behavior of the polymeric material [15].

Several key characteristics of solid rubber are relevant to our setup and analysis [13]. The material behaves as an ideal elastic solid, where, under constant temperature, stress depends solely on the current strain, independent of loading history or rate. The deformation is fully reversible, with the material returning to its original shape upon unloading. The material exhibits a strong resistance to volume changes, characterized by a high bulk modulus, which relates volumetric strain to hydrostatic stress. It is highly compliant in shear, with a shear modulus significantly lower, by

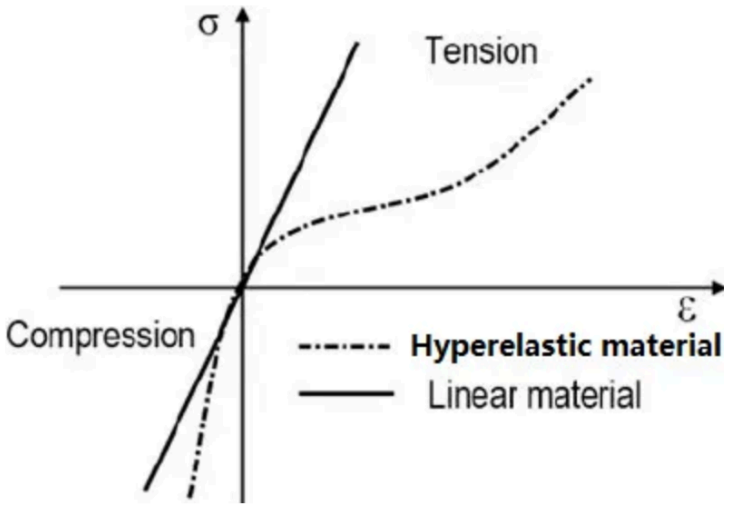

Figure 4.1: An example of a hyperelastic material's stress strain curve compared to that of a linear-elastic material [16].

several orders of magnitude, than that of typical metals. The material is isotropic, meaning its stress-strain response remains consistent regardless of orientation. This combination of properties makes hyperelastic models ideal for capturing the mechanical behavior of the rubber membrane within our structured fabric of interest.

All hyperelastic models are constructed in the following way. The stress-strain relationship is defined by specifying a strain energy density W as a function of the deformation gradient tensor F to ensure the material is perfectly elastic, which also simplifies the analysis by working with a scalar function. The form of W incorporates material-specific properties that can be adjusted to model different materials. The undeformed material is usually assumed to be isotropic i.e the behavior of the material is independent of the initial orientation of the material with respect to the loading. Formulas for stress in terms of strain are calculated by differentiating the strain energy density. The strain energy in terms of the deformation gradient $F_{ij} = \delta_{ij} + \frac{\partial u_i}{\partial x_j}$ is

$$\sigma_{ij} = \frac{1}{J} F_{ik} \frac{\partial W}{\partial F_{kj}}. \tag{4.1}$$

Generalized Neo-Hookean solid

The specific form of strain energy density for a generalized Neo-Hookean solid is [17]:

$$\bar{U} = \frac{\mu_1}{2} \left(\frac{\text{trace}(FF^T)}{J^{2/3}} - 3 \right) + \frac{K_1}{2} (J-1)^2 \tag{4.2}$$

where J is the Jacobian of the Deformation, μ_1 and $K1$ are material properties and are the shear modulus and bulk modulus of the solid, respectively, and the bulk modulus can be calculated from the Lamé parameters by $\kappa = \lambda + 2\mu/3$. The material value of μ_1 can be determined based on the number of polymer chains per unit volume, the Boltzmann constant, and the temperature, which we assume to be constant. This rubber elasticity model is used with rubbers with very limited compressibility, and should be used with $K_1 << \mu_1$. The stress-strain relation follows as (with $B = FF^T$):

$$\sigma_{ij} = \frac{\mu_1}{J^{5/3}} \left(B_{ij} - \frac{1}{3} B_{kk} \delta_{ij} \right) + K_1 (J - 1) \delta_{ij}. \tag{4.3}$$

Finite Element Method for Large Deformations: Hyperelastic Materials
Summary of Governing Equations

The following parameters are given to begin the finite element study [13]:

- The shape of the sheet in its unloaded condition R_0 ,the stress free reference configuration. In our simulation this is membrane without stretching or adhered rigid components.
- A body force distribution b acting on the solid, a body force distribution acting on the solid, in force per unit mass. In the first study step of the simulation, this is the prestrain applied to the body of the membrane. In the second study step of the simulation, the prestrain is released from the body of the membrane, and a light foundation spring is attached to the tile in the center to prevent rigid body motion.
- Boundary conditions, specifying displacements $u^*(x)$ on a portion $\partial_1 R$ or tractions $t^*(x)$ on a portion $\partial_2 R$ of the boundary of the deformed solid where tractions are specified as force per unit deformed area. In the first study step of the simulation, the prestrain applied is held in place by a fixed boundary condition on the boundary of the membrane, in addition to the rigid tiles being placed in this prestretched configuration. In the second study step of the simulation, the rigid tiles remain adhered but the fixed boundary condition is removed.
- The material constants μ_1 and K_1 from the previous section describing the Neo-Hookean constitutive law. In our simulation, the values can be found in

Appendix 3.

- The mass density of the solid in its reference configuration, ρ which in the simulations remains constant throughout and across each of them. In our simulation, the values can be found in Appendix 3.

Then the displacements μ_i, deformation gradient tensor F_{ij} and Cauchy stresses σ_{ij} are calculated such that the governing equations and boundary conditions are satisfied:

$$y_i = x_i + u_i(x_k) \tag{4.4}$$

$$\text{Deformation Gradient: } F_{ij} = \delta_{ij} + \frac{\partial \mu_i}{\partial x_j} \tag{4.5}$$

$$\text{Jacobian of the Deformation: } J = det(F) \tag{4.6}$$

$$\text{Left Cauchy-Green Tensor: } B_{ij} = F_{ik}F_{jk} \tag{4.7}$$

$$\text{Equilibrium of Stresses: } \frac{\partial \sigma_{ij}}{\partial y_i} + \rho b_j = 0 \tag{4.8}$$

$$\text{Prescribed Displacements: } \mu_i = \mu_i^* \text{ on } \partial R_1 \tag{4.9}$$

$$\text{Prescribed Tractions: } \sigma_{ij} n_i = t_j^* \text{ on } \partial_2 R \tag{4.10}$$

with σ_{ij}, Cauchy stress, related to the left Cauchy-Green tensor through the Neo-Hookean constitutive law:

$$\sigma_{ij} = \frac{\mu_1}{J^{5/3}}(B_{ij} - \frac{1}{3}B_{kk}\delta_{ij}) + K_1(J-1)\delta_{ij}. \tag{4.11}$$

Principle of Virtual Work and Finite Element Equations

The stress equilibrium equation is replaced by the equivalent principle of virtual work. The nonlinear virtual work equation is [13]:

$$\int_{R_o} \tau_{ij}\delta L_{ij} dV_0 - \int_{R_o} \rho b_i \delta v_i dV_0 - \int_{\partial R} t_i^* \delta v_i dA = 0 \tag{4.12}$$

for all virtual velocity fields $\delta v_i(x_i)$ and virtual velocity gradients $\delta L_{ij} = \frac{\partial v_i}{\partial y_j}$ that satisfy $\delta v_i = 0$ on $\partial_1 R$, and $\tau_{ij} = J\sigma_{ij}$ is the Kirchhoff stress.

The displacement field is discretized, by choosing to calculate the displacement field at a set of n nodes. The coordinates of these special points are denoted in the reference configuration by x_i^a, where the superscript a ranges from 1 to n. The unknown displacement vector at each nodal point is u_i^a.

The displacement field and virtual velocity field at an arbitrary point within the solid is again specified by interpolating between nodal values.

$$u_i(\mathbf{x}) = \sum_{a=1}^{n} N^a(\mathbf{x}) u_i^a \tag{4.13}$$

$$\delta v_i(\mathbf{x}) = \sum_{a=1}^{n} N^a(\mathbf{x}) \delta v_i^a \tag{4.14}$$

where x denotes the coordinates of an arbitrary point in the reference configuration.

And we can compute the deformation corresponding to a given displacement field with:

$$F_{ij} = \delta_{ij} + \frac{\partial u_i}{\partial x_j} = \delta_{ij} + \sum_{a=1}^{n} \frac{\partial v^a}{\partial x_j} u_i^a. \tag{4.15}$$

Then positions within the element can be interpolated as:

$$x_i = \sum_{a=1}^{N_k} N^a\left(\xi_j\right) x_i^a \tag{4.16}$$

where $N^a\left(\xi_i\right)$ are the shape functions in terms of local element coordinates ξ_i.

To solve the nonlinear virtual work equation using Newton-Raphson iterations, an initial guess for u_i^a is made and denoted as w_i^a. Then, an attempt to correct w_i^a in a direction closer to the solution is done by setting $w_i^a \rightarrow w_i^a + dw_i^a$. Ideally the correction would satisfy:

$$\int_{V_0} \tau_{ij} \left[F_{pq}\left(w_k^b + dw_k^b\right) \right] \frac{\partial V^a}{\partial x_m} (F+dF)^{-1}_{mj} dV_0 - \int_{V_0} F_0 b_i N^a dV_0 - \int_{\partial_2 V_0} t_i^* N^a (\eta + d\eta) dA_0 = 0 \tag{4.17}$$

where $F+dF$ denotes the deformation gradient for the updated solution. In addition, the boundary traction integrals are evaluated.

4.3 Numerical Simulation

To replicate the fabrication process of the structured fabrics, in the first step of the study, the prestretch in the membrane defines the body force distribution. In COMSOL Multiphysics, this is done by applying an external strain on the membrane domain, and fixed constraint boundary condition to the hyperelastic membrane edge. The tile geometry is generated from the meshes used in the previous chapter, with filleted corners to decrease the likelihood of stress singularities occurring at the

boundaries of the hyperelastic and rigid materials. The tiles in this step are located in their original tile pattern, as if they were being adhered to the prestretched membrane in Chapter 3. In the second step of the study, the fixed constraint boundary condition applied to the membrane boundary is removed. Additionally, to inhibit the entire material from rigid body translating due the forces it undergoes in this step, a light spring of only 100 N/m is applied to two points within a central tile of the tile pattern.

The mesh size remained constant across all simulations within the same study type, ensuring consistency in the analysis. They were largely determined by accommodating the smallest geometric element, the modified tile corners after filleting. To find the adequacy of the mesh resolution, an analysis was conducted by varying the mesh size until the results reached a plateau. This plateau indicated that further refinement would not significantly affect the outcomes, confirming that convergence was achieved independently of element size reduction. The final mesh size was selected to balance accuracy and computational efficiency, enabling reliable results without excessively increasing run time. Extensive details about the simulation setup can be found in Appendix 3.

4.4 Tile Density Effects

In the previous project, the amount of discretization and consequently, the number of tiles, was determined by the mesh size used when converting the 3D target surface into a mesh. This mesh was then flattened, and its individual faces were transformed into tiles that formed the structured fabric. While employing a finer mesh with a higher number of faces would have resulted in a smoother and less discretized surface, several practical limitations restricted this approach.

Increasing the tile density directly leads to more fabrication complexity. More tiles require greater precision and transfer of adhesive components during assembly, significantly increasing fabrication time and the likelihood of errors. Additionally, the risk of failure during initial trials grows, leading to repeated fabrication attempts. As a result, the previous designs prioritized fabrication feasibility over surface smooth, since they were primarily demonstrating the design process and method.

However, with sufficient resources, especially time, it would be useful to explore the internal mechanics of the membrane when subjected to increased tile densities. Understanding how the membrane behaves under these conditions could inform how different generated meshes behave. They could also inform strategies to optimize

structural integrity, reduce unwanted strain concentrations, and improve overall performance. Having a deeper understanding of the membrane's behavior would enable the design of non-uniform tile distributions, where smaller, denser tiles could be strategically placed in regions requiring greater flexibility or surface smoothness, while larger tiles could be used in less critical areas to simplify fabrication. This adaptive tiling approach could lead to more efficient and versatile structured fabrics, better tailored to complex geometries and specific mechanical demands.

To systematically investigate the impact of tile density on the system's behavior, a tile density factor was introduced, as shown in Fig. 4.2, allowing for controlled variations in discretization while maintaining a constant total area. The same amount of tile spacing was applied to each pattern. Ideally, observed changes are due to the increased number of tiles rather than differences in overall size.

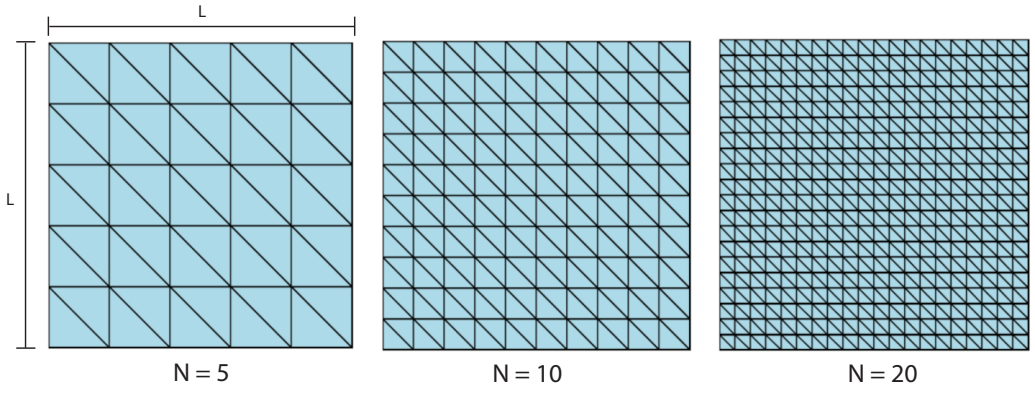

Figure 4.2: The tile pattern set up used to analyze the tile density is shown before a constant spacing is applied. The variable N denotes the number of lengthwise subdivisions applied along each edge of the original surface. The edge length L of the outer dimensions is kept constant across each of the surfaces.

The variable N denotes the number of lengthwise subdivisions applied along each edge of the original surface. Following this subdivision, each resulting square is further divided into two triangular right tiles by cutting along its diagonal, as illustrated in Fig. 4.2, ensuring uniform tile shapes while progressively refining the mesh. As N increases, the total number of tiles grows proportionally to N^2, leading to a denser discretization within the same area. As shown in the design method of the previous chapter, the tiles are then spaced apart by the same spacing factor of 1.2 as shown in Fig. 4.3 and filleted by an amount proportional to their tile size. It is important to note that the system is a hybrid structure, combining

a hyperelastic membrane with extremely rigid tiles that feature sharp corners. In a numerical simulation, these sharp geometric and material transitions naturally induce stress singularities, which can distort simulation results. To mitigate these singularities, filleting was applied to the tile corners. The final fillet proportion was chosen to mitigate stress singularities that permit the use of larger mesh elements for computational efficiency. At the same time, it was kept minimal to better reflect the actual fabrication process, in an attempt to balance numerical stability and experimental accuracy. More details can be found in Appendix 3.

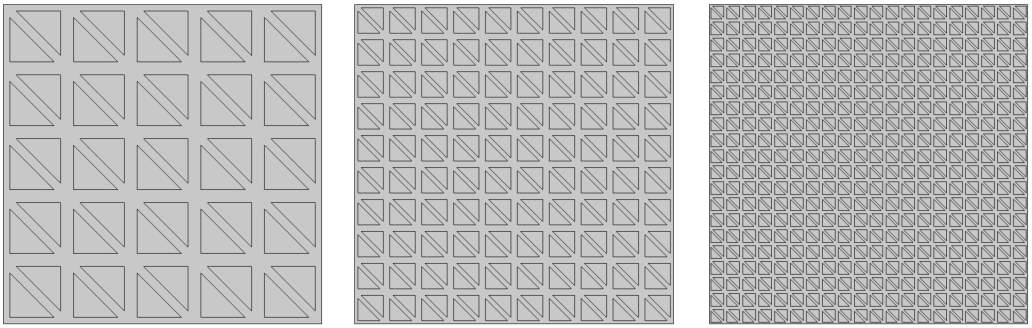

Figure 4.3: The original tile pattern mesh of Fig. 4.2 is distributed to a constant spacing factor of 1.2, to account for the membrane prestretch during fabrication, as explained in the previous chapter.

By maintaining a constant tile density while progressively increasing the membrane's prestretch, it becomes evident that the strain energy within the membrane is unevenly distributed and influenced by kinematic frustrations. Rather than spreading uniformly, the strain energy concentrates in "web-like" patterns, primarily forming along the regions that directly connect neighboring tiles, as shown in Fig. 4.4. The most pronounced strain concentrations occur between each tile and its nearest neighboring tile and nearest neighboring tile with less edge length aligned. Additionally, weaker regions emerge between tiles and their slightly more distant neighbors, though these regions experience comparatively lower strain energy. As the level of membrane prestretch increases, these strain concentrations become even more pronounced, with the highest energy accumulation occurring within the primary connecting webs. This localized build-up of strain highlights critical areas of stress.

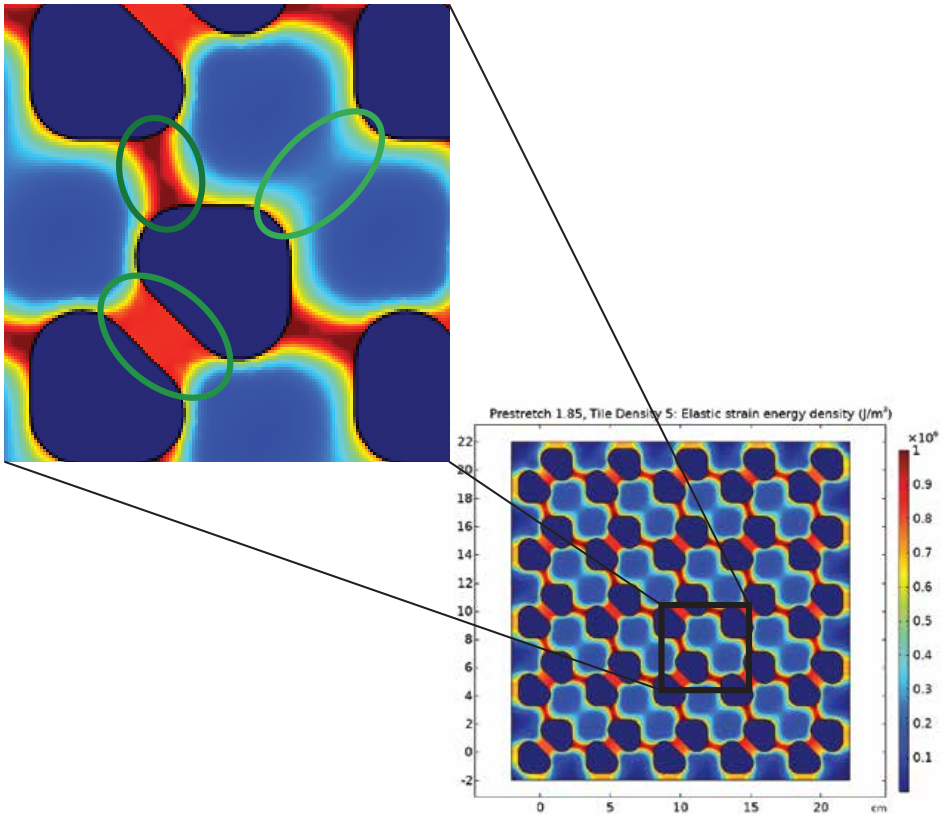

Figure 4.4: An enlarged view of where "webs" occur, where strain energy concentrates, with greater concentrations occurring between a tile and its nearest neighboring tile with less edge length aligned.

As the level of membrane prestretch increases, these strain concentrations become even more pronounced, with the highest energy accumulation occurring within the primary connecting webs, as shown in Fig. 4.5. While the total amount of strain energy in the system increases, the increases are primarily happening in those specific regions.

By maintaining a constant prestretch while increasing the tile density, as shown in Fig. 4.6, it is observed that the stress concentration regions, or webs, become progressively thinner and more localized. As the tile size decreases, the regions through which stress is transmitted are confined to smaller areas, leading to a higher stress intensity within these webs. This is likely a consequence of the strain energy being distributed over a reduced area, causing an amplification of local stresses as the membrane accommodates the same global deformation through finer, more densely packed tiles.

A summary of the data for varying tile densities across different membrane pre-

stretches is presented in Fig. 4.7 and Fig. 4.8.

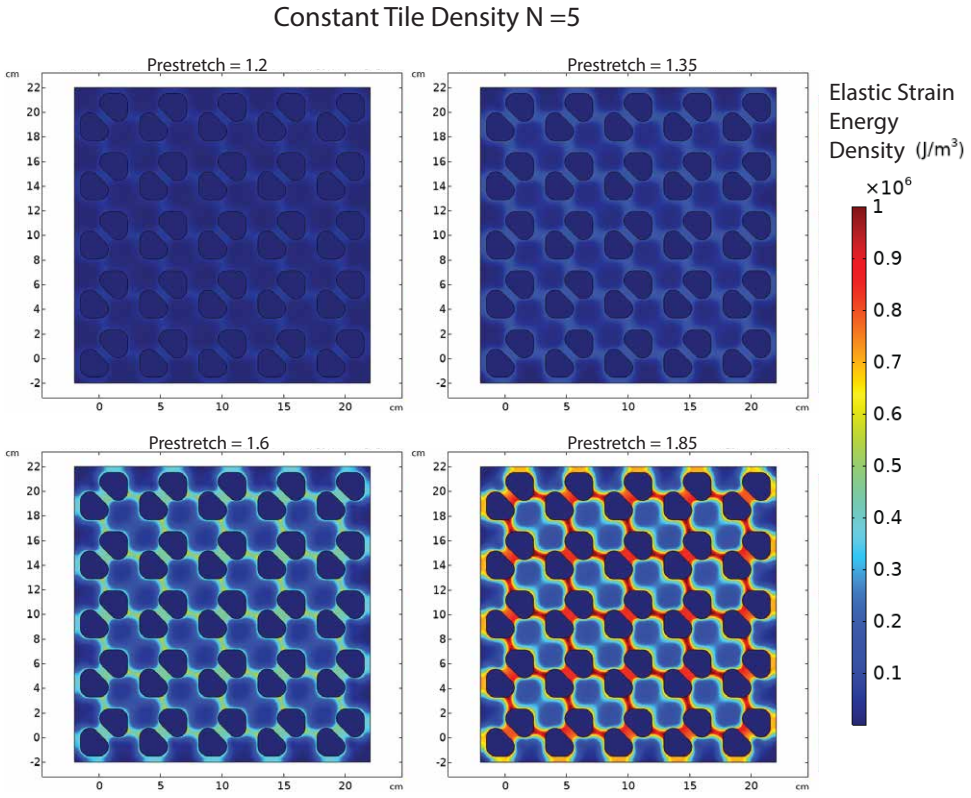

Figure 4.5: Surface plots of strain energy density are shown for a tile pattern of N= 5 after being released from varying prestretch factors.

In Fig. 4.7, increasing the tile density factor leads to a rise in strain energy density. This increase occurs because higher tile densities result in more stress accumulating webs, which become thinner and more concentrated as the tile size decreases. For each level of membrane prestretch, the left plot displays the strain energy density as a percentage change relative to the baseline case with a tile density factor of 2 at the same prestretch level. This normalization highlights the relative impact of increasing tile density within each prestretch scenario. The plot on the right side presents the absolute values of strain energy density, allowing for direct comparison of the magnitude of changes between different prestretch levels. Due to significant differences in scale across prestretch conditions, the percentage change plots on the left provide clearer insight into the internal trends for each case.

Similarly, Fig. 4.8 illustrates how the maximum stress evolves with increasing tile density. While the overall trend mirrors that of the strain energy density, showing

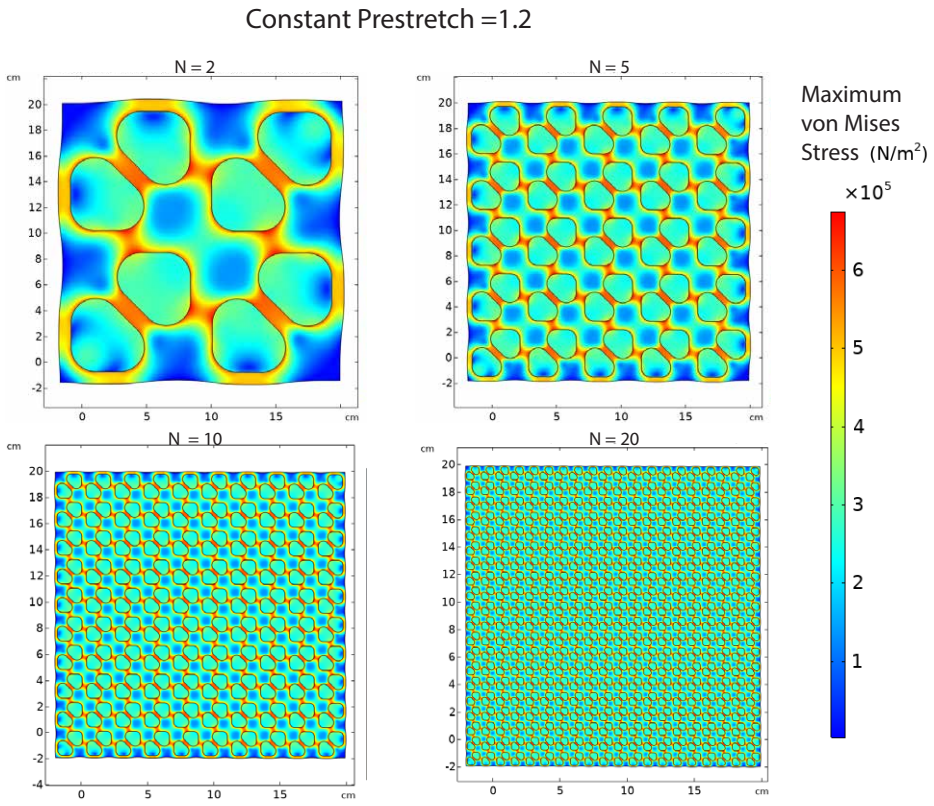

Figure 4.6: Surface plots of the maximum von Mises stresses are shown after releasing the membranes from a prestretch of 1.2 for varying tile densities.

an increase in stress with higher tile densities, the rate of increase differs due to the nonlinear relationship between stress and strain. The right plot highlights the scale of stress values across different prestretches, while the plot on the left side focuses on the percentage change within each prestretch level, allowing for a clearer comparison of relative effects. The increase in prestrain of the material amplifies localized effects, as shown in the plot on the left.

To mitigate stress singularities in the evaluation of maximum values, filleting was applied to the tile corners, as previously discussed, along with mesh optimization to smooth extreme gradients and enhance numerical stability. Despite these refinements, residual numerical artifacts persist, leading to minor irregularities in certain regions of the graphs. Together, these figures reveal how both strain energy density and stress are influenced by the interplay between tile density and membrane prestretch.

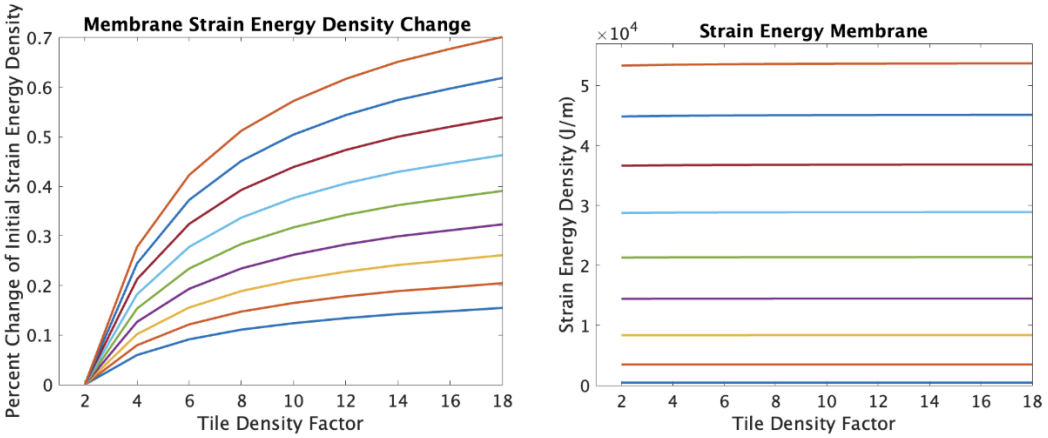

Figure 4.7: For an increasing tile density, the left plot normalizes strain energy density as a percentage change relative to a baseline tile density factor of 2, while the right plot displays absolute values for direct comparison of magnitudes across prestretch levels.

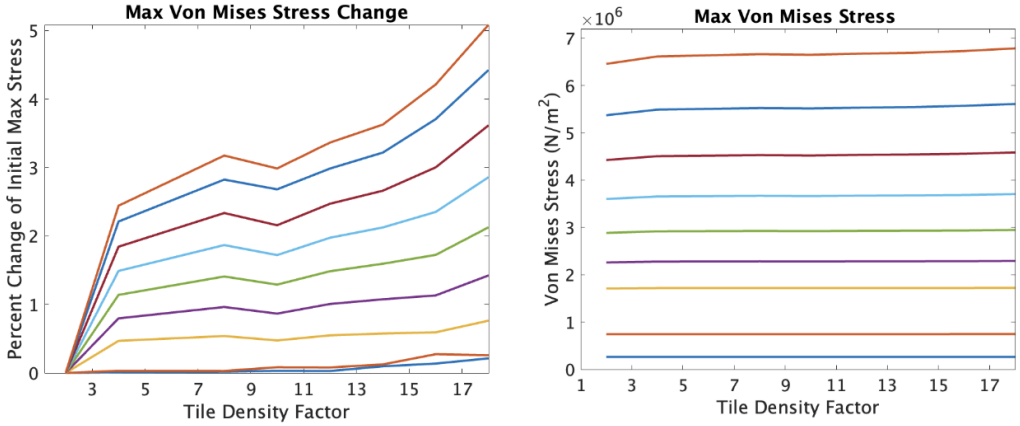

Figure 4.8: For an increasing tile density, the left plot normalizes maximum von Mises Stress as a percentage change relative to a baseline tile density factor of 2, while the right plot displays absolute values for direct comparison of magnitudes across prestretch levels.

4.5 Tile Spacing Effects

The spacing between tiles can also be systematically varied to explore its impact on the overall structure. The tile pattern utilized in this analysis is consistent with the design from the previous chapter's paraboloid structure, where tiles of identical shape, size, and relative orientation were maintained as shown in Fig. 4.9. The variation lies in the adjustment of spacing, achieved through an isotropic rigid body

translation of each tile. This approach ensures that while the fundamental geometry of the tile pattern remains unchanged, the inter-tile gaps can be controlled to study their influence on the membrane's mechanical behavior and strain distribution.

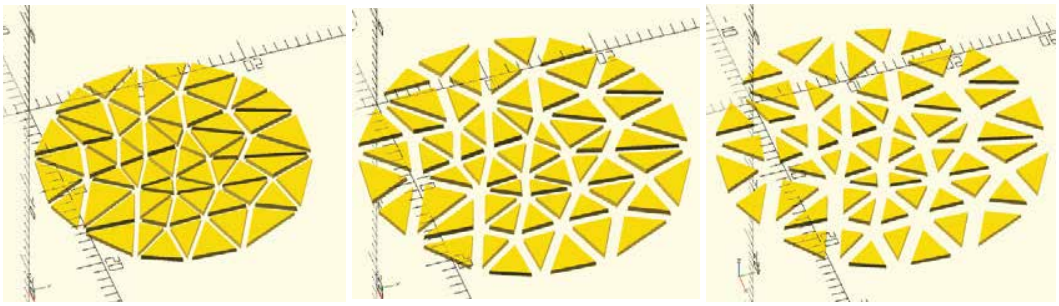

Figure 4.9: Tile spacing is varied while maintaining the same pattern and design as the previous chapter's paraboloid structure. sf is the spacing factor of those tiles.

The variable sf represents the scaling factor applied to adjust the spacing between tiles, based on the expansion of the original pattern. To achieve this, the centroids of the expanded tiles serve as reference points, allowing the tiles to be isotropically distributed while maintaining their original size, orientation, and relative arrangement. Like the previous section using identical triangles, we can observe webs between a tile and its neighbor, with smaller tiles and closer neighbors resulting in more concentrated strains and therefore stresses. As the prestretch increases, those particular regions become more pronounced.

Analyzing the effects of tile spacing, we can first observe that the outer rim undergoes significant contraction, as it is not constrained by neighboring tiles that would otherwise resist the release of prestretch. Consequently, the frustrations near the outer rim experience a greater impact from this contraction compared to the interior tiles, which are more effectively buffered by their surrounding neighbors. This effect can be seen in Fig. 4.11, where the whole structure undergoes compression, but with greater intensity observed further from the center. Kinematic frustrations could be quantified in these displacement plots by comparing the amount of displacement occurring in a released membrane with versus without a tile pattern.

As the spacing between tiles increases, the tiles become less affected by neighboring constraints, making them more susceptible to prestretch release effects in the rim. This phenomenon is particularly pronounced near the outer rim, where the tiles are more isolated, leading to a greater overall contraction effect.

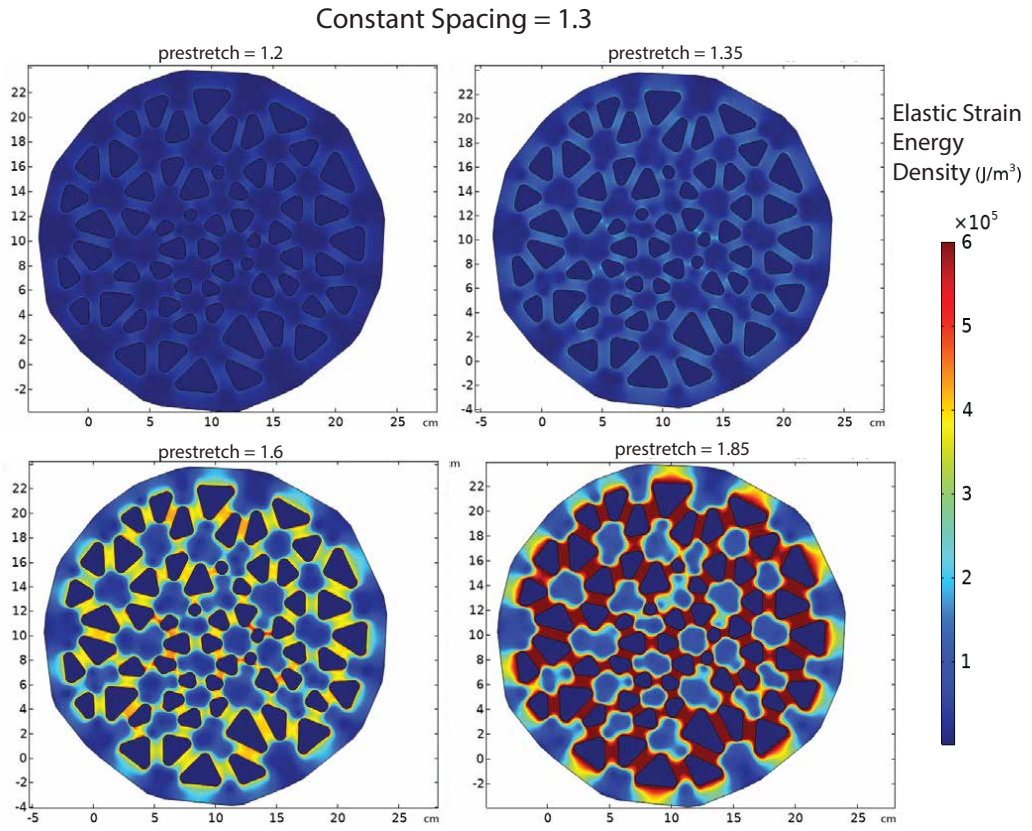

Figure 4.10: Surface plots of strain energy density are shown for a paraboloid tile pattern of constant spacing sf = 1.3, across different prestretches it is released from.

In the tile pattern used, smaller tiles are positioned near the center of the structure. The resulting stress distributions reveal a distinct trend where for small spacing factors sf, stress concentrations are higher in the center. For large spacing factors, the stress shifts toward the outer rim. This shift in stress localization can be attributed to at least two factors. As the spacing increases, the characteristic web lengths begin to align more closely with the larger tiles near the outer region, reducing the dominance of stress concentrations in the center. In addition, the outermost tiles become increasingly isolated as spacing increases, making them less buffered from the prestretch-induced contraction of the outer rim. Since these tiles experience fewer kinematic constraints, the release of prestretch results in heightened stress accumulation in these regions.

As the spacing factor increases, a larger portion of the system undergoes kinematic frustration, resulting in a higher buildup of strain strain energy. This occurs because the tile pattern expands, while individual tile sizes remain unchanged, leading to

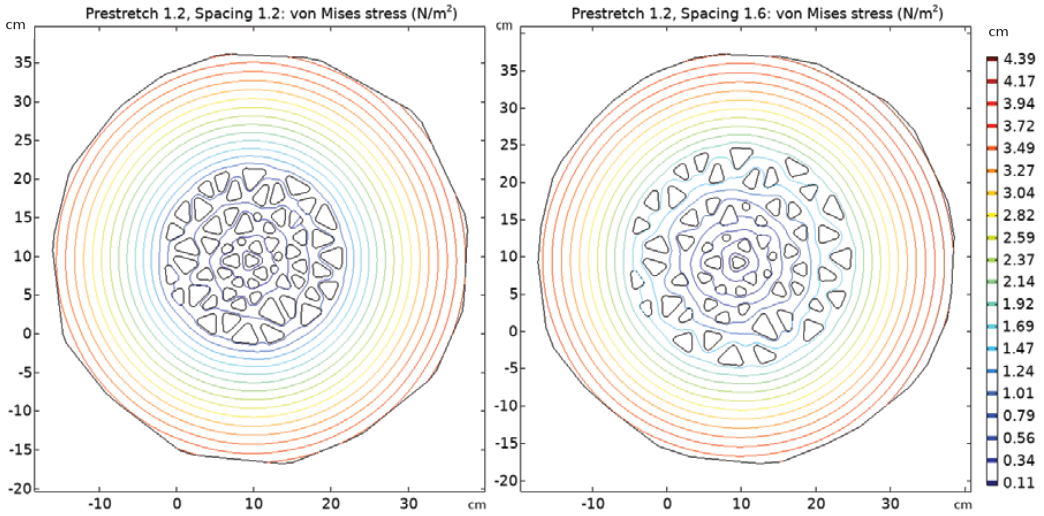

Figure 4.11: Contour displacement plots of the tile patterns at two different spacings.

elevated strain energy density and enhanced stress localization. To elucidate these effects, in Fig. 4.13, the left-hand plot displays percentage changes relative to a baseline tile density factor of 1.2, highlighting relative trends within each prestretch level. In contrast, the right-hand plot presents the absolute values, allowing for a direct comparison of magnitude differences across various prestretch conditions.

The relationship between tile spacing and stress follows a similar trend to strain energy density, though the rate of increase varies due to the nonlinear stress-strain response of the hyperelastic membrane. Higher prestrain amplifies localized effects, as illustrated in the percentage change plots.

Since the system consists of rigid tiles embedded in a hyperelastic membrane, sharp geometric transitions naturally introduce stress singularities in simulations. To reduce these effects, filleting of tile corners and mesh optimization were also applied to improve numerical stability. However, some residual artifacts remain. Overall, the figures illustrate how strain energy density and stress distributions are shaped by the interplay between tile spacing and membrane prestretch, providing critical insights for optimizing structured fabric designs.

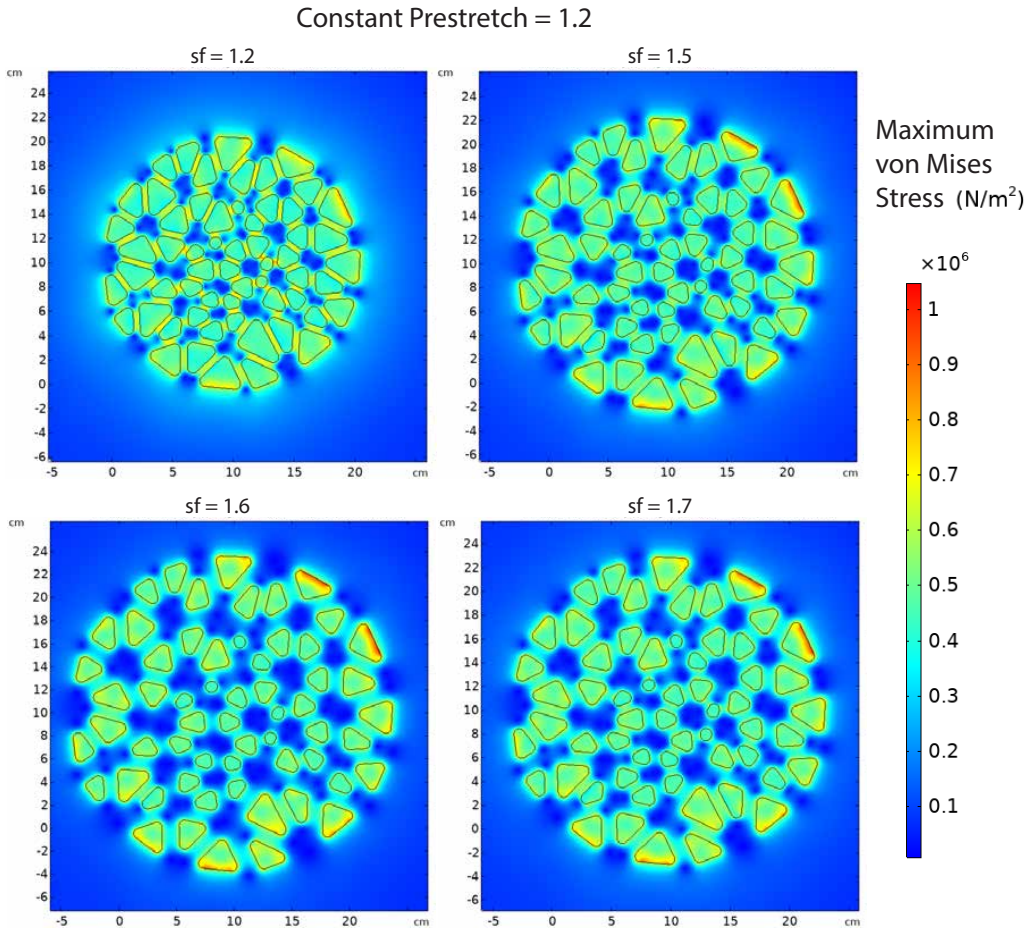

Figure 4.12: Surface plots of maximum von Mises stress are shown after releasing the membrane's prestretch for a paraboloid tile pattern of constant prestretch of 1.2, across increasing spacing factors.

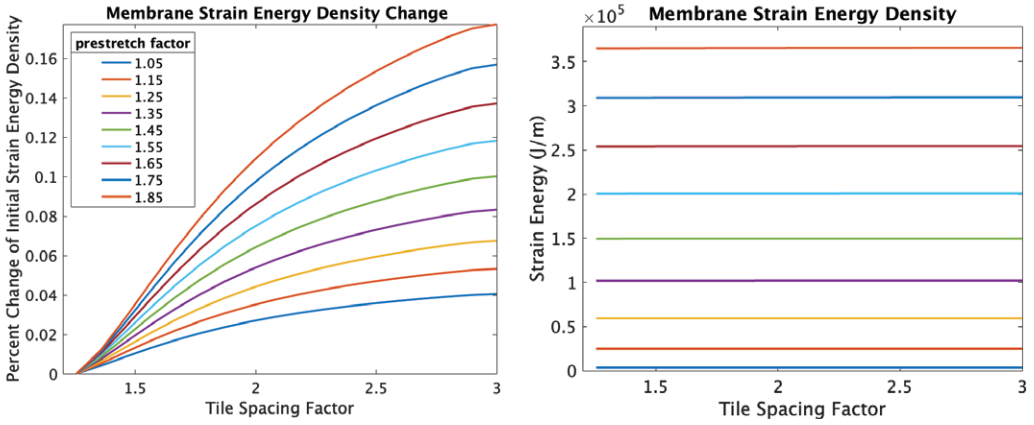

Figure 4.13: For an increasing tile density, the left plot normalizes strain energy density as a percentage change relative to a baseline spacing factor of 1.2, while the right plot displays absolute values for direct comparison of magnitudes across prestretch levels.

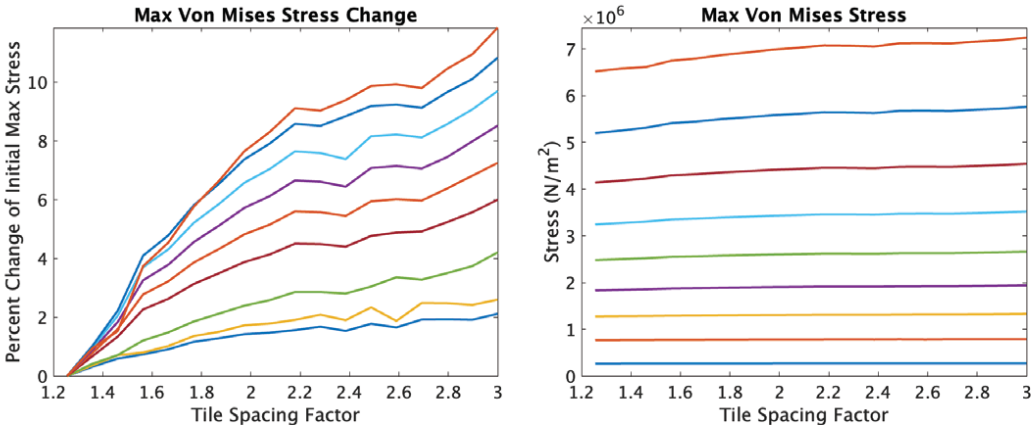

Figure 4.14: For an increasing tile density, the left plot normalizes maximum von Mises Stress as a percentage change relative to a baseline spacing factor of 1.2, while the right plot displays absolute values for direct comparison of magnitudes across prestretch levels.

4.6 Folding

In the previous chapter, we discussed how folding plays a crucial role in structured fabrics, enabling the design to compact along predetermined fold lines inspired by origami, allowing for compact and efficient folding patterns. However, fabrication and experimental observations revealed that failure most commonly occurred in these folding regions, where the membrane undergoes a combination of bending and stretching. The behavior of the folding is primarily determined by the geometry of the tiles, with thickness being the greatest factor. Directly modeling the adhesion of tiles on both the top and bottom of the membrane, along with the contact interactions between rigid elements, would be very computationally expensive. In addition, the membrane was modeled as a 2D cross-section of the full membrane with the plane-strain assumptions.

To address this, the folding behavior was instead simulated using geometric boundary conditions, which effectively capture the constraints imposed by tile interactions, as illustrated in Fig. 4.15. Observations during fabrication and experimentation showed that the bottom tiles collide, causing the membrane to hinge around the bottom two corners, marked by the red dot. Upon collision, the central portion of the membrane begins to stretch, allowing both ends to rotate about the hinge point.

The folding process continues until the tile edges make full contact, at which point the membrane takes on a U-shaped bend. Theoretically, the adhesive area beneath each tile, which is slightly smaller than the tile itself, remains fixed and unable to stretch, as it is bonded to a rigid surface. The adhesives create a small gap of untouched membrane, which is represented by $2L_x$. This also results in localized bending near the tile corners, while the middle portion of the membrane undergoes stretching, potentially leading to necking between the bending regions.

Simulation results illustrate the final membrane configuration for varying tile thicknesses. As tile thickness increases, stress concentrations become more pronounced, particularly in the central region, where visible necking occurs due to intensified strain. While the overall deformation profile remains similar, the middle section elongates, becoming more stretched and thinner, while the corners also begin to thin, though to a lesser extent. As the tile thickness and collision effects increase, the stretching in the middle intensifies, leading to higher localized stress, as indicated by the increasing red regions in the simulation.

The relationship between tile thickness and von Mises stress behavior is expected due to the nonlinear nature of the material. When combined with bending effects

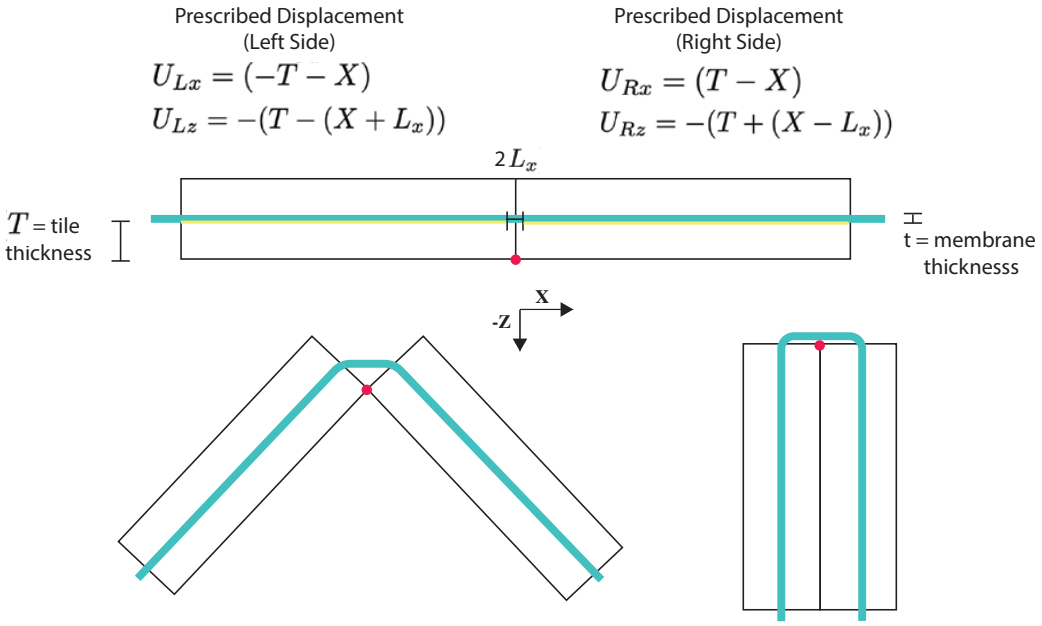

Figure 4.15: The prescribed displacement equations shown are applied to both halves in the yellow region, defining the boundary conditions. The red dot marks the hinge point, around which the rubber bends due to the tile interaction. The diagram beneath the equations illustrates the initial configuration before deformation. The bottom left image captures an intermediate stage of the folding process, while the bottom right image depicts the final folded state, showing the progression of the structure as it deforms.

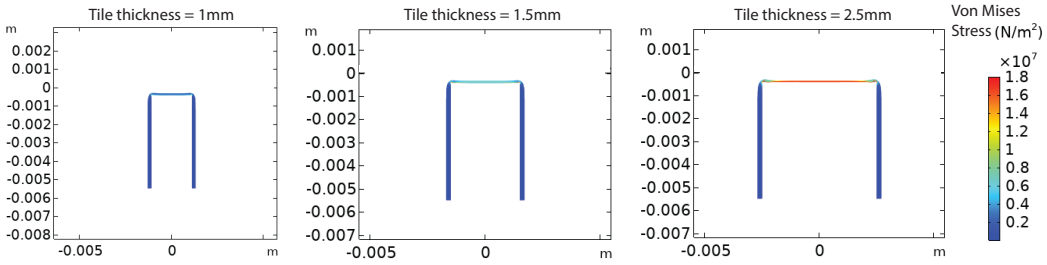

Figure 4.16: Simulation results of the final membrane configuration are shown for varying tile thicknesses.

at the tile corners, this results in an exponential stress profile. By placing probes at different locations, specifically in the middle and at a single corner (leveraging symmetry), we confirm that the majority of deformation occurs in the central region. Furthermore, as tile thickness increases, stress in this central area escalates at a

significantly faster rate compared to the corners, highlighting the concentration of strain in the middle of the membrane.

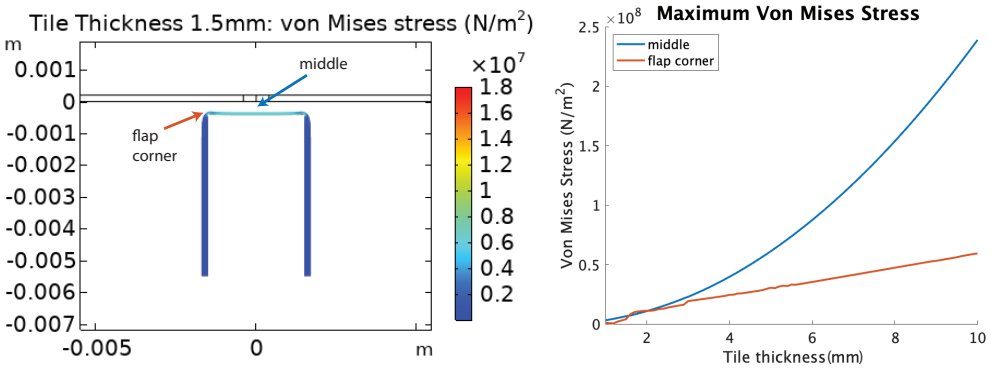

Figure 4.17: On the left, a plot of the final deformation is shown, where probes were placed in the middle and at the corner. For increasing tile thicknesses, the maximum von Mises stress recorded at those locations was recorded in the plot on the right.

4.7 Conclusion

This chapter provided a deeper understanding of the internal mechanics of the deployable 3D structure introduced in the previous chapter, focusing on strain and stress distribution within the membrane. Finite element simulations using a hyperelastic Neo-Hookean model were employed to replicate the behavior of the structured fabric upon the release of prestress, mirroring the fabrication process. By systematically varying parameters such as prestretch levels, tile spacing, tile density, and folding geometries, these simulations revealed how different factors influence strain energy distribution, stress localization, and overall mechanical response.

These insights offer guidance for optimizing design strategies to enhance mechanical performance while minimizing structural weaknesses. The study demonstrated how careful placement of fold lines can prevent excessive strain energy accumulation, reducing the risk of material failure. If overlapping folds are unavoidable, they can be accounted for by considering the previously folded segment as an effective increase in tile thickness. While further exploration of parameter interactions could provide additional refinements, such an approach would be computationally intensive. Nonetheless, the findings can be further integrated into the existing tile pattern generation framework to optimize fold lines and tile arrangements for improved structural efficiency.

4.8 Acknowledgments

I would like to thank Alexander Ogren for his help and vast knowledge of FEM and COMSOL Multiphysics with Matlab integration, Jagannadh Boddapati for his advice on setting up this problem, and Sahangi Dassanayake for helping me with analyzing results. This work was partially funded by Heritage Medical Institute.

4.9 Bibliography

References

[1] G. E. Fenci and N. G. Currie, "Deployable structures classification: A review," *International Journal of Space Structures*, vol. 32, no. 2, pp. 112–130, Jun. 1, 2017, Publisher: SAGE Publications Ltd STM, ISSN: 0956-0599. DOI: 10.1177/0266351117711290. [Online]. Available: https://doi.org/10.1177/0266351117711290.

[2] L. Lanzoni and A. M. Tarantino, "Damaged hyperelastic membranes," *International Journal of Non-Linear Mechanics*, vol. 60, pp. 9–22, Apr. 1, 2014, ISSN: 0020-7462. DOI: 10.1016/j.ijnonlinmec.2013.12.001. [Online]. Available: https://www.sciencedirect.com/science/article/pii/S0020746213002138.

[3] A. Sadeghi, A. Mondini, E. Del Dottore, A. K. Mishra, and B. Mazzolai, "Soft-legged wheel-based robot with terrestrial locomotion abilities," *Frontiers in Robotics and AI*, vol. 3, Dec. 2, 2016, Publisher: Frontiers, ISSN: 2296-9144. DOI: 10.3389/frobt.2016.00073. [Online]. Available: https://www.frontiersin.org/journals/robotics-and-ai/articles/10.3389/frobt.2016.00073/full.

[4] A. De Luca and W. J. Book, "Robots with flexible elements," in *Springer Handbook of Robotics*, B. Siciliano and O. Khatib, Eds., Cham: Springer International Publishing, 2016, pp. 243–282, ISBN: 978-3-319-32552-1. DOI: 10.1007/978-3-319-32552-1_11. [Online]. Available: https://doi.org/10.1007/978-3-319-32552-1_11.

[5] F. Ilievski, A. D. Mazzeo, R. F. Shepherd, X. Chen, and G. M. Whitesides, "Soft robotics for chemists," *Angewandte Chemie International Edition*, vol. 50, no. 8, pp. 1890–1895, 2011, ISSN: 1521-3773. DOI: 10.1002/anie.201006464. [Online]. Available: https://onlinelibrary.wiley.com/doi/abs/10.1002/anie.201006464.

[6] L. L. Howell, *Compliant Mechanisms*. John Wiley & Sons, Aug. 3, 2001, 484 pp., Google-Books-ID: tiiSOuhsIfgC, ISBN: 978-0-471-38478-6.

[7] J. A. C. Ambrósio, "Impact of Rigid and Flexible Multibody Systems: Deformation Description and Contact Models," en, in *Virtual Nonlinear Multibody Systems*, W. Schiehlen and M. Valášek, Eds., Dordrecht: Springer Netherlands, 2003, pp. 57–81, ISBN: 978-94-010-0203-5. DOI: 10.1007/978-94-

010-0203-5_4. [Online]. Available: https://doi.org/10.1007/978-94-010-0203-5_4.

[8] L. Pocivavsek, R. Dellsy, A. Kern, *et al.*, "Stress and fold localization in thin elastic membranes," *Science*, vol. 320, no. 5878, pp. 912–916, May 16, 2008, Publisher: American Association for the Advancement of Science. DOI: 10.1126/science.1154069. [Online]. Available: https://www.science.org/doi/full/10.1126/science.1154069.

[9] W. D. Reynolds, S. K. Jeon, J. A. Banik, and T. W. Murphey, "Advanced folding approaches for deployable spacecraft payloads," 2014. DOI: 10.1115/DETC2013-13378. [Online]. Available: https://dx.doi.org/10.1115/DETC2013-13378.

[10] M. C. Natori, N. Katsumata, H. Yamakawa, H. Sakamoto, and N. Kishimoto, "Conceptual model study using origami for membrane space structures," 2013. DOI: 10.1115/DETC2013-13490. [Online]. Available: https://dx.doi.org/10.1115/DETC2013-13490.

[11] D. W. Nicholson, N. W. Nelson, B. Lin, and A. Farinella, "Finite element analysis of hyperelastic components," *Applied Mechanics Reviews*, vol. 51, no. 5, pp. 303–320, May 1, 1998, ISSN: 0003-6900. DOI: 10.1115/1.3099007. [Online]. Available: https://doi.org/10.1115/1.3099007.

[12] C. Multiphysics, "Introduction to comsol multiphysics®," *COMSOL Multiphysics, Burlington, MA, accessed Feb*, vol. 9, no. 2018, p. 32, 1998.

[13] A. F. Bower. "Applied mechanics of solids (a.f. bower) chapter 8: Theory of FEA -8.4 finite strain elasticity." (2008), [Online]. Available: https://solidmechanics.org/text/Chapter8_4/Chapter8_4.htm.

[14] A. Wineman, "Some results for generalized neo-hookean elastic materials," *International Journal of Non-Linear Mechanics*, Special Issue in Honour of C.O. Horgan, vol. 40, no. 2, pp. 271–279, Mar. 1, 2005, ISSN: 0020-7462. DOI: 10.1016/j.ijnonlinmec.2004.05.007. [Online]. Available: https://www.sciencedirect.com/science/article/pii/S0020746204000587.

[15] L. J. Hart-Smith and J. D. C. Crisp, "Large elastic deformations of thin rubber membranes," *International Journal of Engineering Science*, vol. 5, no. 1, pp. 1–24, Jan. 1, 1967, ISSN: 0020-7225. DOI: 10.1016/0020-7225(67)90051-1. [Online]. Available: https://www.sciencedirect.com/science/article/pii/0020722567900511.

[16] E. M. Arruda and M. C. Boyce, "A three-dimensional constitutive model for the large stretch behavior of rubber elastic materials," *Journal of the Mechanics and Physics of Solids*, vol. 41, no. 2, pp. 389–412, 1993, ISSN: 0022-5096. DOI: https://doi.org/10.1016/0022-5096(93)90013-6.

[17] F. S. Wong and R. T. Shield, "Large plane deformations of thin elastic sheets of neo-hookean material," *Zeitschrift für angewandte Mathematik und Physik ZAMP*, vol. 20, no. 2, pp. 176–199, Mar. 1, 1969, ISSN: 1420-9039. DOI: 10.1007/BF01595559. [Online]. Available: https://doi.org/10.1007/BF01595559.

Chapter 5

CONCLUSION

This research advances the understanding and development of structured fabrics by exploring their tunable mechanical properties and deployable capabilities. This thesis begins with a structured fabric design inspired by structured media and chainmail, utilizing topological interlocking to transition between flexible and rigid states. The effects of particle parameters on the global structure were studied both experimentally and computationally. The ability to control stiffness of a structured fabric through tensioned wires highlights the potential for designing adaptable materials that can transition between soft and rigid states, making them applicable for wearable devices and soft robotics. Initially, these structures maintained flat-plane global geometries. However, the concept was later explored for its potential to induce shape change in addition to stiffness transitions, leading to considerations of how structured fabrics could be improved for deployable applications. The actuation mechanism was modified to a prestretched membrane, with a focus on computationally designing the building blocks to enable shape transformation, preprogrammed compaction, and increased stiffness. This resulted in the ability to apply origami folding patterns which are traditionally made for 2D surfaces, on to 3D surfaces that are stable and load bearing, without any rigid mechanisms. While these demonstrations showcased the design methodology's ability to achieve these unique properties, further investigation was conducted to better understand the internal mechanics of the structures. Finite element analysis was employed to examine kinematic frustrations and stress distributions under varying conditions, such as tile density, tile spacing, and folding. These simulations inform future design optimizations for enhanced structural stability, durability, and efficiency. Through this research, novel structured fabrics were designed and analyzed to push the future capabilities of adaptive, shape-changing structured media.

The findings of this research have broader implications for the design of adaptive and programmable materials, offering potential innovations in soft robotics, aerospace structures, deployable antennas, and kinetic architecture. By developing a deeper understanding of structured fabric mechanics and deployment strategies, this work lays the foundation for future advancements in energy-efficient, reconfigurable, and high-performance materials.

Future Work

Future work should explore the redesign of the structured fabrics but with alternative actuation mechanisms, such as shape memory alloys, novel weaving patterns, and different types of elastic sheets, combined with localized mechanical locking, to further enhance the functionality and scalability of these materials across various engineering applications. A more comprehensive investigation into the combined effects of key factors influencing performance is necessary, including the exploration of alternative particle geometries beyond topological interlocking.

Like other morphing structure approaches that leverage conformal mapping, our methods are less effective for surfaces with regions of high curvature, where surface accuracy declines due to area distortion. Tile optimization can be investigated to minimize shape deviation for higher curvature target surfaces. To improve deployment accuracy and stability, additional strategies such as integrating connectors or 3D-printed micro-velcro at the tile edges could help lock components together upon contact.

Advancing structured fabric design will require further analysis of how fold patterns influence elastic sheet strain energy and the development of optimization strategies for fold patterns. Integrating these insights into the existing tile pattern generation framework could help refine fold lines and tile arrangements, improving both structural efficiency and deployment reliability.

Chapter 6

APPENDIX

6.1 Appendix 1

Numerical model setup

Truncated tetrahedron particles are characterized by a level set grid of 2 mm/voxel. The surface nodes are discretized with a surface density of 230 points/cm^2. The contact mechanism of a pair of penetrating neighboring particles are estimated by visco-elastic models composed of linear springs and viscous dampers. The linear springs have normal and shear stiffnesses k_n and k_s. The choice of these parameters takes into account factors considering material modulus and TIM arrangements, ensuring no excessive overlap between contacting particles [1]. We assume the stiffnesses of the particles made of two materials are comparable. The viscous dampers have normal damping coefficient γ_n estimated based on coefficient of restitution C_res [2] by

$$\gamma_n = 2\sqrt{m k_\mathrm{n}} \frac{-\ln C_\mathrm{res}}{\sqrt{\pi^2 + \ln {C_\mathrm{res}}^2}} \tag{6.1}$$

where m is the mass of the particles. LS-DEM uses an explicit time integration scheme. The critical time-step is estimated by [3]

$$\Delta t = 0.4\sqrt{\frac{2m}{5k_\mathrm{s}}}. \tag{6.2}$$

The wire stiffness $\bar{k}$ is calibrated to match the experimental result of a single woven wire in an uniaxial tension test. The set of parameters used in this work is documented in Table 6.1.

Table 6.1: Model parameters

Parameter	Value	Units
Normal particle stiffness k_n	2	MN/m
Shear particle stiffness k_s	2	MN/m
Wire stiffness $\bar{k}$	720	N/m
Friction coefficient μ	{0.2,0.3,. . . ,0.9}	-
Time-step Δt	5.6e-7	s
Coefficient of restitution C_res	0.5	-

We construct a 1:1 numerical model for the testing apparatus (Fig. 6.1) with the same level set grid density and surface discretization density. The indenter and the two supports have the same dimension as the actual experimental test machine. The two supports are placed 6 cm apart, same as the experiment. After the numerical TIM sample has been post-tensioned, we allow the sample to settle onto the supports by gravity. We then move the indenter downward at a constant speed. Since we have a small time-step of $\Delta t = 5.6 \times 10^{-7}$ s for numerical stability, we apply a global damping parameter of $1 \times 10^{-4}/\Delta t$ s^{-1} to ensure quasi-static conditions and to avoid excessive computation time [4].

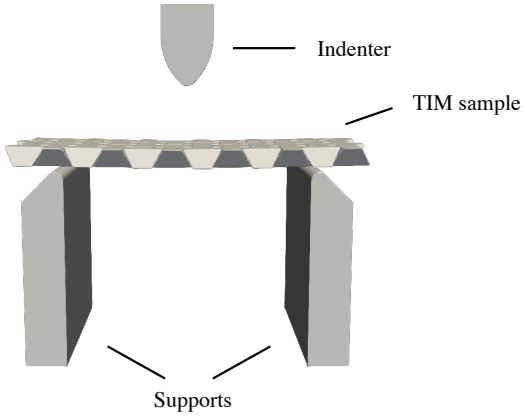

Figure 6.1: Numerical test apparatus.

Fabrication Details and 3D Printing

The Selective laser sinter printing was done with a Sintratec Kit 3D Printer. Selective laser sintering (SLS) [5] is an additive manufacturing technique that uses a laser as the power and heat source to sinter powdered material (in our case Nylon 12), aiming the laser automatically at points in space defined by a 3D model, binding the material together to create a solid structure. This was useful for the particles designed, since they had through holes passing through the each of the edge faces. Since the powder acts as a natural support for the printed geometry, additional support structures were not required.

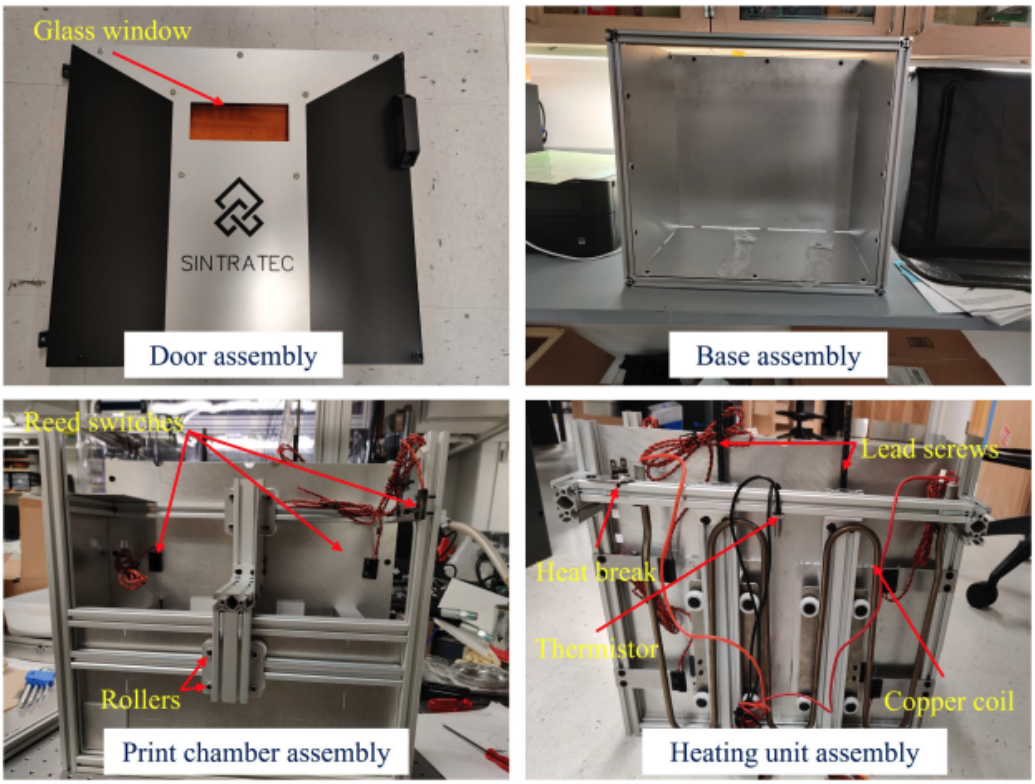

Figure 6.2: Assembly sequence and components of the frame (top) and the print chamber (bottom) [6].

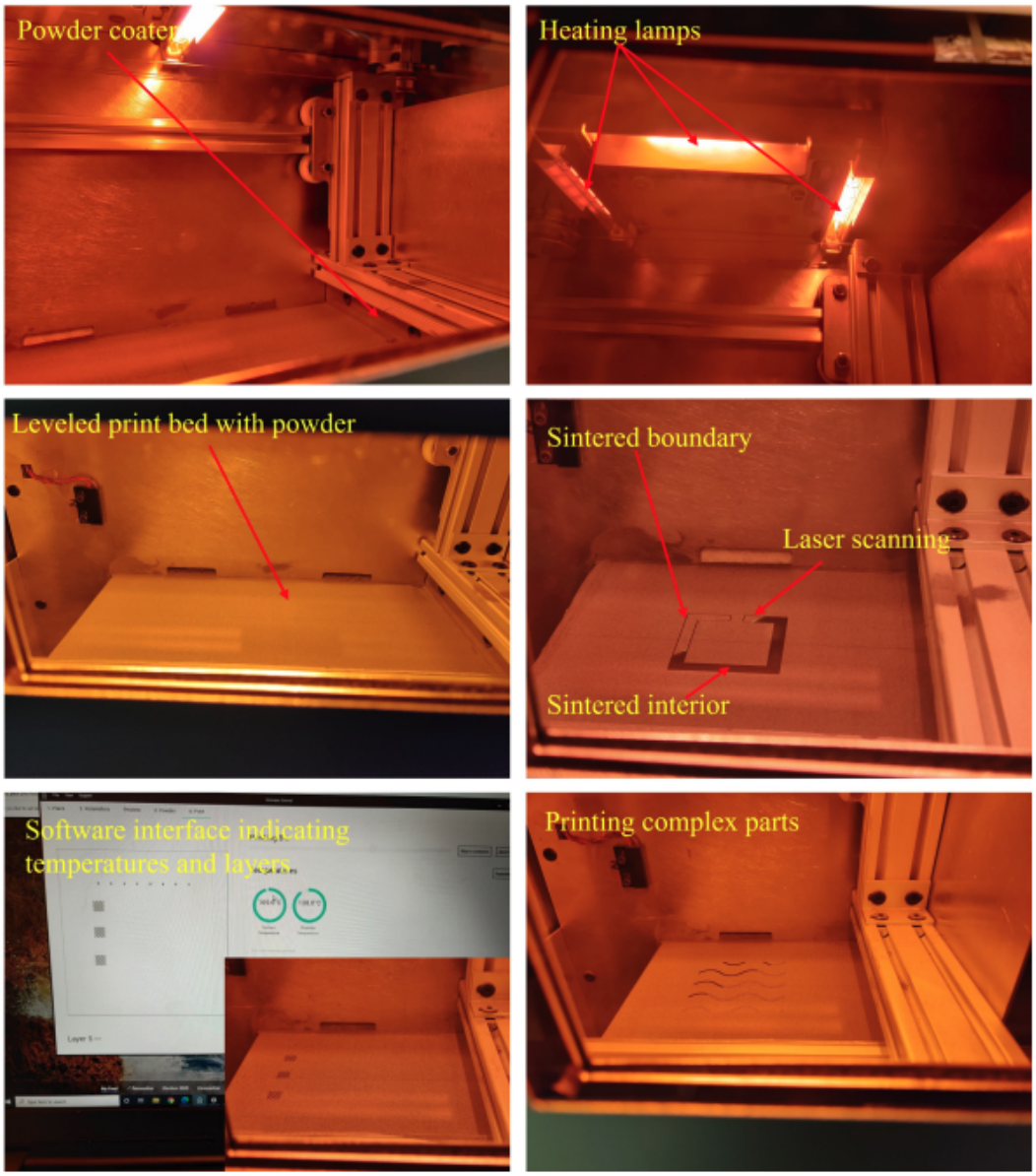

Figure 6.3: Print chamber and print bed during the printing. The temperatures inside the chamber go as high as 150°C, while the sintering area that is exposed to the laser gets as hot as 210°C [6].

Multi-material jetting photopolymer 3D printing technology that quickly creates precise parts using photopolymers, UV light, and inkjet heads [7]. It achieves accuracy by layering resins to form digital materials. Drops of photopolymer are jetted onto the build platform, then cured with UV lamps to bond layers. Support materials are dissolved or manually removed for the finished PolyJet model. This was useful for the particles designed, since they had through holes passing through the each of the edge faces. The support material inside the hole pathways needed to be drilled out and dissolved, and the support material on the outside needed to be scrapped off and dissolved.

Figure 6.4: The Stratasys Object500 Connex 3 Polyjet printer used to print the Vero White photopolymer samples.

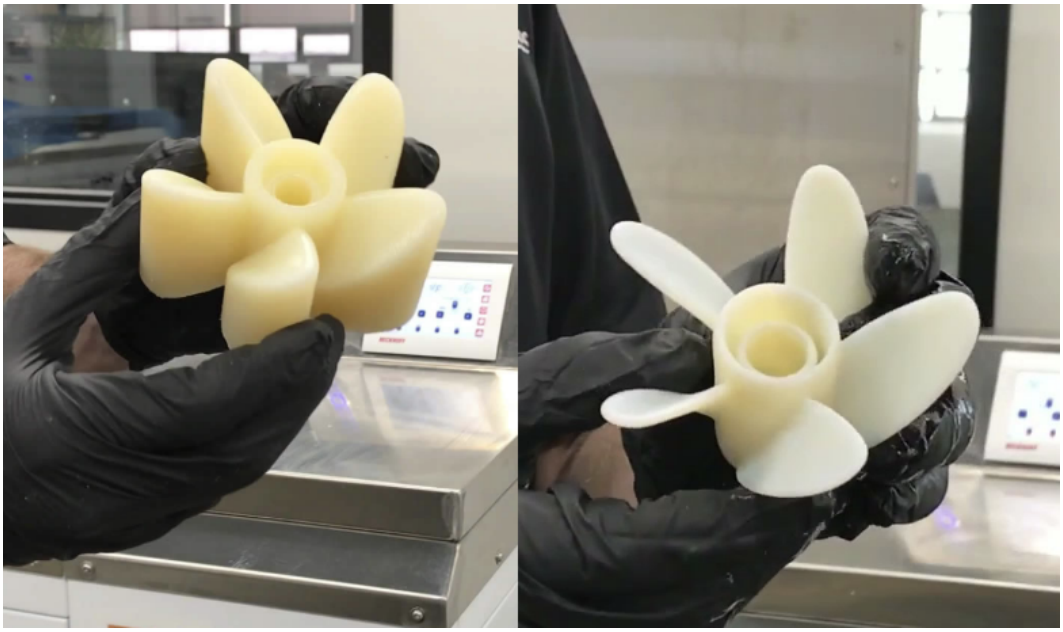

Figure 6.5: An example of how a print comes out of the printer before removing and dissolving support material [8].

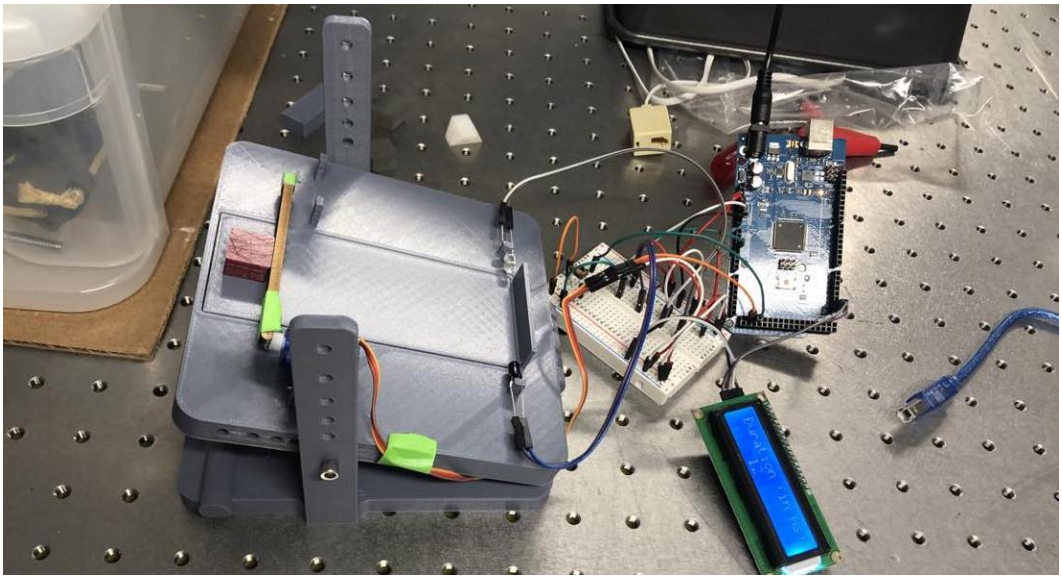

Figure 6.6: A friction sliding test fabricated to confirm the friction coefficients of the particles.

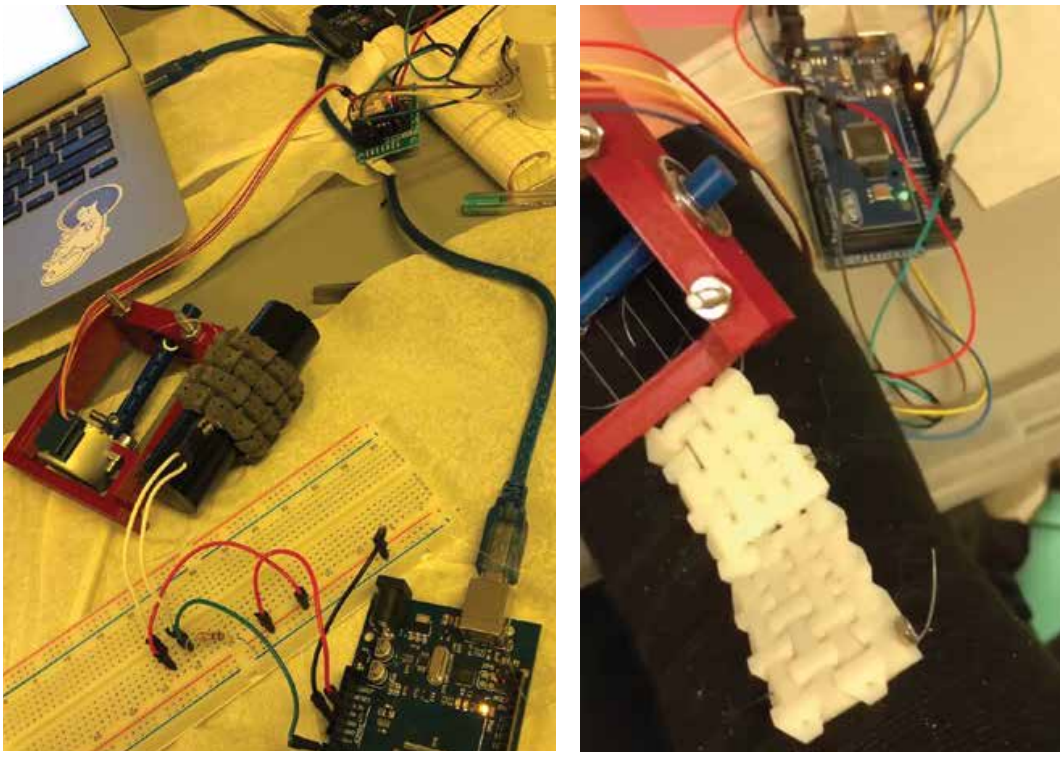

Figure 6.7: Prototypes and tests of how the structured fabrics could be integrated as potential wearables. Left: A rubber cylinder with a similar durometer to that have human skin simulates a finger or wrist with a pressure sensor mounted underneath it. Right: The structured fabric is woven into an elbow sleeve to influence joint movement and function.

6.2 Appendix 2

Initial Concept of a Structured Fabric Deployable

Before deciding on using a prestretched membrane to actuate the structured fabric, shown in Fig. 6.8 the initial prototype also used weaving of discrete particles, similar to the method of Chapter 2 [9]. However, the wires would tangle and the weaving was limited and very difficult to fabricate. This led us to changing the actuation mechanisms to the prestretched membrane which provides uniform, multidirectional tension, as shown in Fig. 6.10. Points were measured and marked on the membrane, then stretched along the hoop corners based on the marked points to obtain a corresponding prestretch factor.

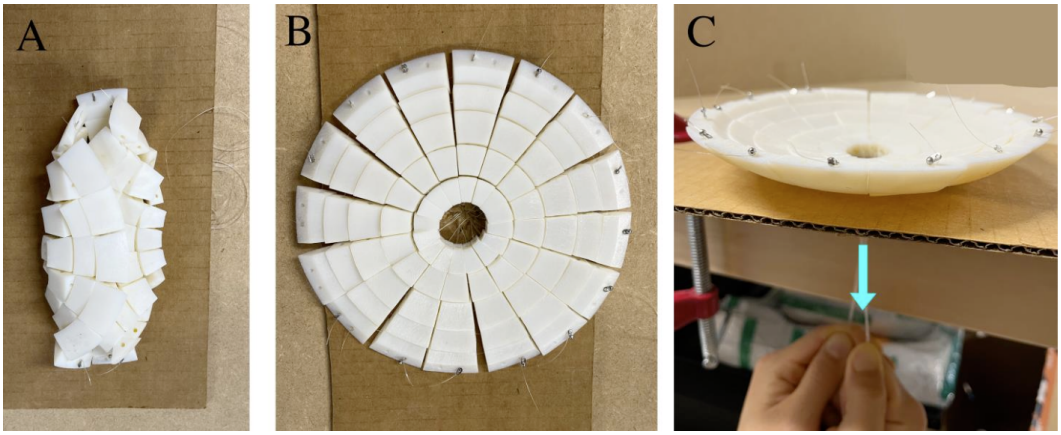

Figure 6.8: Prototype of polymeric antenna structure and sequence of deployments: A) low tension in wires (flexible state) that can be folded compactly for launch; B) slightly more tension in the wires to prepare for full deployment; C) higher tension in the wires for the deployed antenna, with adjustable shape depending on how the tension is allocated among the different wires.

Membrane Stretching

A custom laser cut hoop was designed so that the membrane could be accurately stretched to a predetermined prestretch factor based on measured markings without tearing at the corners.

Figure 6.9: The stretching hoop was made from a laser cut wooden board.

Figure 6.10: Points were measured and marked on the membrane, then stretched along the hoop corners based on the marked points to obtain a corresponding prestretch factor.

Origami Flasher

One origami mechanism that has received considerable attention over the years is the pattern called a "flasher," which was introduced and explored in the origami world by Palmer and Shafer [10]; they developed their concept from the twist-fold

forms of Kawasaki [11]. They have been useful in previous deployable designs where flat panels were stowed and deployed efficiently[12]. The equations used to

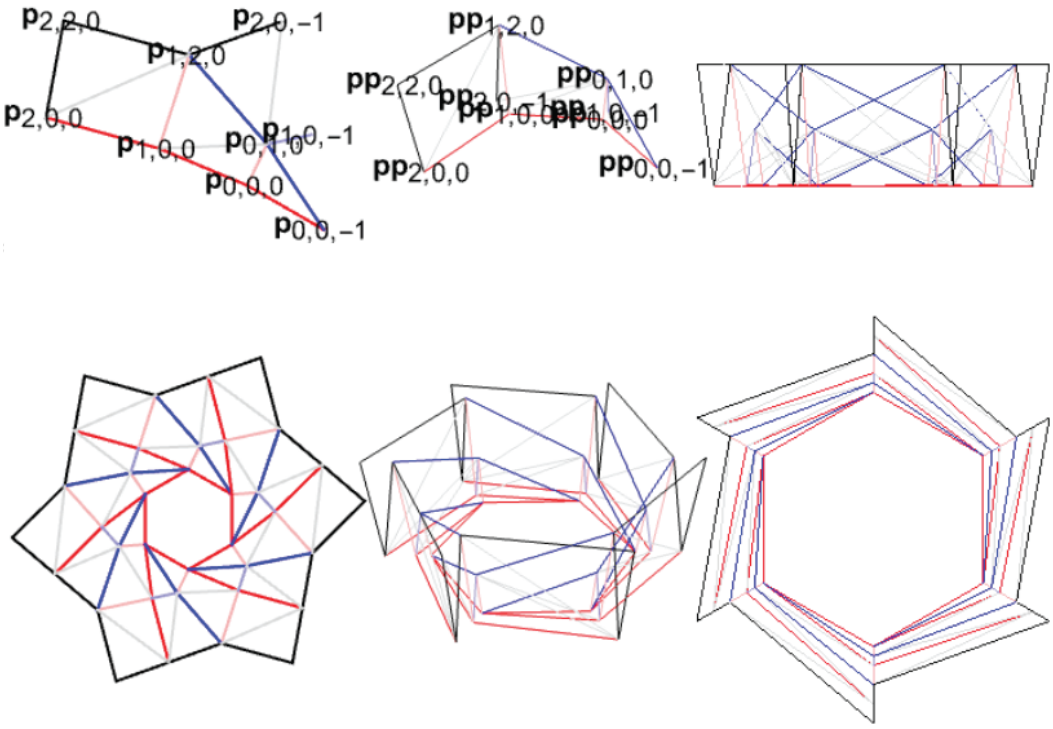

Figure 6.11: Right: Photo of the inside of the 3D Systems SLA ProJet7000 machine. Left: the printed part in the curing procedure in a UV light machine.

calculate the fold line segment points are below:

$$\mathbf{p}_{i,j,k} = \mathbf{R}(k)\cdot\left[\frac{1}{2}\left(\cot\frac{\pi}{m},1\right)+\begin{cases}(i+1)\mathbf{u}\left(\frac{\pi}{2}+\frac{2\pi}{m}\right)+(j)\tan\frac{\pi}{m}\mathbf{u}\left(\frac{2\pi}{m}\right) & \text{if } i+1\geq j\\ (j)\mathbf{u}\left(\frac{\pi}{2}\right)-(i+1)\tan\left(\frac{\pi}{m}\right)\mathbf{u}(0) & \text{otherwise}\end{cases}\right] \tag{6.3}$$

$$\mathbf{p}'_{i,j,k} = \mathbf{R}'(k+\mathrm{rot}(i,j))\cdot\left[\frac{1}{2}\left(\cot\frac{\pi}{m},1,0\right)+\left(0,0,\mathrm{ht}(i,j)\tan\frac{\pi}{m}\right)\right]. \tag{6.4}$$

Fabrication with SLA machine

Stereolithography, also known as vat photopolymerization or resin 3D printing, is an additive manufacturing process where a light source cures liquid resin into hardened plastic [13].

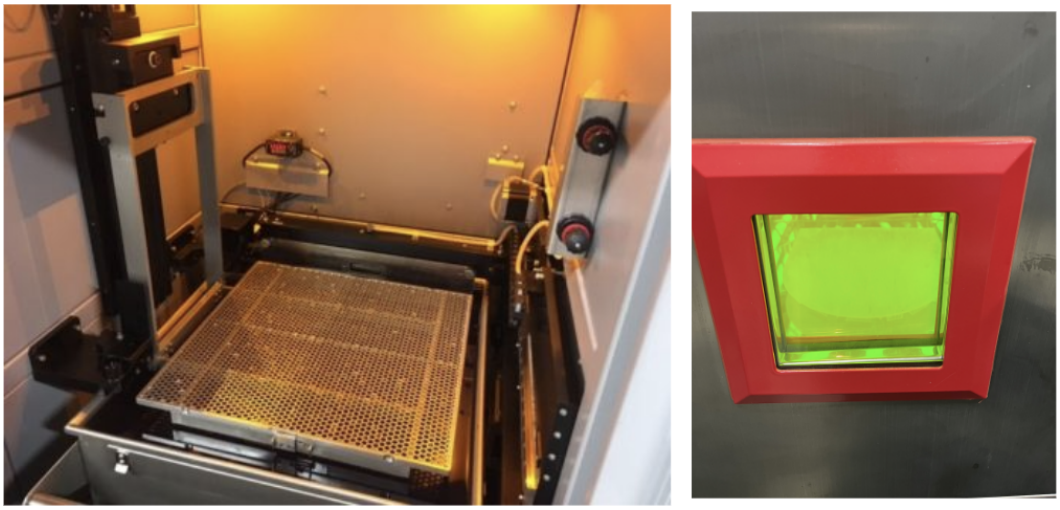

Figure 6.12: Right: Photo of the inside of the 3D Systems SLA ProJet7000 machine. Left: The printed part in the curing procedure in a UV light machine.

This type of 3D printing was necessary for the geometric designs generated, where the tiles need to be held in place relative to each other and attached to a plate, but separate from each other and with the ability to easily detach. The residual powder of SLS printing would interfere with the adhesion to the membrane, and the support material of the polyjet printing would be difficult to remove while keeping the support trees in tact. These issues are shown in Fig. 6.17. Therefore, SLA printing was chosen as the printing method of choice.

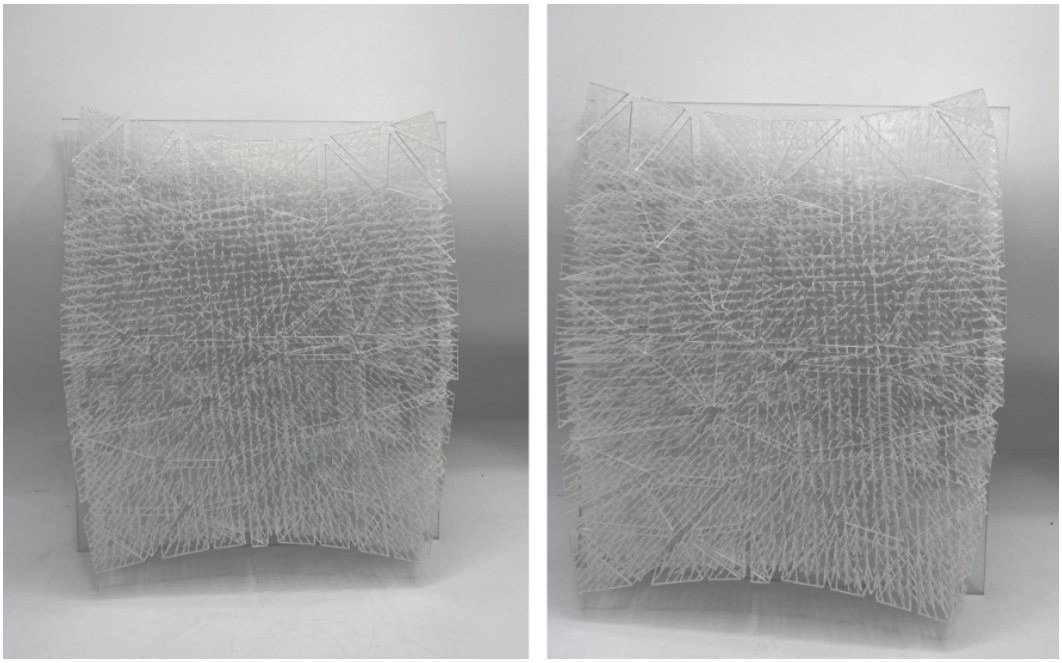

Figure 6.13: The SLA prints attached plate and support trees with Accura ClearVue before the remaining fabrication process of the design in Fig. 3.12.

Figure 6.14: The original designs were attempted in the polyjet printer. However the tiles were difficult to clean and retain in their predetermined configurations.

Further Discretization

The structured fabric designs could be made smoother by increasing the discretization which is determine upon converting the 3D surface to a mesh. While this would make this surface closer to the original input 3D surface, this greatly increases the fabrication complexity. An attempt at this level is shown below in Fig. 6.15.

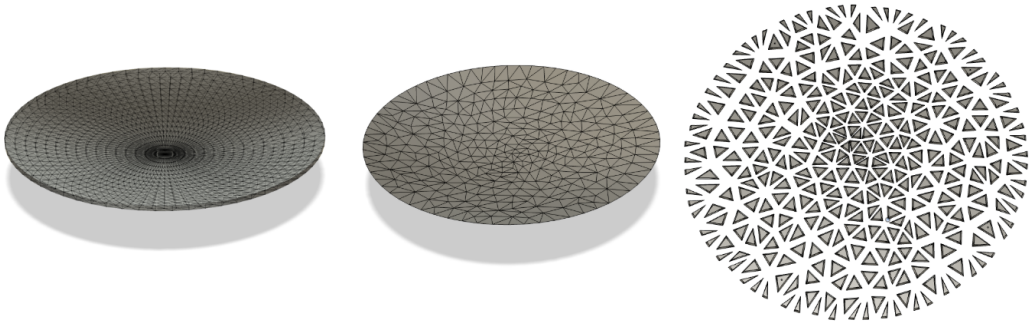

Figure 6.15: Surface conversion to mesh then flattening of mesh for a refined paraboloid.

As shown below in Fig. 6.16, the fabrication of these designs with tiny tiles did not succeed due to the following reasons. The tiles were difficult to align on the top and bottom halves of the membrane. Adhesion by precision cut tape would be too labor intensive, so glue was used. These issues could be mitigated by using an image projector to indicate where the tiles should align when performing the adhesion on that side. Additional hands could help with the massive increase of labor of switching to precision cut tape. However, with the increase of smaller tiles, they become more difficult to handle, especially since their corresponding double-sided tape is even smaller, and due to the increase in quantity, there are more opportunities for tiles to misalign with their top or bottom counterparts.

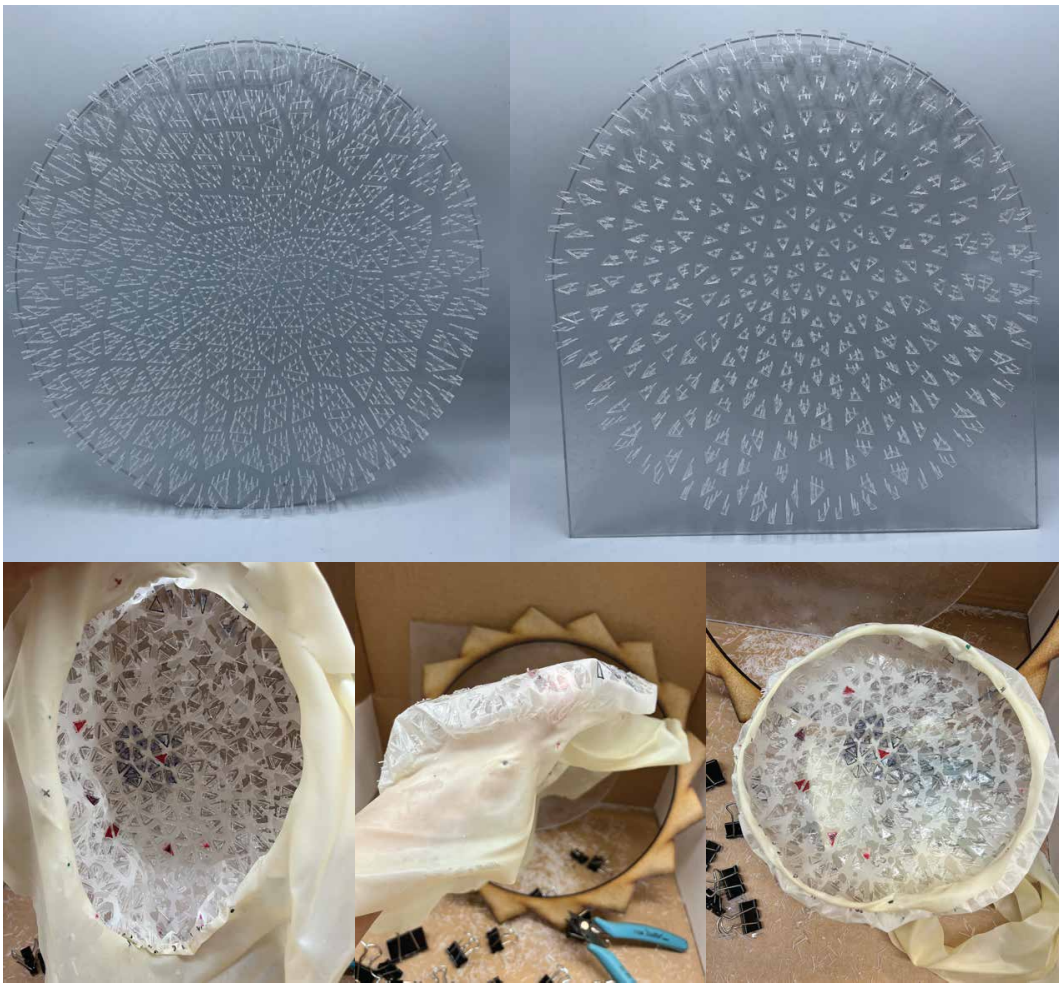

Figure 6.16: Fabrication of the printed parts. Due to the increased number of tiles and decrease in each of their sizes, the fabrication was unable to work without more resources.

6.3 Appendix 3

6.4 Tile Density and Spacing Factor Studies

Below is a table or parameters used in the COMSOL simulation of the tile density and spacing factor studies.

Table 6.2: Simulation Parameters for Tile Density and Spacing Factor Studies

Variable	Name	Expression
E_{tiles}	Young's Modulus of Tiles	1e9[Pa]
v_{tiles}	Poisson's ratio of tiles	0.35
p_{tiles}	density of tiles	1.2e3 [kg/m^3]
λ_m	first Lamé parameter	1.7e6[Pa]
μ_m	second Lamé parameter	1e6[Pa]
p_m	membrane density	950 [kg/m^3]
ele_{size}	mesh element size	0.05

Filleting Radii

The corners of the tiles needed to be rounded or filleted to reduce stress singularities occurring during the simulations. Since the studies are highly sensitive to the membrane's surface area, parameters are adjusted to maintain a constant total membrane area. This ensures that any observed changes are solely attributable to the altered variables and due to changes in membrane area or other inconsistencies.

Rounding the corners of the tiles reduces the amount of rigid tile material but increases the amount of hyperelastic membrane material. In addition, each file has a different tile size and different number of tiles.

At each corner of each right triangle with leg length s, applying a fillet radius r removes a small circular segment.

For the 90° vertex (right angle): The interior angle is $\theta = \frac{\pi}{2}$. Area of the circular segment removed:

$$A_{90^\circ \text{ segment}} = \frac{1}{2}r^2\left(\frac{\pi}{2} - \sin\left(\frac{\pi}{2}\right)\right) = \frac{\pi r^2}{4} - \frac{r^2}{2}.$$

For each 45° vertex: The interior angle is $\theta = \frac{\pi}{4}$. Area of the circular segment removed:

$$A_{45^\circ \text{ segment}} = \frac{1}{2}r^2\left(\frac{\pi}{4} - \sin\left(\frac{\pi}{4}\right)\right).$$

Simplified, this is:

$$A_{45^\circ \text{ segment}} = \frac{\pi r^2}{8} - \frac{\sqrt{2}r^2}{4}.$$

The total area removed due to the fillet is:

$$A_{\text{removed}} = A_{90^\circ \text{ segment}} + 2 \cdot A_{45^\circ \text{ segment}}$$

$$\text{Percent Change} = \frac{A_{\text{removed}}}{A_{\text{original}}} \times 100.$$

Substituting $A_{\text{original}} = \frac{1}{2}s^2$ and A_{removed} :

$$\text{Percent Change} = \frac{(\pi - 1 - \sqrt{2})r^2}{s^2} \times 100$$

To keep the percent change and therefore membrane area consistent, a constant fillet factor, r_o was multiplied by other parameters:

$$r = r_o * \sqrt{\frac{\text{current tile size}}{\text{constant tile size}}} \tag{6.5}$$

so that the fillet radius calculated, r adjusts the tile fillet in a way that maintains a proportional relationship to the edge length across all tile sizes.

To find an appropriate element size, the element size was incrementally varied until the results of the simulation study converged. An example is shown below, where element factor varies inversely with the mesh size.

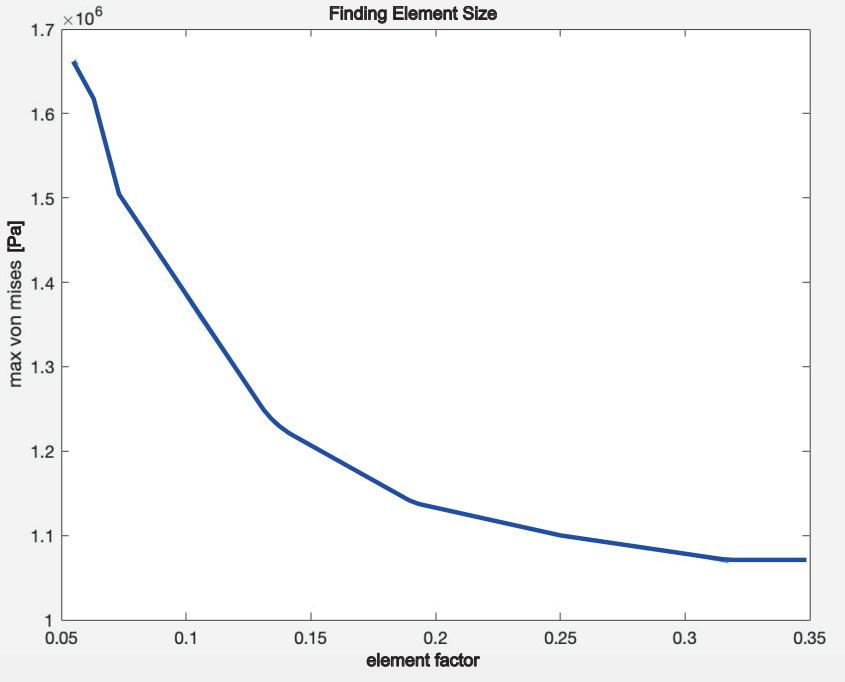

Figure 6.17: As the element factor increases, the mesh size decreases and the maximum recorded von Mises stress converges.

6.5 Folding

The parameters for the folding simulations and analysis are listed in the table below.

Table 6.3: Simulation Parameters for Folding Studies

Variable	Name	Expression
T	tile thickness	range(.001,.009/90,.01)[m]
w	width	.011[m]
d	depth	.2[m]
ramp	ramp increment	range(0,1/(N_{ramp} − 1),1)
λ_m	first Lamé parameter	1.7E6[Pa]
μ_m	second Lamé parameter	1E6[Pa]
p_m	membrane density	1E3 [kg/m^3]
t	membrane thickness	2.032E − 4[m]
N_{ramp}	end of ramp	30
L_x	sticker gap	4E − 4[m]
ele_{size}	mesh element size	t/5*.8

6.6 Bibliography

References

[1] S. Feldfogel, K. Karapiperis, J. Andrade, and D. S. Kammer, "Failure of topologically interlocked structures — a level-set-dem approach," *European Journal of Mechanics - A/Solids*, vol. 103, p. 105 156, 2024, ISSN: 0997-7538. DOI: https://doi.org/10.1016/j.euromechsol.2023.105156.

[2] Y. Tsuji, T. Kawaguchi, and T. Tanaka, "Discrete particle simulation of two-dimensional fluidized bed," *Powder Technology*, vol. 77, no. 1, pp. 79–87, 1993, ISSN: 0032-5910. DOI: https://doi.org/10.1016/0032-5910(93)85010-7.

[3] X. Tu and J. E. Andrade, "Criteria for static equilibrium in particulate mechanics computations," *International Journal for Numerical Methods in Engineering*, vol. 75, no. 13, pp. 1581–1606, 2008. DOI: https://doi.org/10.1002/nme.2322.

[4] R. Kawamoto, E. Andò, G. Viggiani, and J. E. Andrade, "Level set discrete element method for three-dimensional computations with triaxial case study," *Journal of the Mechanics and Physics of Solids*, vol. 91, pp. 1–13, 2016, ISSN: 0022-5096. DOI: https://doi.org/10.1016/j.jmps.2016.02.021.

[5] M. B. Kumar, P. Sathiya, and M. Varatharajulu, "Selective laser sintering," in *Advances in Additive Manufacturing Processes*, Bentham Science Publishers, Nov. 29, 2021, pp. 28–47. [Online]. Available: https://www.benthamdirect.com/content/books/9789815036336.chapter-2.

[6] P. C. J. K. Boddapati, "Shear-normal coupled deformations in anisotropic structured materials," Ph.D. dissertation, California Institute of Technology, 2025. DOI: 10.7907/k1t8-4t34. [Online]. Available: https://resolver.caltech.edu/CaltechTHESIS:08142024-070224435.

[7] P. Patpatiya, K. Chaudhary, A. Shastri, and S. Sharma, "A review on polyjet 3d printing of polymers and multi-material structures," *Proceedings of the Institution of Mechanical Engineers, Part C: Journal of Mechanical Engineering Science*, vol. 236, no. 14, pp. 7899–7926, Jul. 1, 2022, Publisher: IMECHE, ISSN: 0954-4062. DOI: 10.1177/09544062221079506. [Online]. Available: https://doi.org/10.1177/09544062221079506.

[8] "Removing stratasys PolyJet support material." Section: 3D Printing Techniques. (Mar. 17, 2021), [Online]. Available: https://www.javelin-tech.com/blog/2021/03/removing-stratasys-polyjet-support-material/.

[9] T. Lu, Z. Zhou, P. Bordeenithikasem, *et al.*, "Role of friction and geometry in tuning the bending stiffness of topologically interlocking materials," *Extreme Mechanics Letters*, vol. 71, p. 102 212, Sep. 1, 2024, ISSN: 2352-4316. DOI: 10.1016/j.eml.2024.102212. [Online]. Available: https://www.sciencedirect.com/science/article/pii/S2352431624000920.

[10] R. Lang. "Origami in action," Macmillan Publishers. (1997), [Online]. Available: https://us.macmillan.com/books/9780312156183/origamiinaction/.

[11] Kawasaki. "Roses, origami & math," Origami USA: We are the American national society devoted to origami, the art of paperfolding. (Nov. 9, 2011), [Online]. Available: https://origamiusa.org/library-book/roses-origami-math.

[12] R. J. Lang, S. Magleby, and L. Howell, "Single degree-of-freedom rigidly foldable cut origami flashers," *Journal of Mechanisms and Robotics*, vol. 8, no. 3, p. 031 005, Jun. 1, 2016, ISSN: 1942-4302, 1942-4310. DOI: 10.1115/1.4032102. [Online]. Available: https://asmedigitalcollection.asme.org/mechanismsrobotics/article/doi/10.1115/1.4032102/441838/Single-DegreeofFreedom-Rigidly-Foldable-Cut.

[13] C. Schmidleithner and D. M. Kalaskar, "Stereolithography," in *In: Cvetković, D, (ed.) 3D Printing. (pp. 1-22). IntechOpen: London, UK. (2018)*, D. Cvetković, Ed., London, UK: IntechOpen, 2018, pp. 1–22. [Online]. Available: https://doi.org/10.5772/intechopen.78147.